

PHASE TRANSITIONS IN  
CARBON-BASED NANOCCLUSERS  
as seen via molecular dynamics simulations

Dissertation zur Erlangung des Doktorgrades  
der Naturwissenschaften

vorgelegt beim Fachbereich Physik  
der Goethe Universität  
in Frankfurt am Main

von

ADILAH HUSSIEN  
aus Singapur

Frankfurt am Main 2010  
(FB 13)

ii

vom Fachbereich Physik  
der Goethe Universität als Dissertation angenommen.

Dekan: Prof. Dr. Dirk H. Rischke

Gutachter 1: Prof. Dr. Andrey V. Solovyov

Gutachter 2: Prof. Dr. Dr. h.c. mult. Walter Greiner

# ABSTRACT

Nanocarbon structures, such as fullerenes and nanotubes, have generated considerable interest and research, due to their unique properties and potential applications. In this thesis, we present a study of the phase transition properties of nanocarbon clusters—in particular, we pay special consideration to fullerenes. The work presented in this thesis is largely theoretical and computational in nature, employing as a tool, molecular dynamics simulations to probe the dynamic stability of fullerenes and associated nanocarbon structures such as graphenes and nanotubes.

We have investigated the phase transition of buckminsterfullerene  $C_{60}$ , corresponding to a topologically-free (TF) and a topologically-constrained (TC) model. The TF case was constructed using the Tersoff potential, while the TC model is based on a novel forcefield that we have developed: the Topologically-constrained forcefield. We have explored the phase transition properties of both models within different simulation volumes and for different lengths of simulation times. The TF- $C_{60}$  was observed to experience a first-order phase transition in a simulation volume of  $1.25 \times 10^8 \text{Å}^3$ ; while a second-order phase transition was observed when the simulation volume was reduced to  $8 \times 10^3 \text{Å}^3$ . In both cases, the TF- $C_{60}$  exhibited transformations to a series of carbon phases prior to multifragmentation at high temperatures.

The TC- $C_{60}$ , in contrast, did not show transient phase transformations prior to multifragmentation. However, in the smaller simulation volume, the TC- $C_{60}$  undergoes a *dynamic phase coexistence*, where the fullerene is seen to continuously fragment and reassemble back into the fullerene cage. Hence the TC- $C_{60}$  and carbon gas state effectively coexists at the phase transition temperature. Based on these results, we have constructed a statistical me-

chanics model to correspond the conditions of the dynamic phase coexistence of  $C_{60}$  to the generalised pressure and temperature conditions in typical arc-discharge experiments. Nevertheless, the correspondence is quite idealised due to the complex nature of the experimental conditions.

Furthermore, we have studied the phase transitions in fullerenes  $C_{32}$  to  $C_{540}$ , where we have shown that the fragmentation pathways within the simulations are different for fullerenes smaller and bigger than  $C_{70}$ . Small fullerenes were shown to transform into transient graphene phases before multifragmentation to the carbon gas phase. Whereas no such phase were observed for the larger fullerenes. Such a behaviour may be attributed to entropic factors which would make transformation to the graphene phase unlikely.

Additionally, we have also investigated the phase transitions of a cluster of 240 carbon atoms in the form of a fullerene, buckyball,  $C_{60}@C_{180}$  carbon onion, graphene and an uncapped (10,10) nanotube. In this study, we have found that the carbon onion, nanotube and buckyball structures transform into a fullerene before a phase transition to carbon gas. Graphene, on the other hand, showed no transformation to other phases prior to fragmentation, allowing one to surmise that it follows a different fragmentation pathway.

Finally, we have studied the interaction of carbon with a metal nanocluster,  $Ni_{147}$ . Specifically, we investigate how the melting temperature of the nickel cluster is affected by the presence of a carbon atom or a  $C_2$  molecule. We also investigate the diffusion of the carbon impurity within the nickel nanocluster. This question is relevant because, during the nanotube growth process, it is thought that the carbon atoms may migrate into the metal nanocluster, causing “poisoning” of the catalytic particle and halting the growth process of the nanotubes. Thus, knowledge of the specific role of a carbon impurity in the Ni catalytic nanoparticle may ascertain whether the carbon nanotube structure and its growth kinetics can be controlled. Moreover, understanding how the metal nanocluster reacts with the carbon impurity will help shed light on controlling the production yields of higher fullerenes.

# KURZFASSUNG

Das Thema dieser Dissertation ist die Erforschung der Phasenübergänge der Kohlenstoff-Nanostrukturen, wobei den Fullerenen besondere Beachtung geschenkt wird. Der Grossteil der Ergebnisse basiert auf Theorie und Computersimulationen, wobei Molekulardynamische Simulationen genutzt werden um dynamische Stabilität der Fullerene und verwandter Systeme wie Fullerene, Nanoröhrchen und “Nanoschsselchen” zu untersuchen.

In dieser Dissertation werden die offenen Problemstellungen der Entstehung und des Zerfalls der Fullerene als Phasenübergang in Angriff genommen, wobei insbesondere der Phasenübergang des Buckminsterfullerens  $C_{60}$  in topologisch-selektiven und topologisch-freien Modellen untersucht werden. Das topologisch freie Modell wurde mithilfe des Tersoff Potentials entwickelt, wogegen für das topologisch selektive Modell ein neuartiges Kraftfeld entwickelt wurde: Das topologisch selektive Kraftfeld [1]. In beiden Fällen wurden die Eigenschaften der Phasenübergänge bei unterschiedlichen Simulationsvolumen und unterschiedlicher Simulationsdauer untersucht.

Aufbauend auf diesen Ergebnissen wurde ein statistisches Modell entwickelt, das die Bedingungen der dynamischen Phasenkoexistenz mit den Umgebungsbedingungen – Druck und Temperatur – bei Bogenentladungen in Zusammenhang bringt und es einem ermöglicht den Temperatur- und Druckbereich in dem der Phasenübergang beobachtet werden kann abzuschätzen. Allerdings sollte beachtet werden daß bei diesem statistischen Modell von einem lokalem Gleichgewicht ausgegangen wird und diverse Details der Bedingungen im Experiment, wie Temperaturgradienten und geladene Teilchen vernachlässigt wurden.

Ausser den Buckminsterfullerenen wurden auch Phasenübergänge in an-

deren Fullerenen, von  $C_{32}$  bis  $C_{540}$  untersucht. Die Molekulardynamischen Simulationen deuten darauf hin daß die grösseren Moleküle stabiler als  $C_{60}$  sind, was damit im Einklang steht daß die höheren Fullerene grössere Bindungsenergien als  $C_{60}$  haben. Daher scheint es als reichen die thermodynamischen und energetischen Kriterien nicht aus, die besondere Stabilität von  $C_{60}$  zu beschreiben, wie sie in diversen Experimenten beobachtet wurde – insbesondere der hohe Anteil von  $C_{60}$  in den Methoden zur Erzeugung von Fullerenen. Zudem wurde in den Simulationen beobachtet daß sich Zerfallswege der Fullerene die grösser als  $C_{70}$  sind sich von den Zerfallswegen der kleineren Fullerene unterhalb von  $C_{70}$  unterscheiden. Kleinere Fullerene wandeln sich vor der multiplen Fragmentierung zum Kohlenstoff Gas in Graphenstrukturen um wogegen es bei grösseren Fullerenen keine Anzeichen für derartige Übergangsphasen gibt. Ein dertatiges Verhalten lässt sich durch die Entropie der entarteten Konfigurationen erklären, die die Wahrscheinlichkeit eines Übergangs in die Graphenstruktur verringert.

Zusätzlich wurden auch die Phasenübergänge in Clustern von 240 Kohlenstoff Atomen untersucht, die die Struktur eines Fulleren, eines Nanoschüsselchens, einer  $C_{60}@C_{180}$  Nanozwiebel oder eines offenen (10,10) Nanoröhrchens annehmen können [2]. Wie in Abbildung 2 beispielhaft zu sehen ist hat diese Untersuchung ergeben daß die Nanozwiebel, das Nanoschüsselchen und das Nanoröhrchen zuerst in ein Fulleren über gehen. Bei Graphen konnten allerdings keine Übergangsphasen vor der Fragmentierung beobachtet werden, weshalb sich vermuten lässt das es sich hierbei um einen anderen Zerfallsweg handelt.

# ZUSAMMENFASSUNG

Als Cluster bezeichnet man begrenzte Ansammlungen von Atomen oder Molekülen die durch die Wechselwirkungen zwischen Atomen gebunden sind. So gibt es diverse verschiedene Cluster, wie metalische und van der Waals Cluster, Graphene oder Fullerene. Unterschiedliche Cluster sind sehr verschieden geometrisch aufgebaut und können aus nur wenigen Atomen oder auch zehntausenden Atomen bestehen [3].

Daher können Cluster als eine Brücke zwischen Atomen und der gewöhnlichen kondensierten Materie betrachtet werden. Dementsprechend haben sie einzigartige Eigenschaften und es besteht großes Forschungsinteresse darin zu untersuchen wie ihre Eigenschaften im Zusammenhang mit ihrer Größe stehen, insbesondere mit Blick auf mögliche Phasenübergänge [4–11].

Diese Herausforderung den Übergang zwischen Quantenobjekten und klassischen Objekten zu verstehen ist nach wie vor eine der grundlegendsten Motivationen in der Clusterphysik.

Ausserdem gibt es signifikante Überschneidungen zwischen der Clusterphysik und der Nanotechnologie, insbesondere der Herstellung und Bearbeitung von Nanostrukturen und Nanomaschinen. Daher ist aufgrund ihrer potenziellen Anwendungen grosses Interesse in Kohlenstoff-Nanostrukturen, z.B. Fullerene und Nanoröhrchen, entstanden.

Das Thema dieser Dissertation ist die Erforschung der Phasenübergänge der Kohlenstoff-Nanostrukturen, wobei den Fullerenen besondere Beachtung geschenkt wird. Der Grossteil der Ergebnisse basiert auf Theorie und Computersimulationen, wobei Molekulardynamische Simulationen genutzt werden um dynamische Stabilität der Fullerene und verwandter Systeme wie Fullerene, Nanoröhrchen und “Nanoschüsselchen” zu untersuchen.

Wegen seiner einzigartigen Struktur und Eigenschaften ist das Buckminsterfulleren seit seiner Entdeckung in 1985 [12] eines der faszinierendsten Forschungsobjekte. Trotz 25 Jahren intensiver Forschung wirft das  $C_{60}$  Molekül noch viele offene Fragen auf. So ist noch nicht viel über die Entstehung, die Stabilität, Energieabsorbierung und darauffolgende Energieverteilung im Molekül bekannt. Ein besonders langanhaltender Streitpunkt beinhaltet das Mysterium der Entstehung von Fullerenen.

In dieser Dissertation werden die offenen Problemstellungen der Entstehung und des Zerfalls der Fullerene als Phasenübergang in Angriff genommen, wobei insbesondere der Phasenübergang des Buckminsterfullerens  $C_{60}$  in topologisch-selektiven und topologisch-freien Modellen untersucht werden. Das topologisch freie Modell wurde mithilfe des Tersoff Potentials entwickelt, wogegen für das topologisch selektive Modell ein neuartiges Kraftfeld entwickelt wurde: Das topologisch selektive Kraftfeld [1]. In beiden Fällen wurden die Eigenschaften der Phasenübergänge bei unterschiedlichen Simulationsvolumen und unterschiedlicher Simulationsdauer untersucht.

Im Fall des topologisch freien  $C_{60}$  wurde bei einem Simulationsvolumen von  $1.25 \times 10^8 \text{Å}^3$  ein Phasenübergang erster Ordnung beobachtet, wogegen nach einer Reduktion des Volumens auf  $8 \times 10^3 \text{Å}^3$  ein Phasenübergang zweiter Ordnung beobachtet wurde. In diesen beiden Fällen gab es im topologisch freien Modell Übergänge zwischen unterschiedlichen Strukturen des Moleküls geringfügig unterhalb der Temperatur der multiplen Fragmentierung. Bei dem Übergang erster Ordnung ähnelten diese Strukturen Röhren, Schüsselchen und Graphen. Ausserdem wurde beobachtet wie das  $C_{60}$  Molekül  $C_2$  Moleküle und Kohlenstoff Atome abdampft. Hingegen waren dem Phasenübergang zweiter Ordnung die Graphen Strukturen in einem Temperaturbereich von ca. 3600K bis 4300K metastabil.

Im Gegensatz zu den topologisch freien Modellen gab es bei den topologisch selektiven Modellen keine Anzeichen von derartigen Übergängen vor der Fragmentierung. Allerdings wurde Beobachtet daß im Fall des kleineren Simulationsvolumens die Phasen dynamisch koexistieren und das Fulleren wiederholt zerfällt und sich wieder komplett zusammensetzt, was in Abbildung 1 dargestellt wird. Dementsprechend koexistiert im Bereich der kritis-



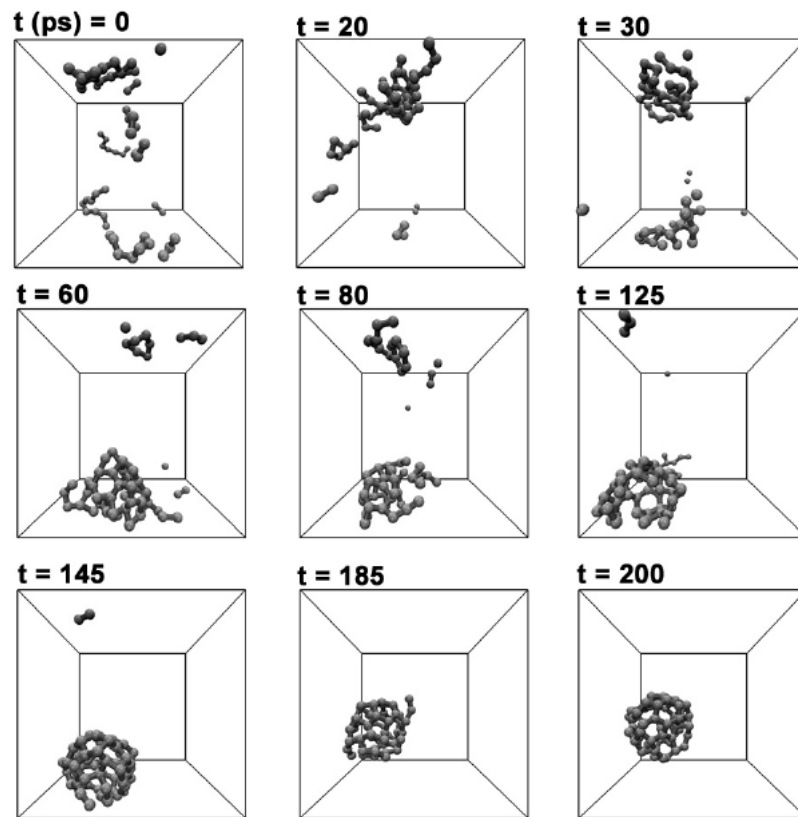


Figure 1: Rekonstituierung der  $C_{60}$  Struktur bei der kritischen Temperatur im topologisch selektiven Modell.

chen Temperatur das topologisch selektive  $C_{60}$  mit dem Kohlenstoff Gas.

Aufbauend auf diesen Ergebnissen wurde ein statistisches Modell entwickelt, das die Bedingungen der dynamischen Phasenkoexistenz mit den Umgebungsbedingungen – Druck und Temperatur – bei Bogenentladungen in Zusammenhang bringt und es einem ermöglicht den Temperatur- und Druckbereich in dem der Phasenübergang beobachtet werden kann abzuschätzen. Allerdings sollte beachtet werden daß bei diesem statistischen Modell von einem lokalem Gleichgewicht ausgegangen wird und diverse Details der Bedingungen im Experiment, wie Temperaturgradienten und geladene Teilchen vernachlässigt wurden.

Ausser den Buckminsterfullerenen wurden auch Phasenübergänge in an-

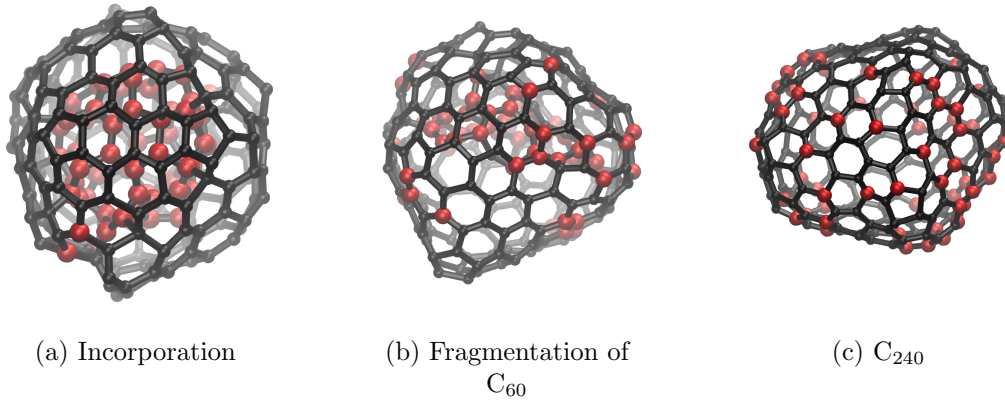


Figure 2: Der Übergang von  $C_{60}@C_{180}$  zu  $C_{240}$  beginnt mit der Aufnahme von Kohlenstoff Atomen des  $C_{60}$  in die  $C_{180}$  Struktur (a), gefolgt von der Fragmentierung der  $C_{60}$  Struktur wenn dessen Atome sukzessive in die  $C_{180}$  Struktur Einwachsen (b) bevor der Endzustand, die  $C_{240}$  Struktur (c) erreicht wird.

deren Fullerenen, von  $C_{32}$  bis  $C_{540}$  untersucht. Die Molekulardynamischen Simulationen deuten darauf hin daß die grösseren Moleküle stabiler als  $C_{60}$  sind, was damit im Einklang steht daß die höheren Fullerene grössere Bindungsenergien als  $C_{60}$  haben. Daher scheint es als reichen die thermodynamischen und energetischen Kriterien nicht aus, die besondere Stabilität von  $C_{60}$  zu beschreiben, wie sie in diversen Experimenten beobachtet wurde – insbesondere der hohe Anteil von  $C_{60}$  in den Methoden zur Erzeugung von Fullerenen. Zudem wurde in den Simulationen beobachtet daß sich Zerfallswege der Fullerene die grösser als  $C_{70}$  sind sich von den Zerfallswegen der kleineren Fullerene unterhalb von  $C_{70}$  unterscheiden. Kleinere Fullerene wandeln sich vor der multiplen Fragmentierung zum Kohlenstoff Gas in Graphenstrukturen um wogegen es bei grösseren Fullerenen keine Anzeichen für derartige Übergangsphasen gibt. Ein dertatiges Verhalten lässt sich durch die Entropie der entarteten Konfigurationen erklären, die die Wahrscheinlichkeit eines Übergangs in die Graphenstruktur verringert.

Zusätzlich wurden auch die Phasenübergänge in Clustern von 240 Kohlenstoff Atomen untersucht, die die Struktur eines Fullerenens, eines Nanoschüssel-

chens, einer  $C_{60}@C_{180}$  Nanozwiebel oder eines offenen (10,10) Nanoröhrchens annehmen können [2]. Wie in Abbildung 2 beispielhaft zu sehen ist hat diese Untersuchung ergeben daß die Nanozwiebel, das Nanoschüsselchen und das Nanoröhrchen zuerst in ein Fulleren über gehen. Bei Graphen konnten allerdings keine Übergangsphasen vor der Fragmentierung beobachtet werden, weshalb sich vermuten lässt das es sich hierbei um einen anderen Zerfallsweg handelt.

Die Untersuchung der Phasenübergänge von  $C_{60}$  und anderen kleinen Kohlenstoff Nanostrukturen ist ein wichtiger Schritt in der Erforschung der Stabilität und Widerstandsfähigkeit dieser Strukturen, ihrer Entstehungsmechanismen und Übergänge zwischen unterschiedlichen Strukturen. Zudem ist das Wissen ueber die Phasenübergänge der Kohlenstoff Nanostrukturen wichtig um deren Phasendiagramm zu aufzubauen, das den Phasenraum einer stabiler Strukturen in Temperatur, Druck und Anzahl der Atome zeigt. Derartige Informationen sind essenziell in den Anwendungen der Kohlenstoff Nanostrukturen, insbesondere in der Nanoelektronik.



# ACKNOWLEDGMENTS

I thank my supervisor, Prof. Andrey Solov'yov, for his patience, his advice and his encouragement. Working with him and in his group has been an enriching experience.

I thank the members of the MBN group for the advice and support: Alexander Yakubovich, Stephanie Lo, Dr. Emanuele Scifoni, Veronika Dick, Dr. Andrei Korol, Dr. Ilia Solov'yov, Dr. Andriy Kostyuk, Pavel Nikolaev and Dr. Ekaterina Paramonova. I especially thank Alexander Yakubovich, with whom I have collaborated, for his help and patience.

I thank Drs. Andrey Lyalin and Elsa Henriques for teaching me, for their advice and support and for helping me correct my thesis. To Prof. J-P. Connerade, thank you! Thank you for always being there to advise and encourage me. I also wish to thank Prof. Walter Greiner for his helpful advice on my work, and to Prof. Dirk Rischke for his support and his help. To Mauricio Martinez and Cristina Savin, I thank them for their advice regarding the thesis submission.

To my friends Hasnaa Fatehi, Maneesh Mathew and Jenia Jitsev—“Thank you” would be an understatement, but I thank them nonetheless, for their friendship, their support, their advice, for believing in me, for being there for me, for their courage and for encouraging me.

To my parents, I am grateful for their constant love and support, for always being there to hear me out, for reminding me that failure cannot cope with persistence. To my sisters, *meh pas ni kiter buka kedai kopi samerx2 pat jepon lul, pastu milly leh bwat kek, nana leh jadi org pat counter pastu aku leh bwatx2 kopi, kan best!* and to Noetta, for being my Chep.



To my teachers.





# CONTENTS

<b>Contents</b>	<b>xvii</b>
<b>1 Introduction</b>	<b>1</b>
1.1 The world of clusters . . . . .	1
1.2 Understanding fullerenes . . . . .	2
1.2.1 Making fullerenes . . . . .	4
1.2.2 Breaking fullerenes . . . . .	7
1.2.3 Using fullerenes . . . . .	9
1.3 Thesis overview . . . . .	11
<b>2 Methods</b>	<b>13</b>
2.1 Molecular Dynamics . . . . .	14
2.1.1 Atomic interactions . . . . .	15
2.1.2 Time in molecular dynamics . . . . .	17
2.2 Bond-order potentials . . . . .	19
2.2.1 The Tersoff Potential . . . . .	20
2.2.2 Post-Tersoff potentials . . . . .	23
2.3 The Topologically-constrained Forcefield . . . . .	24
2.4 The Sutton-Chen potential . . . . .	27
2.5 Simulation parameters . . . . .	28
2.6 Chapter summary . . . . .	29
<b>3 Principles of phase transition</b>	<b>31</b>
3.1 Classifying phase transitions . . . . .	32
3.2 Phase coexistence . . . . .	34

3.3	Chapter summary . . . . .	37
<b>4</b>	<b>C<sub>60</sub>: Buckminsterfullerene</b>	<b>39</b>
4.1	Finite time simulations . . . . .	40
4.2	Topology and volume effects . . . . .	43
4.2.1	The topologically-free C <sub>60</sub> . . . . .	44
4.2.2	Validation of the Topologically-constrained forcefield . . . . .	49
4.2.3	The topologically-constrained C <sub>60</sub> . . . . .	52
4.3	Statistical mechanics model . . . . .	61
4.4	Chapter summary . . . . .	72
<b>5</b>	<b>Nanocarbon transitions</b>	<b>73</b>
5.1	Stability of fullerenes larger than C <sub>60</sub> . . . . .	74
5.1.1	Phase transitions of C <sub>32</sub> to C <sub>540</sub> . . . . .	76
5.1.2	Fragmentation dynamics . . . . .	81
5.2	Nanocarbon structures . . . . .	86
5.2.1	Phase transitions of C <sub>240</sub> . . . . .	88
5.3	Chapter summary . . . . .	92
<b>6</b>	<b>Interaction of carbon with a metal cluster</b>	<b>95</b>
6.1	Pure and Carbon-doped Clusters . . . . .	96
6.1.1	Pure Ni <sub>147</sub> clusters . . . . .	98
6.1.2	Carbon-doped Ni <sub>147</sub> clusters . . . . .	101
6.2	Modifying the Ni-C interaction . . . . .	108
6.3	Chapter summary . . . . .	112
<b>7</b>	<b>Conclusions</b>	<b>113</b>
	<b>Bibliography</b>	<b>117</b>
	<b>List of Figures</b>	<b>143</b>
	<b>List of Tables</b>	<b>151</b>
	<b>Curriculum Vitae</b>	<b>153</b>

# CHAPTER 1

## INTRODUCTION

### 1.1 THE WORLD OF CLUSTERS

Cluster science remains one of the most rapidly expanding fields in research [10, 11]. This interdisciplinary field has attracted enormous interest, both fundamentally and in terms of future applications in electronics, medicine and energy. Advances in computational power and in experimental and theoretical techniques have allowed for extensive investigations of the various types and sizes of atomic and molecular clusters.

Clusters are finite aggregates of atoms or molecules that are bound by inter-atomic forces. There are a wide variety of clusters, from metallic and van der Waals clusters to graphenes and fullerenes. Each with different structural and geometrical organisations, and with sizes that can range from a few to tens of thousands of atoms [3]. Clusters are, in fact, a bridge between single atoms or molecules and the familiar bulk matter. As such, they possess unique properties and considerable effort has gone into understanding the evolution of their properties with size—in particular, within the context of phase transitions [4–11]. This quest to understand the transition from quantum to classical objects has remained one of the most fundamental motivations in the field cluster science.

A second motivation for studying clusters is related to the understanding and control of catalysis [13]. The large surface area to volume ratio and selective properties of clusters, especially metal clusters, could be tailored to

catalyse certain chemical reactions. Related to this, is the study of how the doping of clusters with dopants of different size or type affects the electronic, geometric and thermodynamical properties of the host clusters, allowing one to control and tune clusters to exhibit specific properties [14, 15].

Finally, much of cluster science overlaps with the realm of nanotechnology, the fabrication and manipulation of structures and devices on the nanoscale. In both fields, nanocarbon systems are the *de facto* driving force behind the surge of interest and investigations, of which the discovery of fullerenes can be considered to have sparked the nanotechnology revolution. While carbon nanotubes and graphene may currently have taken the forefront in the nanotechnology rush [16], fullerenes remain one of the most fundamental and interesting objects of research and is the particular focus of this thesis.

## 1.2 UNDERSTANDING FULLERENES

With more than 100,000 publications on its subject matter alone [17], the fullerene molecule  $C_{60}$  has fuelled a new area of research. Its serendipitous discovery, twenty-five years ago, in an experiment to recreate the environment of carbon stars was rewarded with a Nobel Prize in 1996 [12, 18–20]. Nonetheless, conjectures of its existence have been around since 1966 [21], as well as theoretical work regarding its stability [22, 23] and electronic structure [24–26].

Topologically, the  $C_{60}$  molecule is a truncated icosahedron where each of the 60 carbon atoms is bonded to three others, creating a trivalent network of bonds akin to that of graphite. However, unlike graphite, fullerenes contain pentagonal rings alongside hexagonal faces. Indeed, this is in accordance to Euler’s theorem on spherical polyhedra. For a closed cage structure to form, the number of vertices  $v$ , edges  $e$  and faces  $f$  must be related by

$$v + f = e + 2, \tag{1.1}$$

where in this case,  $v$  is simply the number of atoms and  $e$  is the number of bonds. The number of faces can be further defined as  $f = \frac{5}{6}p + h + 2$ , where  $p$

is the number of pentagons and  $h$  is the number of hexagons in the fullerene. It can then be trivially shown that, for a closed cage structure of  $v$  atoms to form, the trivalent network must contain 12 pentagonal and  $(v/2 - 10)$  hexagonal faces. For the  $C_{60}$ , this corresponds to 90 carbon-carbon bonds distributed as 12 pentagons and 20 hexagons in the cage structure.

The distribution of these 12 pentagonal rings in the  $C_{60}$  leads to 1812 possible isomers (excluding permutation-inversion isomers). Of these, there is only one isomer where each of the 12 pentagons are equally separated from each other by a hexagonal ring. This  $\mathcal{I}_h$ -symmetric isomer is known as the *buckminsterfullerene* and is the only stable isomer of the  $C_{60}$  which can be produced in macroscopic quantities. In general, fullerenes with a similar hexagon-pentagon distribution, *i.e.* displaying no adjacent pentagons, are particularly stable and fulfil the so-called “Isolated Pentagon Rule” (IPR). However, it is known that for charged fullerenes and endohedral/exohedral fullerenes, the most stable form of the fullerene cage may not necessarily be an IPR-structure.

Due to the pentagonal rings in its structure, the  $C_{60}$  possesses two different types of bonds that alternate throughout the trivalent network. These two bonds correspond to sixty (5 – 6) bonds of length 1.45-1.49 Å, and thirty (6 – 6) bonds of length 1.38-1.40 Å. The (5-6) bonds are named as such because they are formed by the edges of a pentagon and a hexagon; while the (6-6) bonds correspond to the edges of two hexagons. These bonds are also referred to as “single” and “double” bonds respectively. The  $C_{60}$  has 240 valence electrons, of which there are 60 delocalised  $\pi$ -orbitals; and 180 degrees of freedom, of which 6 are the translational and rotational degrees of freedom, and the remaining 174 are the vibrational degrees of freedom—though with only 46 distinct frequencies. These properties, together with its unique structure, makes  $C_{60}$  a particularly interesting system to study. Nonetheless, despite twenty-five years of intense research, the  $C_{60}$  molecule remains elusive—with many fundamental questions regarding its formation, stability, energy absorption and subsequent redistribution persisting without definitive answers. Of these open questions, the mystery of fullerene formation continues to be an issue of long-standing dispute.

### 1.2.1 MAKING FULLERENES

The gas-phase formation mechanism of  $C_{60}$  has attracted considerable attention since the discovery of fullerenes in 1985—where the fullerene molecules were produced through laser-ablation of graphite. In this technique, a graphite disk is rotated slowly to provide a vapourisation target for a laser pulse. Meanwhile, a buffer gas of helium is pumped into the vapourisation zone and carries away with it the produced carbon vapour (or carbon plume) which then condenses into clusters. The gas then supersonically expands into a vacuum chamber and is afterwards identified using mass spectroscopy [12, 19, 20]. However, the yields of fullerenes produced using laser-ablation of graphite is often minimal.

A milestone in fullerene research occurred a few years later through the discovery that a simple arc-discharge of graphite electrodes could produce macroscopic amounts of fullerenes [27]. The arc-discharge technique consists of two graphite electrodes contained within a chamber with a small gap between them. Each rod is connected to a motor in order to control the size of the gap. The chamber is evacuated and then filled with a helium buffer gas. When a current is passed through the graphite rods, an arc is formed in the region of the gap where temperatures are more than 5000 K at the centre of the arc, and around 4000 K at the arc periphery [28]. The evaporated carbon vapour is carried away from the arc region by the buffer gas which simultaneously cools the vapour. The cooled vapour then condenses on the cooler regions of the chamber, *e.g.* the glass dumbbell. At the end of the reaction, the soot is collected and fullerenes are extracted using chromatographic methods. Yields using the arc-discharge technique is on the range of 15-30% of fullerenes, hence, this method has been widely used to generate fullerenes.

In both of these techniques, it was observed that the final yields of fullerenes showed an unusually large proportion of  $C_{60}$  compared to any other fullerene size. Therefore, any proposed mechanism of fullerene formation requires an explanation on two points. The first being the actual mechanism by which a closed cage structure can be formed, while the second is an ex-

planation for the unique yields of  $C_{60}$  in comparison to all other fullerenes. In the following, we outline a few prominent formation mechanisms:

- **The Pentagon Road:** small carbon species of C,  $C_2$  and  $C_3$  form linear chains which react with each other to form carbon rings. Further reaction of these rings leads to growth of the structure to 25-40 atoms. In this domain, the polycyclic network evolves into the thermodynamically favourable graphene-like sheet. The graphene-like sheet is driven to reduce the number of dangling bonds by closing up the structure. To do so, it incorporates pentagonal faces which leads the sheet to curl up into open graphitic cups/bowls. These open structures continue to react with the available precursor molecules while eliminating defects in the network through Stone-Wales transformations or the evaporation of  $C_2$  (also known as ‘Shrink-wrapping’). With the correct conditions, these graphitic cups will be able to anneal into fullerenes. As  $C_{60}$  is the first fullerene fulfilling the “Isolated Pentagon Rule”, most of the graphitic cups will end its growth—thus its reactivity—by transforming into the stable  $C_{60}$  molecule.
- **The Fullerene Road:** Similar to the Pentagon Road, however, instead of the transformation into graphitic cups, this mechanism assumes that the graphene-like structures transforms into small non-IPR fullerenes which are reactive, thus unstable. The sites where there are two adjacent pentagons in these fullerenes serve as activation sites for the incorporation of  $C_2$  molecules or small rings/chains. As these small fullerenes grow,  $C_{60}$  is a special stopping place in the growth kinetics as it is the first fullerene which obeys the IPR by having no adjacent pentagons.
- **Ring Stacking:** In this mechanism, a fullerene is assumed to be formed by the sequential stacking of an appropriate number and combination of mono-cyclic carbon rings. These rings stack up to make a network of only pentagons and hexagons and is then terminated by a  $C_2$  to form a  $C_{60}$ . However, if the ring-stack is not immediately termi-

nated by  $C_2$ , then the sequential addition of more  $C_2$  units will lead to the formation of the next IPR-fullerene, *i.e.*  $C_{70}$  and so on [29, 30].

- **Shrinking Hot Giant:** The Shrinking Hot Giant mechanism consists of a “Size-up” and a “Size down” sub-mechanisms. In the “size up” part, giant fullerene-like structures self-assemble through reactions of rings and chains structures. However, these giant fullerene-like structures contain many defects and attached dangling chains. In the “size down” part, these structures anneal through bond transformations and ‘shrink-wrapping’—evaporation of successive  $C_2$  molecules—which shrinks the structure down to sizes of  $C_{70}$  and  $C_{60}$  and causes the removal of the attached dangling chains.

In all these mechanisms, two underlying processes are immediately obvious: that there is a “bottom up” process in which fullerenes are built from small precursors, and a “top down” process in which there is an evaporation of small carbon units leading to a “shrink-wrapping” of the fullerene. In fact, both processes may be interdependent and occur together, as in the Shrinking Hot Giant mechanism.

Experimentally, evidence of the “bottom up” process has been provided by isotopic scrambling experiments using normal and  $^{13}C$ -enriched graphite electrodes. While the ‘shrink-wrapping’ of the “top down” process has been observed through successive  $C_2$  evaporation of a giant fullerene trapped within a nanotube, heated to temperatures of around 2000 K [31]. Nonetheless, verification of these processes are not conclusive in determining which, or if any, of the proposed mechanisms is the correct one during fullerene formation.

Aside from the microscopic mechanism of fullerene formation, the local environment of the carbon vapour produced through either laser-ablation of graphite or arc-discharge may influence the obtained yields of fullerenes. In particular, the pressure and temperature of the buffer gas should affect the annealing process of the hot carbon vapour produced from the graphite, as these two parameters determine the collision frequency between among the carbon clusters, thus influencing the rate of cooling and growth of the clus-



ters. The temperature of the buffer gas can be controlled by encasing the laser vapourisation target or the electrodes of the arc discharge within an over. Such techniques are known as the laser furnace and the arc furnace respectively, and have been used to study the effect of buffer gas pressures on the yields of  $C_{60}$ . While this is certainly an improvement in understanding fullerene growth, it is difficult to extricate the interdependent roles that factors such as the arc current, the volume of the cooling chamber and even size of the graphite electrodes influence upon the final yields of  $C_{60}$ .

Irrespective of these facts, neither laser ablation nor arc discharge are techniques that can be easily scaled up for industrial production. Instead, fullerenes are industrially mass-produced using combustions techniques involving the pyrolysis of methane, toluene, naphthalene or benzene in low-pressure sooting flames [32, 33]. Additionally, chemical synthesis methods to produce fullerenes have also been intensively investigated. In particular, methods using chemical vapour deposition have been successful in producing fullerenes, although these methods often require synthesising complicated precursor molecules as a pre-production step (for further details, see Ref. [34]. and references therein).

### 1.2.2 BREAKING FULLERENES

Experimental studies of fullerene stability have been conducted through laser-irradiation [35], thermal fragmentation [36] and through collisions of  $C_{60}$  with charged or neutral molecules [37–39], with surfaces and through electron impact.

On the timescale of tens of  $\mu s$ , excited fullerenes can decay through three competing channels:  $C_2$  evaporation (also known as 'fission' and 'shrink-wrapping'), thermionic emission (or delayed ionisation) and blackbody radiation (or radiative cooling) [38, 40–42]. At low temperatures, thermionic emission becomes a significant decay channel, though fullerenes dominantly decay through the sequential evaporation of  $C_2$  molecules, while retaining

their closed-cage structure:



where  $n$  is the number of atoms,  $C_n$  the parent molecule and  $C_{n-2}$  the daughter fragment. The fragmentation energy (also referred to as the  $C_2$  binding energy) of this reaction is defined as the difference between the energies of the products and reactants. Till 2002, there had been a large discrepancy between the theoretically calculated value of the  $C_2$  binding energy for  $C_{60}$  and the value determined experimentally. Theoretical calculations has placed the fragmentation energy at 11-12 eV, while the energies extracted from experiments were found to be significantly smaller, 7-8 eV. This difference in values was found to be attributed to the use of an incorrect value for the Gspann factor, which lowered the pre-exponential factor of the Arrhenius equation used in analysing the experimental data.

In collision experiments at low energies (of up to hundreds of eV), the unimolecular decay of positively-charged  $C_{60}^+$  leads to a bimodal fragment distribution. In such a pattern, one can observe fullerene fragments of  $C_{2n}^+$ , where  $n > 16$  and ring/chain fragments of  $C_n^+$ , for  $n < 32$ . The bimodal pattern can be explained in terms of successive loss of  $C_2$  from the  $C_{60}^+$  to an unstable  $C_{30}^+$  which then either disintegrates or cleaves into large cluster fragments. At high energies (on the scale of keV to MeV), fullerenes may also decay through multi-fragmentation [43, 44] of three or more clusters, as well as evaporate large neutral fragments such as  $C_4$  or  $C_6$ . In fact, at sufficiently high energies, the fullerene cage may simply undergo a catastrophic phase transition-like fragmentation, as seen in photo-dissociation experiments with ns laser pulses and also in experiments involving super-heated  $C_{60}$  vapours at 1900–2000 K.

Fullerene stability and its fragmentation have been investigated extensively by a variety of computational methods, notably tight-binding molecular dynamics [45–51]. Initial thermal fragmentation studies based on tight-binding methods were performed by Wang *et al.* in which the  $C_{60}$  was found to be stable against spontaneous disintegration for temperatures up

to 5000 K [47]. This was followed by similar studies by Zhang *et al.* for fullerenes ranging from  $C_{20}$  to  $C_{90}$  where, for small fullerenes ( $n \leq 58$ ) it was discovered that the fragmentation temperature increased linearly. However, for larger fullerenes ( $n=60$  and  $n \geq 70$ ), the temperature stabilised around 5500 K [45, 46]. Both studies employed the TB-parametrisation of Xu *et al.* [52], as are the work conducted by László [50] and Openov and Podliyaev [51] for the canonical and microcanonical ensembles respectively. Kim *et al.* reported structural changes in the  $C_{60}$  and  $C_{70}$  in the range of 3000 and 4000 K—with the onset of bond breaking around 5000 K [49]. While, Kim and Tomànek conducted fragmentation simulations of the  $C_{20}$ ,  $C_{60}$  and  $C_{240}$  and found several different phases of the fullerene melting process, including a liquid-like pretzel phase [48]. Semi-empirical bond-order methods, such as the Tersoff [53, 54] and Brenner [55] potentials, are also used in studying the thermal fragmentation of fullerenes [56–59].

Fragmentation induced by radiation have been also been investigated [60, 61]. Xu and Scuseria conducted photofragmentation simulations of the  $C_{60}$  and observed sequential loss of  $C_2$  units with cage fragmentation occurring for  $T > 5600$  K [60]. While, Horvát and Beu reported multi-fragmentation to be the main disintegration channel at high excitation energies. However, between excitation energies of 100–120 eV, they reported the occurrence of a phase transition where they had defined phase transition to be a steep drop in the average fragment size with temperature (in their work, the average fragment size dropped from 60 to 5 between 100–120 eV) [61]. Other notable fragmentation studies involved collisions with surfaces [62, 63], as well as collisions with molecules [64].

### 1.2.3 USING FULLERENES

While fullerenes may be the first nanocarbon allotrope that was discovered and intensively researched, much of fullerene-based applications are still within a development phase. This is in contrast with the rapid progression of carbon nanotube-based applications. The stalwart growth of fullerene-based applications can be attributed to the difficulties in synthesising fullerenes

larger than  $C_{60}$ , the cost of the material and the more accessible availability of larger nanotubes and nanodiamonds. However, fullerene applications have been steadily gaining ground and in the following, we highlight some of the most promising applications of fullerenes.

The conversion of fullerenes to diamond, as well as the generation of ultra-hard material from fullerenes have garnered considerable attention. Phase transition-like transformations of fullerenes to diamonds require either high temperatures, or high pressures (on the scale of GPa), or both. Fullerenes are either used as the source material for transformation to diamonds [65–69] or as catalysts in the process [70–72]. Novel fullerene-based ultra-hard material have been found which exceed the hardness of diamonds [73–75].

Endohedral fullerenes—fullerenes with encapsulated atoms and in particular, N and P encapsulated atoms—have also been investigated as potential qubits in the functional quantum architecture of quantum computers [76–79]. Fullerenes have also been used in the construction of sensors to detect organic molecules, metal ions and anions [80, 81], as well as odorant molecules [82] (for a more comprehensive review, see Refs. [83, 84]. and the references therein).

$C_{60}$  and certain  $C_{60}$  derivatives have been shown to suppress replication of HIV through inhibition of HIV enzymes [85–90]. In addition to this antiviral property, cationic fullerene derivatives have been demonstrated to inhibit bacterial and tumour cell growth [91]. The highly antioxidant property of fullerenes has led it to be called a *radical sponge* [92] which can be used as a medical antioxidant. In fact, fullerene-derivatives have been shown to protect rodent liver cells against free radical damage [93] and protect cell growth from apoptotic-induced injuries [94–98].

The hollow of the carbon cage has often been envisioned for the use of drug delivery within the body. However, the difficulties in producing endohedral fullerenes has led to little progress within this domain. Nonetheless, derivitised fullerenes are known to be able to cross the cell membrane and bind to the mitochondria [99]. This effect has been exploited in a study that demonstrated a non-viral gene delivery using a fullerene-derivative bound to a plasmid vector DNA [100]. Additionally, fullerenes were found to be able

to penetrate through intact skin—a property that is promising for further developments in drug and gene delivery [101, 102].

### 1.3 THESIS OVERVIEW

The thesis progresses as follows.

In Chapter 2, I describe the computational methodology used in investigating the phase transitions of nanocarbon systems. Specifically, I discuss the molecular dynamics methods, the empirical potentials used in modelling carbon-carbon bonding and the specific simulation parameters that are used in setting up and running the simulations for this work.

In Chapter 3, I outline the fundamental ideas of phase transitions in finite systems and introduce *dynamic phase coexistence* which occurs at the phase transition temperature of nanoclusters.

Chapter 4 is devoted to the discussion of phase transitions in the buckminsterfullerene  $C_{60}$ . In this chapter, results of the molecular dynamics simulations and a statistical mechanics model of the  $C_{60} \leftrightarrow 30C_2$  phase coexistence will be analysed and discussed.

In Chapter 5, I extend the discussion of phase transition in  $C_{60}$  to fullerenes of sizes  $C_{32}$  to  $C_{540}$ , and I attempt to provide insights regarding the stability of fullerenes and their formation mechanisms in lieu of the molecular dynamics results. The discussion is then extended to clusters of 240 carbon atoms in the structural forms of: a fullerene, a nanotube, a buckyball and a graphene sheet.

In Chapter 6, I discuss how the presence of carbon affects the melting temperature of metal nanoclusters—specifically  $Ni_{147}$ . This is relevant in understanding the growth mechanism of various nanocarbon structures, such as nanotubes and large fullerenes, that grow with higher abundance when a catalytic metal cluster is present.

Finally in Chapter 7, I summarise the achievements of the work described in this thesis and suggests directions for future research.

I hope the organisation of the chapters and the materials presented will illustrate how phase transitions can be considered as a framework in which

the structure of nanocarbon systems, their dynamics and thermodynamical properties are intimately related. Although the approach of this work is essentially theoretical and computational, throughout the thesis I have attempted to relate the results of the simulations and models to experimental findings. Indeed, the hope is that the results of the work can provide further understanding of the rich behaviour of nanocarbon systems.

## CHAPTER 2

# METHODS

Computational methods have become an indispensable tool when investigating material at the nanoscale. It has facilitated the understanding and the prediction of behaviours and properties of an ever-growing class of new carbon-based structures [12, 103–105]. While the advances in computational technology has made calculations more efficient and viable, the *ab initio* level of computation remains daunting and computationally expensive when considering problems where there are a large number of atoms, or when one requires long simulations or statistical averages. Consequently in this work, empirical potentials have been used for studying the various nanocarbon structures of interest.

In Section 2.1, the foundations of molecular dynamics is presented. This is followed by a discussion of the empirical potentials used in this work, namely the Tersoff potential, in Section 2.2; and the *Topologically-constrained force-field*, a novel potential that we developed for the description of bonding in fullerenes, in Section 2.3. In Section 2.4, we introduce the Sutton-Chen potential which was used in the study of how carbon affects a metal nanocluster. Finally in Section 2.1, we discuss the details of the molecular dynamics simulations that we have conducted.

## 2.1 MOLECULAR DYNAMICS

Molecular dynamics is a computational technique to simulate the dynamical evolution of  $N$  atoms by integrating their classical equations of motion,

$$\mathbf{F}_i = m_i \mathbf{a}_i, \quad (2.1)$$

where  $i$  represents an atom from a total of  $N$  atoms in the system,  $m_i$  is the mass of the atom,  $\mathbf{a}_i = d^2\mathbf{r}_i/dt^2$  is the corresponding acceleration of the atom and  $\mathbf{F}$  is the force acting upon  $i$  due to interactions with the other  $(N - 1)$  atoms in the system. Thus, given an initial set of atomic coordinates and velocities, the dynamical evolution of a system—its *trajectory*—is, in principle, completely deterministic, and is calculated within a  $6N$ -dimensional phase space, consisting of  $3N$  positions and  $3N$  momenta.

The main motivation behind molecular dynamics is that it can be used to explore the macroscopic properties of a system, such as its thermodynamic and kinetic properties. The connection between molecular dynamics and macroscopic observables is provided via statistical mechanics. With molecular dynamics, one can obtain a set of configurations distributed according to a particular statistical ensemble, such as the microcanonical ensemble (NVE) characterised by a constant number of atoms  $N$ , a constant volume  $V$  and a constant energy  $E$ ; or a canonical ensemble (NVT) characterised by constant  $N$ ,  $V$  and temperature  $T$ .

The foundational principle of this connection is the *ergodic hypothesis*, which assumes that the time-averages of a system is equivalent to the statistical ensemble averages,

$$\langle A \rangle_{ensemble} = \langle A \rangle_{time} \quad (2.2)$$

where  $\langle A \rangle$  represents a macroscopic observable. This assumption is valid, in general, when the dynamical trajectory of the system approaches infinite time. More realistically, for finite-time simulations, it is important that the system's trajectory has sufficiently explored its phase space, such that the time averages of the observables can be correctly equated to the ensemble



averages.

In this section, we first discuss the general interactions between the atoms in the system as described using a *potential*. We then present the time-integration methods used to propagate the atomic coordinates in the simulations. Next, we discuss the use of a thermostat to control the temperature fluctuations in order to generate a canonical (NVT) ensemble. We finish the section by describing a few important observables that can be calculated from the simulated trajectories.

### 2.1.1 ATOMIC INTERACTIONS

In general, the interactions within the system is given by the potential  $V$ , which can be divided into *non-bonded* and *bonded* contributions. From the potential, the forces  $\mathbf{F}_i$  can then be derived as the gradients of the potential with respect to atomic coordinates,

$$\mathbf{F}_i = -\nabla_{\mathbf{r}_i} V(\mathbf{r}_1, \dots, \mathbf{r}_N). \quad (2.3)$$

The non-bonded interaction is often described as the summation of two-body (pairwise) interactions over all atoms, a common example being the Lennard-Jones (LJ) potential:

$$V_{LJ}(r_{ij}) = \epsilon \left[ \left( \frac{\sigma}{r_{ij}} \right)^{12} - 2 \left( \frac{\sigma}{r_{ij}} \right)^6 \right], \quad (2.4)$$

where  $r_{ij} = |\mathbf{r}_i - \mathbf{r}_j|$  is the interatomic distance between atoms  $i$  and  $j$  and  $\sigma$  is the equilibrium distance corresponding to the minimum energy  $\epsilon$  (the well depth).

If electrostatic charges are present, the appropriate Coulomb potential is also added to the nonbonded interaction,

$$V_{Coulomb}(r_{ij}) = \frac{Q_1 Q_2}{4\pi\epsilon_0 r_{ij}}, \quad (2.5)$$

where  $Q_1$  and  $Q_2$  are the charges and  $\epsilon_0$  is the permittivity of free space.

However, in this work, we focus on neutral nanocarbon systems, thus electrostatic interactions are not accounted for.

The bonding interactions within the system are often more complex and may involve many-body effects. An example of a simple bonding potential is a molecular mechanics forcefield. Here, the contribution to the intramolecular bonding potential is separated into a “chemical bond” term and an angular term (often modelled as harmonic oscillators), as well as a torsional/dihedral term,

$$\begin{aligned}
 V_{intra-bond} &= \frac{1}{2} \sum_{bonds} k_{ij}^b (r_{ij} - r_{eq})^2 \\
 &+ \frac{1}{2} \sum_{angles} k_{ijk}^a (\theta_{ij} - \theta_{eq})^2 \\
 &+ \frac{1}{2} \sum_{dihedral} \sum_m k_{ijkl}^d (1 + \cos(m\theta_{ijkl} - \gamma_{eq})),
 \end{aligned} \tag{2.6}$$

where  $k$ ,  $r_{eq}$ ,  $\theta_{eq}$ ,  $\gamma_{eq}$  are specific parameters that are collated in the forcefield for different atomic interactions. Other interactions such improper torsions or explicit terms for hydrogen bonding may also be included. In fact, there are a variety of molecular mechanics forcefields (*e.g.* CHARMM, AMBER, GROMOS) that are used to describe different systems, such as DNA and protein molecules. However, due to the construction of these forcefields, the system is not allowed to break and make new bonds.

The interatomic potential (both bonded and non-bonded) described above has infinite range. In practice, a cutoff radius  $R_c$  is often employed to neglect the interactions between atoms that are separated by a distance more than  $R_c$ . Nonetheless, a simple truncation of the interaction will create spurious results in the energy calculation, therefore a “switching” function is often employed. The purpose of the switching function is to smoothly truncate the interaction at the cutoff distance, such that between the switching distance  $R_s$ , where  $R_s < R_c$ , the potential is shifted and finally goes to zero at  $R_c$ .

Hence, when the interatomic distance between atoms  $i$  and  $j$  is more than the cutoff radius,  $r_{ij} > R_c$ , the molecular dynamics program skips the

expensive force calculation and moves on to the next atom, e.g.  $k$ , and checks if  $r_{ik}$  is more or less than the cutoff radius. However, the time to calculate each and every interatomic pair is time-consuming and inefficient. Thus, one may implement a *neighbours* list.

A simple implementation of the neighbours list is known as the *Verlet List*. As before, each atom is effectively surrounded by a cutoff sphere, which is a sphere with radius  $R_c$ . In addition to the cutoff sphere, there is an extra “skin” layer which gives a larger sphere of  $R_{list} = R_c + s$ , where  $s$  is the additional skin distance.

At the beginning of the simulation, the Verlet list is constructed by listing all the neighbours of each atom that are within  $R_{list}$ . Over the next few time steps in the molecular dynamics simulation, only the pairs of atoms in the list are checked to see if they are within  $R_c$ . Hence whether a force calculation is necessary or not necessary for that particular pair. From time to time, the Verlet list is updated and reconstructed to ensure that all interactions are properly accounted for.

In this thesis, we have used the many-body Tersoff potential [53, 54] to describe the covalent bonding in the nanocarbon systems of interest. In contrast to molecular mechanics forcefields, the Tersoff potential was constructed in order to allow the simulated system to make and break bonds. We have also developed the *Topologically-constrained* forcefield to describe a “constrained”-fullerene model—specifically a model of  $C_{60}$ . Detailed presentation and discussion of the Tersoff potential and the Topologically-constrained forcefield are given later in Sections 2.2 and 2.3 respectively.

### 2.1.2 TIME IN MOLECULAR DYNAMICS

At the core of any molecular dynamics program is algorithm to integrate the classical equations of motion of the interacting particles in the system. Time-integration algorithms are based on finite difference methods, discretising time on a finite grid, where time  $t$  is separated from time  $t + 1$  by a finite *timestep*,  $\Delta t$ . This then allows the generation of the system trajectory by iterating the procedure.

All algorithms assume that the atomic positions and dynamical properties can be approximated as Taylor series expansions:

$$\begin{aligned}
 \mathbf{r}(t + \Delta t) &= \mathbf{r}(t) + \mathbf{v}(t)\Delta t + \frac{1}{2}\mathbf{a}(t)\Delta t^2 + \dots & (2.7) \\
 \mathbf{v}(t + \Delta t) &= \mathbf{v}(t) + \mathbf{a}(t)\Delta t + \frac{1}{2}\mathbf{b}(t)\Delta t^2 + \dots \\
 \mathbf{a}(t + \Delta t) &= \mathbf{a}(t) + \mathbf{b}(t)\Delta t + \frac{1}{2}\mathbf{c}(t)\Delta t^2 + \dots \\
 \mathbf{b}(t + \Delta t) &= \mathbf{b}(t) + \mathbf{c}(t)\Delta t + \dots
 \end{aligned}$$

where  $\mathbf{r}$  is the position,  $\mathbf{v}$  is the velocity (the first derivative of position with respect to time),  $\mathbf{a}$  is the acceleration (the second derivative),  $\mathbf{b}$  is the third derivative, and so on.

A widely-used integration algorithm is known as the Verlet algorithm. In this method, two Taylor expansions of the atomic positions are used—one forward in time and the other backward,

$$\begin{aligned}
 \mathbf{r}(t + \Delta t) &= \mathbf{r}(t) + \mathbf{v}(t)\Delta t + \frac{1}{2}\mathbf{a}(t)\Delta t^2 + \dots & (2.8) \\
 \mathbf{r}(t - \Delta t) &= \mathbf{r}(t) - \mathbf{v}(t)\Delta t + \frac{1}{2}\mathbf{a}(t)\Delta t^2 - \dots
 \end{aligned}$$

Adding both equations then gives

$$\mathbf{r}(t + \Delta t) = 2\mathbf{r}(t) - \mathbf{r}(t - \Delta t) + \mathbf{a}(t)\Delta t^2 + O(\Delta t^4). \quad (2.9)$$

However, velocities are not explicitly generated by the Verlet algorithm, but can be computed in a number of ways, the simplest of which is

$$\mathbf{v}(t) = \frac{\mathbf{r}(t + \Delta t) - \mathbf{r}(t - \Delta t)}{2\Delta t}. \quad (2.10)$$

In this thesis, we have mainly used the *velocity Verlet* algorithm, also known as Leapfrog method. The velocity Verlet algorithm is based on the original Verlet algorithm, however here, the velocities are directly incorporated within the method. To implement this algorithm, the velocities  $\mathbf{v}(t + \frac{1}{2}\Delta t)$  are calculated from the velocities at time  $(t - \frac{1}{2}\Delta t)$  and the acceleration at time  $t$ . The positions  $\mathbf{r}(t + \Delta t)$  can then be determined from the velocities  $\mathbf{v}(t + \frac{1}{2}\Delta t)$

as follows

$$\begin{aligned}\mathbf{r}(t + \Delta t) &= \mathbf{r}(t) + \mathbf{v}(t + \frac{1}{2}t)\Delta t, \\ \mathbf{v}(t + \frac{1}{2}\Delta t) &= \mathbf{v}(t - \frac{1}{2}t)\Delta t + \mathbf{a}(t)\Delta t,\end{aligned}\tag{2.11}$$

and the velocities and accelerations at  $t + \Delta t$  are given as

$$\begin{aligned}\mathbf{a}(t + \Delta t) &= -(1/m)\nabla V(\mathbf{r}(t + \Delta t)), \\ \mathbf{v}(t + \Delta t) &= \mathbf{v}(t + \Delta t/2) + (1/2)\mathbf{a}(t + \Delta t)\Delta t.\end{aligned}\tag{2.12}$$

## 2.2 BOND-ORDER POTENTIALS

The concept of bond order is one of the basic qualitative measures of the strength of a bond. The bond strength, in turn, is related to the bond dissociation energy, hence the bond length. In the early 1930s, Pauling introduced a simple empirical function to describe the correlation between bond order and bond length [106]:

$$b_p = \exp^{-(r-r_0)/\alpha}\tag{2.13}$$

where  $b_p$  is known as the ‘‘Pauling bond order’’,  $r$  is the length of the bond,  $r_0$  its equilibrium bond length and  $\alpha$  is an empirical parameter which is fitted for different molecules.

The bond order-bond length correlation is used particularly in theories of chemical reaction. In stable molecules, the bond orders are close to integer numbers. However, when a bond is formed or broken, not only does the bond length change, but the bond order changes as well—from its stable integer value to a non-trivial, non-integer value that is characteristic of a bond found in a transition structure.

Although the concept of bond order was first formulated as an empirical function, its quantum mechanical definition has been determined to be the total overlap population between two atoms within the framework of the Mulliken population analysis [107]. However, in the following discussion we focus instead on formulating the bond order as function of the local environment

of the bonding atoms.

The formulation of the bond order in terms of the local environment was introduced by Abell in his general model of bonding energetics, based on chemical pseudopotential theory [108]. The model assumes that the total binding energy of a system can be written as a sum over the individual bonds, where the energy of each bond is composed of pairwise repulsive and attractive contributions, mediated by the bond order. This bond-order term depends upon the “primary interaction topology” of the molecule. In other words, the intra-atomic interaction topology of the system is *restricted* to only the nearest neighbours, which is given by the “coordination number” of the atom—a comparable concept to the *Topologically-constrained forcefield* which we introduced in the previous section.

In the following section, we present and discuss the Tersoff potential [53, 54], highlighting its successful application in a wide variety of carbon systems. In Section 2.2.2, we consider the limitations inherent in the Tersoff potential and outline a series of bond-order potentials which were developed as extensions and intended corrections to the Tersoff potential.

### 2.2.1 THE TERSOFF POTENTIAL

Based on bond-order concepts, Tersoff introduced an empirical forcefield which could, in principle, handle the making and breaking of bonds based on the changes in the value of the bond order. In his formulation, the bond order term is *parametrised* in a many-body scheme depending upon the local atomic environment of the bond—conceived as the dependence on the number on nearest neighbours and an angular contribution.

In the Tersoff potential, the total energy  $E$  of a system is given by the sum of the interaction energy  $V$  between all pairs of bonded atoms. In equation (2.14),  $i$  and  $j$  refer to a pair of atoms whose interatomic distance is given by  $r_{ij} = |\mathbf{r}_i - \mathbf{r}_j|$ .

$$E = \frac{1}{2} \sum_i \sum_{j \neq i} V_{ij} \quad (2.14)$$

The interaction energy  $V_{ij}$  between atoms  $i$  and  $j$  is then expressed as the interplay between the repulsive pair potential  $f_R$ , the attractive pair potential  $f_A$  and the bond order term  $b_{ij}$ . This is written as

$$V_{ij} = f_C(r_{ij}) [f_R(r_{ij}) + b_{ij}f_A(r_{ij})]. \quad (2.15)$$

The term  $f_C$  is a smooth cutoff function whose purpose is to limit the range of the potential, since short-ranged functions confer a tremendous reduction in computational efforts. The function has a continuous value between 0 and 1 for a small range around  $R$ , where  $R$  is taken to include only the first-neighbour shell for most structures.  $D$  is the “skin” of this range, such that atoms within the vicinity of bonding is accounted for.

$$f_C(r_{ij}) = \begin{cases} 1, & r_{ij} < R - D \\ \frac{1}{2} - \frac{1}{2} \sin\left(\frac{\pi}{2}(r_{ij} - R)/D\right), & R - D < r_{ij} < R + D \\ 0, & r_{ij} > R + D. \end{cases} \quad (2.16)$$

The repulsive  $f_R$  and attractive  $f_A$  potentials are expressed in an exponential form as this has the useful feature of leading automatically to a “universal” bonding behaviour [109]. They are given as follows

$$f_R(r_{ij}) = A \exp(-\lambda_1 r_{ij}), \quad (2.17)$$

$$f_A(r_{ij}) = -B \exp(-\lambda_2 r_{ij}). \quad (2.18)$$

where  $A$ ,  $B$ ,  $\lambda_1$  and  $\lambda_2$  are parameters whose values are given in Table 2.2.1, together with the values of  $R$  and  $D$  and the remaining five parameters which are found in the bond order term.

The effect of the local environment of the bonding atoms on the bond strength is encapsulated in the many-body bond order term  $b_{ij}$ , expressed as

$$b_{ij} = (1 + \beta^n \zeta_{ij}^n)^{-1/2n}, \quad (2.19)$$

where  $\beta$  and  $n$  are parameters given in Table 2.2.1 and  $\zeta_{ij}$  is the coordination

A	B	R	D	$\lambda_1$	$\lambda_2$	$\lambda_3$
1393.6 eV	346.74 eV	1.95 Å	0.15 Å	3.4879 Å	2.2119Å	0
n	h	c	d	$\alpha$	$\beta$	
0.727510	-0.57058	38049	4.3484	0	$1.5724 \times 10^{-7}$	

Table 2.1: Tersoff potential parameters for carbon

factor which is evaluated as follows

$$\zeta_{ij} = \sum_{k \neq i, j} f_C(r_{ik}) g(\theta_{ijk}) \exp[\lambda_3^3 (r_{ij} - r_{ik})^3], \quad (2.20)$$

where  $k$  denotes another atom which is also bonded to atom  $i$ ,  $\lambda_3$  is a parameter and  $\theta_{ijk}$  is the bond angle spanned by bonds  $ij$  and  $ik$ . The bond angle function  $g(\theta_{ijk})$  is further expressed as

$$g(\theta_{ijk}) = 1 + \frac{c^2}{d^2} - \frac{c^2}{[d^2 + (h - \cos\theta_{ijk})^2]} \quad (2.21)$$

where  $c$ ,  $d$  and  $h$  are parameters with values given in Table 2.2.1. The parameter  $c$  determines the strength of the angular effect, while  $d$  determines how sharp the dependence on angle is. The parameter  $h$  is formally the cosine of the energetically optimal angle. It should be noted that the parameter  $\lambda_3$  is set to 0. Therefore, the coordination factor  $\zeta$  is dependent only upon the number of nearest neighbour atoms (encapsulated in the cutoff  $f_C$ ) and the bond angle term  $g(\theta_{ijk})$ .

The dependence of  $b_{ij}$  on the coordination number is straightforward: if atom  $i$  has two neighbours  $j$  and  $k$  that compete to form a bond with  $i$ , then, if both atoms succeed in forming bonds  $ij$  and  $ik$ , the strength of either bond is weaker compared to a bond formed *exclusively* when there are no other competing atoms, *e.g.* a two-atom case. The addition of the bond angle term  $g(\theta_{ijk})$  was done in order to stabilize open lattices against shear distortion,



and to model elastic properties and defect energies with reasonable accuracy. It should be noted, however, that in the formalism introduced by Abell, there are no angular terms.

### 2.2.2 POST-TERSOFF POTENTIALS

The Tersoff potential has been used extensively to describe various carbon systems, such as graphite, diamond, fullerenes and nanotubes [58, 110–114]. It has been found to successfully describe the cohesive energy and bond lengths of  $C_{60}$  molecules. Furthermore, the Raman spectrum of  $C_{60}$  calculated using the Tersoff potential is in good agreement with the observed spectrum in the low-energy regions corresponding to bond-bending modes, although it is less accurate in describing bond-stretching and shearing modes [115].

The Tersoff potential suffers from two drawbacks: (i) overbinding of radicals and (ii) inaccurate treatment of conjugacy. This becomes clear when the potential is applied to hydrocarbons. When applied to the radical  $C_2H_5$ , the Tersoff potential considers the carbon-carbon bond as half the bond strength of a single C-C and a double C=C bond, when in reality, this bond is only a single C-C bond. Secondly, because of the way the Tersoff potential calculates the coordination number of the carbon atoms, it misidentifies the carbon-carbon bond between, e.g., graphite and  $(CH_3)_2C=C(CH_3)_2$  because the local environment about both bonds gives the same coordination number, although the bond in  $(CH_3)_2C=C(CH_3)_2$  is a double bond, contrary to that of graphite.

The Brenner potential [116] attempts to alleviate these problems by the addition of two *ad hoc* parameter groups  $F_{ij}$  and  $H_{ij}$  into the bond order term of the original Tersoff potential. Moreover, the parameters for pure carbon were refitted in the Brenner potential. While the addition of these 23 extra parameters allows for the correct description of a selected group of small hydrocarbons, the problems of overbinding and conjugacy remain, in general, unsolved.

In addition to these two limitations, both the Tersoff and Brenner po-

tentials are unable to describe dispersion and nonbonded repulsions that are important for *intermolecular* interactions. In response to this, the adaptive intermolecular reactive bond order potential (AIREBO) [117] was developed by Stuart *et. al.* based upon a then-incomplete improvement of the Brenner potential by Brenner *et. al.*, which would be published two years after AIREBO in a final form known as REBO [55]. AIREBO accounts for the nonbonded interactions via a van der Waals term (using the Lennard-Jones potential). In addition to this, it contains a four-body dihedral term to account for the torsional stiffness of a  $\pi$  bond against rotation. However, when applied strictly to carbon systems, the AIREBO potential fares worse compared to the REBO potential. The long-range nature of the AIREBO function as well as the extra 39 parameters which controls its screening, non-bonded and torsional functions make AIREBO significantly demanding in terms of computation, compared to the original Brenner and Tersoff potentials.

The completed form of the “second-generation” Brenner potential is called the reactive bond order potential, REBO [55]. This revised potential includes modified analytic functions for the intramolecular interactions and an expanded fitting database. Similar to AIREBO, it contains the four-body torsional term, although fitted with a more complicated spline function compared to AIREBO. Additionally, the three-body angular term of the original Brenner potential has been revised to include correction functions to account for under- and over-coordinated atoms.

## 2.3 THE TOPOLOGICALLY-CONSTRAINED FORCE-FIELD

The *Topologically-constrained Forcefield* (TCF) was developed to adequately describe the carbon-carbon interaction in fullerenes within a simple but effective framework.

Although empirical potentials that describe covalent bonding in carbon are readily available in the literature, these potentials can be overtly compli-

cated, and often contain *ad hoc* parameters whose physical basis are uncertain. In lieu of this, the topologically-constrained forcefield was developed with a minimal set of parameters and is composed solely of pairwise terms, thereby allowing for significant gains in computational time.

Much like Ref. [118], we have also developed a potential without angular dependence. To compensate for this, the topologically-constrained forcefield employs a repulsive “penalty” potential to prevent unphysical bonding angles, and a static neighbours list—hence fixing the coordination number (number of neighbours) per carbon atom. Additionally these constraints enabled us to restrict our system to the investigation of a single channel, in this case the  $C_{60} \leftrightarrow 30C_2$  channel, which will be elaborated in Section 4.

The topologically-constrained forcefield is given by

$$V(r_i) = \sum_{j \neq k, l, m}^N V_p(r_{ij}) + \sum_{j=k, l, m} V_{cov}(r_{ij}). \quad (2.22)$$

There are two types of interactions: the short-range *covalent* (cov) bonding and the long-range “penalty” interaction (p), which can also be thought of as a repulsive van der Waals interaction. The interatomic distance  $r_{ij}$  between atoms  $i$  and  $j$  is defined as  $r_{ij} = |r_i - r_j|$ . The sum in the covalent term is over the three nearest-neighbours of atom  $i$ : atoms  $k$ ,  $l$  and  $m$ ; while the sum in the penalty term is over the other  $(N - 4)$  non-neighbours of atom  $i$ . Hence, each atom is allocated 3 covalent nearest-neighbours, determined by their positions relative to atom  $i$ , and  $(N - 4)$  non-neighbours. In this way, the atom is *topologically-constrained* to interact with a certain type of bonding with certain atoms in the system.

Both short and long-range interactions in the system are modelled using the Lennard-Jones potential, though in principle, one may choose a different potential (e.g. the Morse potential), to model these interactions. The Lennard-Jones potential is given by:

$$V_{LJ}(r_{ij}) = \epsilon \left[ \left( \frac{\sigma}{r_{ij}} \right)^{12} - 2 \left( \frac{\sigma}{r_{ij}} \right)^6 \right], \quad (2.23)$$

Table 2.2: The fullerene forcefield parameters

$\sigma_s$ (Å)	$\epsilon_s$ (eV)	$\sigma_d$ (Å)	$\epsilon_d$ (eV)	$\sigma_p$ (Å)	$\epsilon_p$ (eV)
1.45	3.81	1.38	6.27	3.00	0.00052

where  $\sigma$  is the equilibrium distance corresponding to the minimum energy  $\epsilon$ .

As already discussed in the previous section, there are two types of bonds in the  $C_{60}$ : the “single” (5-6) bond and the “double” (6-6) bond. Hence, we have two different equilibrium parameters for the covalent interaction:  $\sigma_s$  and  $\sigma_d$  with corresponding minimum energy parameters  $\epsilon_s$  and  $\epsilon_d$ . The values of  $\sigma_s$  and  $\sigma_d$  reflect the equilibrium bond lengths of the single and double bonds in the  $C_{60}$  [119], while  $\epsilon_s$  and  $\epsilon_d$  are based on the carbon-carbon bond dissociation energies in ethane and ethene respectively [120]. All parameters of the forcefield are summarised in Table 2.2.

It should be noted that the topologically-constrained forcefield was jointly developed with a statistical mechanics model (presented in Section 4) which contains corrections to the entropy of the system. This is because we have set a fixed coordination number, which effectively entails a static neighbours list throughout the entire simulation. The fixed coordination restricts our system to the  $C_{60} \leftrightarrow 30C_2$  channel. Thus allowing us to perform sufficiently long molecular dynamics simulations of the system’s phase space in the vicinity of the “ $C_{60}$ ” and the “ $30C_2$ ” states. Therefore, each atom can only “form” and “break” bonds with its 3 specified covalent neighbors. Nevertheless, in principle the system should be allowed to form bonds with any 3 carbon atoms and not only the neighbors that were specified at the beginning of the simulation. As noted, this restriction is corrected in Section 4(a) using our statistical mechanics model

In principle, if we omit the topological constraint and consider all possible carbon bonding formations in the system, the fullerene will be just one among a myriad of other possible carbon clusters. Therefore the observation of the fullerene formation would become extremely difficult and the computa-

tional demands would be unfeasible because one would have to run numerous trajectories in order to observe a single fullerene formation event. Thus the topological constraint allows us to focus only on the fullerene formation channel without needing to account for all other possible structures. Although in the whole range of temperatures and pressures, the  $C_{60} \leftrightarrow 30C_2$  channel is not necessarily the most probable one. Therefore, the results of our work (presented in Section 4) should be understood as follows: “if the fullerenes are formed within this method, then they are formed at the temperatures and pressures presented in Section 4.3”.

Additionally, as our forcefield is based on central potentials, the transverse vibrational modes of the fullerene cage appears to be softer than in the case of, *e.g.* the Tersoff or tight-binding potentials. This will lead to a certain overestimation of the entropy of the cage state. However, in the present work we do not account for these corrections and leave this question for further consideration.

## 2.4 THE SUTTON-CHEN POTENTIAL

The Sutton-Chen potential [121] is a many-body potential that has been shown to reproduce bulk and surface properties of transition metals and their alloys with sufficient accuracy (see, *e.g.*, Refs. [122–126] and references therein). the Sutton-Chen model has the following form:

$$U_{pot} = \varepsilon \sum_i \left[ \frac{1}{2} \sum_{j \neq i} \left( \frac{a}{r_{ij}} \right)^n - c \rho_i^{1/2} \right], \quad (2.24)$$

where

$$\rho_i = \sum_{j \neq i} \left( \frac{a}{r_{ij}} \right)^m. \quad (2.25)$$

Here  $r_{ij}$  is the distance between atoms  $i$  and  $j$ ,  $\varepsilon$  is a parameter with dimension of energy,  $a$  is the lattice constant,  $c$  is a dimensionless parameter, and  $n$  and  $m$  are positive integers with  $n > m$ . The parameters provided by Sutton and Chen for nickel have the following values:[121]  $\varepsilon = 1.5707 \cdot 10^{-2}$

eV,  $a = 3.52 \text{ \AA}$ ,  $c = 39.432$ ,  $n = 9$ , and  $m = 6$ .

The Sutton-Chen potential is used in Chapter 6, when we discuss the effect of carbon on a nickel nanocluster. Additionally, the carbon-nickel interaction is modelled using the Morse potential:

$$V^{Ni-C}(r) = \varepsilon_M \left( (1 - e^{\rho(1-r/r_0)})^2 - 1 \right), \quad (2.26)$$

whose parameters were obtained by fitting the results of an *ab initio* density-functional calculation of the Ni-C interaction [127–129]. These parameters are  $\varepsilon_M = 2.431 \text{ eV}$ ,  $\rho = 3.295$ ,  $r_0 = 1.763 \text{ \AA}$ .

## 2.5 SIMULATION PARAMETERS

For the work exclusively concerning nanocarbon structures in Chapters 4 and 5, we have conducted extensive molecular dynamics simulations on a range of nanocarbon systems using the two forcefields that we have introduced in the previous sections: the *Topologically-constrained forcefield* and the Tersoff potential.

*The topologically-constrained forcefield.* Within the topologically-constrained forcefield, we performed constant-temperature molecular dynamics simulations for  $C_{60}$  with a timestep of  $\Delta t = 1 \text{ fs}$  and a total of  $5 \times 10^8$  steps to give a total simulation time of 500 ns. The system is equilibrated during the first 500 ps of the simulation, thus we have only considered data from the remaining trajectory in our analysis. The interaction cutoff was set to  $15 \text{ \AA}$  and the simulation was performed with a simulation box of either: (a) length  $20 \text{ \AA}$  per side, hence a volume of  $8 \times 10^3 \text{ \AA}^3$ , or (b)  $500 \text{ \AA}$  per side, hence a volume of  $1.25 \times 10^8 \text{ \AA}^3$ . Temperature control was achieved by means of the Langevin thermostat with a damping constant of  $100 \text{ ps}^{-1}$  [130, 131]. The simulations were conducted for temperatures between 2500 K and 8500 K. These simulations were conducted using NAMD [132].

*The Tersoff potential.* We have also conducted molecular dynamics simulations using the Tersoff potential for  $C_{60}$ . This was done in order to investigate the phase transition of  $C_{60}$  without the constraints imposed by our

statistical mechanics model and the topologically-constrained forcefield. In addition to this, we have also used this potential to investigate a series of fullerenes between  $C_{32}$  to  $C_{540}$  (Section 5), as well as five phases of nanocarbon consisting of 240 atoms (Section 5). As with the previous method, we have performed constant-temperature molecular dynamics simulations with a timestep of  $\Delta t=1$  fs. We have conducted different lengths of simulations, the longest being  $1\mu s$ , and the shortest being 50 ns. We have also considered three simulation box sizes: (a) length 20 Å per side, hence a volume of  $8 \times 10^3 \text{Å}^3$ , or (b) 100 Å per side, hence a volume of  $1 \times 10^6 \text{Å}^3$ , or (c) 500 Å per side, hence a volume of  $1.25 \times 10^8 \text{Å}^3$ . However, *unless explicitly indicated*, the results presented in Sections 4, 5 and 5 are for simulations that are 500 ns long in a simulation volume of  $1.25 \times 10^8 \text{Å}^3$  (or 500 Å per side). Temperature control was achieved by means of the Nosé-Hoover thermostat [133, 134] with a damping constant a damping constant of 0.01 ps, for temperatures between 2500 K and 6000 K. These simulations were conducted using LAMMPS [135].

Simulations of the interaction of carbon with the nickel nanocluster in Chapter 6 were were calculated using a timestep of  $\Delta t = 1$  fs and a total simulation run of 10 ns (excluding an initial equilibration time of 50 ps). As before, temperature control was achieved via the Nosé-Hoover thermostat. These simulations were conducted using GULP [136].

## 2.6 CHAPTER SUMMARY

In this chapter, we have introduced and discussed the foundations of molecular dynamics. We have also introduced two potentials that model the the covalent carbon-carbon bonding: the bond-order Tersoff potential [53] and the Topologically-constrained forcefield [1].

The Tersoff potential, in comparison to TCF, can be considered as a topologically-free forcefield. It is an empirical bond-order type potential, where the bond-order term accounts for the many-body effects in the system and depends upon the local atomic environment of the bond. By using this scheme, the bond order term allows for the making and breaking of bonds in the Tersoff potential.

The Topologically-constrained forcefield (TCF) was first developed to specifically explore the  $C_{60} \leftrightarrow 30C_2$  channel. This was done by restricting the number of neighbours such that each atom is constrained to only interact with specific neighbours within the system. Thus these constraints allow one to restrict the system to explore only certain areas of its available phase space, *i.e.* those that are relevant for the fullerene formation and fragmentation within the  $C_{60} \leftrightarrow 30C_2$  channel. By omitting these topological constraints and considering all possible carbon bonding formations in the system, the fullerene will be just one among a myriad of other possible carbon clusters. This would make the observation of the fullerene formation from a gas of 30  $C_2$  atoms an extremely unlikely event. Additionally, the computational demands to observe such an event would be extremely demanding as one would have to run numerous trajectories in order to observe a single fullerene formation event. Thus the topological constraint allows us to focus only on the fullerene formation channel without needing to account for all other possible structures.

Both of these potentials are used to run molecular dynamics simulations of various nanocarbon systems, whose results are presented in the following two chapters—Chapters 4 and 5.

We have also introduced the Sutton-Chen potential [121], used to describe the nickel-nickel interaction for the work in Chapter 6, where we discuss the effect of carbon on a nickel metalcluster.



## CHAPTER 3

# PRINCIPLES OF PHASE TRANSITION

In this chapter, we discuss the concepts of phase transition. In particular, we focus on phase transition of finite systems, of which clusters are an example, depend significantly on the size of the cluster. One such size-specific property is the melting temperature of metal clusters. In general, the melting temperature of a spherical metal particle is known to decrease monotonically with decreasing particle radius [137–141]. This relation is captured in the empirical “Pawlow law” [138] and is expressed as,

$$T_m = T_m^{bulk} \left(1 - \frac{\alpha}{r}\right), \quad (3.1)$$

where  $T_m$  is the melting temperature,  $r$  is the radius of the spherical particle and  $\alpha$  is a constant defined by fitting the temperature  $T_m$  to available experimental data. While equation 3.1 shows good correspondence for large clusters, such as nickel clusters consisting of 336–8007 atoms [141], this monotonic decrease of the melting temperature with size is only valid down to 2–3 nm [142–145].

Below this limit of 2 nm, the melting temperature is no longer a monotonic function of cluster size. This has been demonstrated for various types and sizes of clusters, in particular, sodium [9, 146–149], tin [6, 150], aluminium [151–153] and gallium [8, 154] clusters. The variation in the melting temperature with size shows an irregular trend, such that changing the cluster size by an additional atom may cause a substantial change in the melting

temperature. In fact, the melting temperatures of selected tin [6], gallium [8] and aluminium [152] clusters approach or even exceed that of the respective bulk counterpart. This counterintuitive result stems from the structural differences between the small clusters and the bulk [6].

In the following section, we briefly outline classification of phase transitions. We then discuss *static* and *dynamic phase coexistence*. The former is characteristic of bulk matter, while the latter of finite structures.

### 3.1 CLASSIFYING PHASE TRANSITIONS

Thermodynamically, an equilibrated stable phase of a system is associated with the lowest free energy of the appropriate ensemble (the Helmholtz free energy  $F$  for the canonical ensemble; the Gibbs free energy  $G$  for the isobaric-isothermal ensemble; the internal energy  $U$  for the microcanonical ensemble). However, a system may reside in a long-lived metastable phase if there is a sufficiently high energy barrier separating it from the equilibrated stable phase for given external parameters, *e.g.* pressure, temperature. An appropriate example would be the long-lived metastable phase of diamond at room temperature and atmospheric pressure, although graphite is the actual stable phase of carbon within these conditions. By heating diamond in an oxygen-free environment at 1400–1700 K, the energetic barrier can be overcome and diamond transforms into the stable phase of graphite. In other words, one can associate equilibrated stable phases to the global minimum of the free energy, while metastable states correspond to the local free energy minima.

A phase transition occurs when the system evolves from one phase to another. This can be seen in the free energy which either changes continuously or exhibits a non-analytic change. The non-analytic behaviour of the free energy indicates that the free energies of the phases on either side of the transition are two different functions. In 1933, Ehrenfest proposed a classification of phase transitions based on thermodynamic potentials [155]. In this scheme, a *first-order phase transition* occurs when the thermodynamic quantities corresponding to the first derivative of the free energy are discon-

tinuous,

$$C_p = \left( \frac{\partial A}{\partial T} \right)_p \quad S = - \left( \frac{\partial G}{\partial T} \right)_p \quad V = \left( \frac{\partial G}{\partial p} \right)_T, \quad (3.2)$$

where  $G$  is the Gibbs free energy,  $C_p$  is the constant-pressure specific heat capacity,  $T$  the temperature,  $S$  the entropy and  $V$  the volume. All first-order phase transitions involve a latent heat  $\Delta H$  due to the discontinuity in the entropy,  $\Delta H = T_c \Delta S$ , at a critical temperature  $T_c$ . Thus during such a transition, the system either absorbs or releases a fixed amount of energy without change in temperature.

In *second-order* phase transitions, the first derivative of the free energy is continuous, while the second derivative may either be discontinuous or divergent,

$$\begin{aligned} - \left( \frac{\partial^2 G}{\partial T^2} \right)_p &= \left( \frac{\partial S}{\partial T} \right)_p = \frac{C_p}{T} \\ - \left( \frac{\partial^2 G}{\partial p^2} \right)_T &= - \left( \frac{\partial V}{\partial p} \right)_T = \kappa_T \cdot V, \end{aligned} \quad (3.3)$$

where  $\kappa_T$  is the compressibility at constant temperature. In the Ehrenfest's original classification, the order of the phase transition corresponds to the lowest derivative of the free energy with a discontinuity. However, it is known that many phase transitions, such as ferromagnetic transitions in metals, can be characterised by a divergent behaviour instead. For this reason, the original classification has been extended to encompass a general non-analyticity of the free energy derivative. Additionally, second-order phase transitions—and in fact, all higher-order phase transitions—do not involve latent heat.

In 1937, Landau formulated a phenomenological theory of phase transitions based on the concept of order parameters and symmetry. In a phase transition without an associated latent heat, the order parameter—which is any extensive physical quantity that can distinguish between two phases—is zero in the most symmetric (or most disordered) phase and non-zero in the least symmetric (or ordered) phase. Therefore, the phase transition causes symmetry breaking. In a magnetic material, the order parameter is

the net magnetisation. When the temperature increases beyond a critical point (the Curie temperature), a second-order phase transition occurs and the material becomes paramagnetic, *i.e.* no net magnetisation in the absence of an external field. However, below the Curie temperature, there is spontaneous symmetry breaking and the material has a net magnetisation in a certain direction.

Ehrenfest's classification can be expanded to account for the notion of order parameter. In this scheme, two types of phase transitions can be distinguished:

- phase transitions where the order parameter is discontinuous at the phase transition temperature, and the two phases do not have a symmetry group-subgroup relationship to each other. These transitions always involve a latent heat and are equivalent to the Ehrenfest first-order phase transition
- phase transitions where the symmetry group of the least symmetric phase is a subgroup of the symmetry group of the most symmetric phase. If the order parameter is discontinuous at the phase transition, the transition is equivalent to the Ehrenfest first-order transition; if it is continuous, it is a second-order phase transition without a latent heat.

## 3.2 PHASE COEXISTENCE

In general, the main difference between the phase transition of finite systems and bulk matter lies in the significant contribution of the surface energy in finite systems. Moreover, the free energy difference between two phases is large in bulk matter and small in finite systems (this point will be elaborated further in the discussion regarding phase coexistence). Thus the classification of phase transitions introduced in the previous section can be adapted to describe finite-sized systems. Instead of a discontinuity in the heat capacity (or the caloric) curve at the phase transition temperature, the heat capacity curve for finite systems becomes “rounded-off” and exhibits a singular

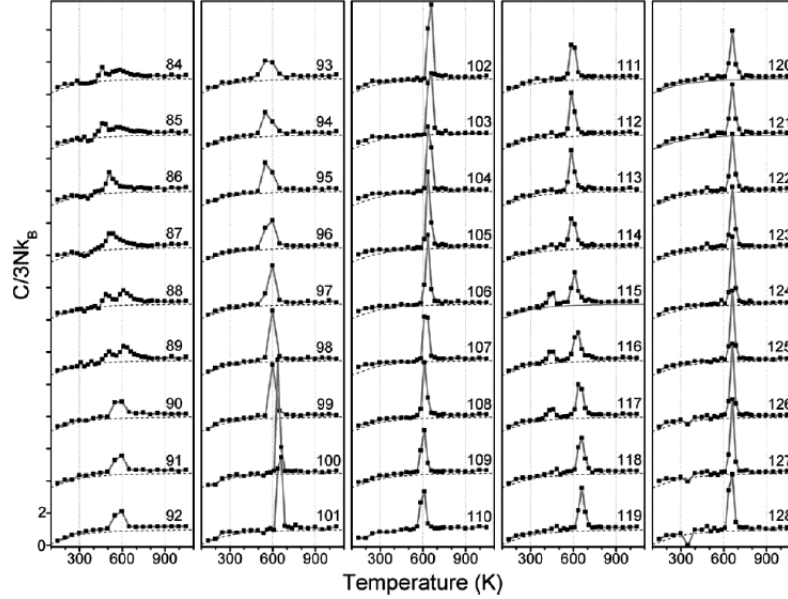


Figure 3.1: Finite-sized heat capacity curves of aluminium clusters consisting of 84-128 atoms [153].

significant peak, as demonstrated in Fig. 3.1 for small  $\text{Al}_n$  clusters, where  $n = 84 - 128$  atoms. This is a finite-sized analogue of a first-order phase transition. In addition to this, there are differences in the thermodynamic properties of the finite system in different statistical ensembles (while in the bulk, these properties are the same). As an example, while the phase transition temperature is identical, the width of the transition region in the caloric curves of the finite system in the microcanonical and the canonical ensembles are different. This can be rationalised in terms of the energy fluctuations within the canonical case [5].

At the phase transition temperature, a system may exhibit phase coexistence between two or more phases. In bulk matter, this phase coexistence takes place through the existence of domains containing either phase, separated by an interface. This can be seen in the boiling of water, in which water does not transform instantly to vapour. Rather, a turbulent mixture of water and water vapour bubbles can be seen prior to a complete transition. In this example, the two phases are water and vapour and the interface be-

tween the two is the surface of the water vapour bubble. A phase coexistence characterised by *simultaneous* coexisting phases through the existence of an interface is known as *static phase coexistence* or phase separation.

Finite systems may demonstrate phase separation [156], however they may also exhibit *dynamic phase coexistence*. This occurs in finite systems through sudden transitions between configurationally different states. For a cluster at its melting temperature, dynamic phase coexistence can be manifested through oscillations of the cluster between the frozen and molten phases, where it spends relatively long intervals in one phase before transitioning to the next phase. Therefore, instead of simultaneous phase separation through an interface, the cluster transforms from being completely in one configuration to another. This can only occur (in the canonical ensemble) if the difference of the free energies between the two phases is within the energy fluctuations of the system, proportional to  $kT$ , where  $k$  is the Boltzmann constant and  $T$  the phase transition temperature. Dynamic phase coexistence is also thought to occur due to the energetic cost of creating an interface between the two phases, due to the high surface area to volume ratio of finite systems. Hence, a signature of dynamic phase coexistence is the oscillations of the short time-averaged total energy of the system about two average values corresponding to two phases, see Fig. 6.3, *i.e.* a bimodal internal energy distribution for two coexisting phases, though in general a system may exhibit multiple phase coexistence at the phase transition temperature.

The existence of dynamic phase coexistence was largely demonstrated via molecular dynamics simulations in small clusters of Argon and various metal clusters, including sodium, nickel and aluminium. Experimental supporting evidence for the presence of dynamic phase coexistence in  $\text{Na}_{147}$ ,  $\text{Al}_{100}$  and  $\text{Al}_{101}$  clusters have been performed to show the presence of a bimodal internal energy distribution at the phase transition temperature. Note that, in order to demonstrate dynamic phase coexistence, the time between, *e.g.* the melting and freezing transitions must be longer than the time required for equilibration of the internal energy of the finite system.

### 3.3 CHAPTER SUMMARY

In this chapter, we have introduced phase transition in finite systems. The main difference between the phase behaviour of finite systems and bulk matter can be attributed to the large surface energy in finite systems, as well as the small difference in the difference of the free energies between two phases (as compared to the bulk). As a result, finite systems may exhibit *dynamic* phase coexistence, where two different phases coexist at different times. Effectively, at the phase transition temperature, the finite system is completely found in one phase for some period and in another phase at a different period. This is in contrast to *static* phase coexistence, or phase separation, characteristic of bulk systems.





## CHAPTER 4

# C<sub>60</sub>: BUCKMINSTERFULLERENE

Having finished the discussion on the theoretical aspects of phase transition, we now turn our attention to the application of these ideas to fullerenes, hollow carbon cages formed of five- and six-fold carbon rings. Although discovered more than twenty years ago, these hollow cages continue to remain one of the most investigated molecules in the field of nanoscience, superseded only by their close relative: carbon nanotubes. Both structures however, are driven by a common question regarding their origins: how are they formed? How do they grow? What drives their formation processes? In fullerenes, these questions are at the heart of the puzzle of C<sub>60</sub>—a fullerene whose particular abundance is often a magnitude higher than any other size of fullerenes.

In this chapter, we first discuss how the length of a simulation affects the phase transition properties of C<sub>60</sub>. We then investigate the effect of the phase transition of C<sub>60</sub> on the simulation volume. We highlight the different behaviours of C<sub>60</sub> when it is a topologically-free and topologically-constrained system. In the case of the topologically-free C<sub>60</sub>, the system exhibits a variety of phases, including a long-lived metastable phase of graphene. In the topologically-constrained case, the C<sub>60</sub> can be found to continuously fragment and reassemble back into the fullerene cage at the phase transition temperature. Based on this result, we then present a statistical mechanics model that was developed to extend the simulation results to generalised pressure and temperature conditions in arc-discharge experiments [1].

## 4.1 FINITE TIME SIMULATIONS

The foundation of molecular dynamics is the ergodic hypothesis which assumes that the time-averages of a system is equivalent to the statistical ensemble averages. This assumption is valid, in general, when the dynamical trajectory of the system approaches infinite time. For finite time simulations however, it is important that the system's trajectory has sufficiently explored its phase space, such that the time averages of the observables can be correctly equated to the ensemble averages. In this section, we investigate how the length of the simulation—the total simulation time—affects the phase transition properties of  $C_{60}$  under constant-temperature molecular dynamics simulations.

It is well known that the  $C_{60}$  phase transition temperature obtained via molecular dynamics is significantly higher ( $>3000$  K) than those obtained in experiments ( $<2000$  K). This is because the relevant experimental timescales of fullerene fragmentation and formation are on the order of microseconds [40–42]. On the other hand, most molecular dynamics calculations of  $C_{60}$  fragmentation or formation are less than 50 nanoseconds long [31, 45–52, 56–59, 61–64, 157], which may lead to an overestimation of the phase transition temperature.

For this reason, some short computational works done with the Tersoff potential [57, 58, 111] have required recalibration of the obtained temperatures. This recalibration involves factoring the molecular dynamics temperature by a constant—determined by the ratio of the known experimental melting temperature of graphite (4300 K) to its computational value obtained from the short simulation. Nonetheless, such a recalibration remains arbitrary and does not clarify the effect of the simulation time on the equilibrium observables of the system. Instead of recalibrating the temperatures, we have conducted simulations of varying lengths in order to establish a sufficient simulation time that would generate accurate time-averages of the phase transition observables in the  $C_{60}$  system.

In Fig. 4.1, we present three caloric curves of  $C_{60}$  and their corresponding heat capacities for three different lengths of simulation time (50 ns, 500 ns

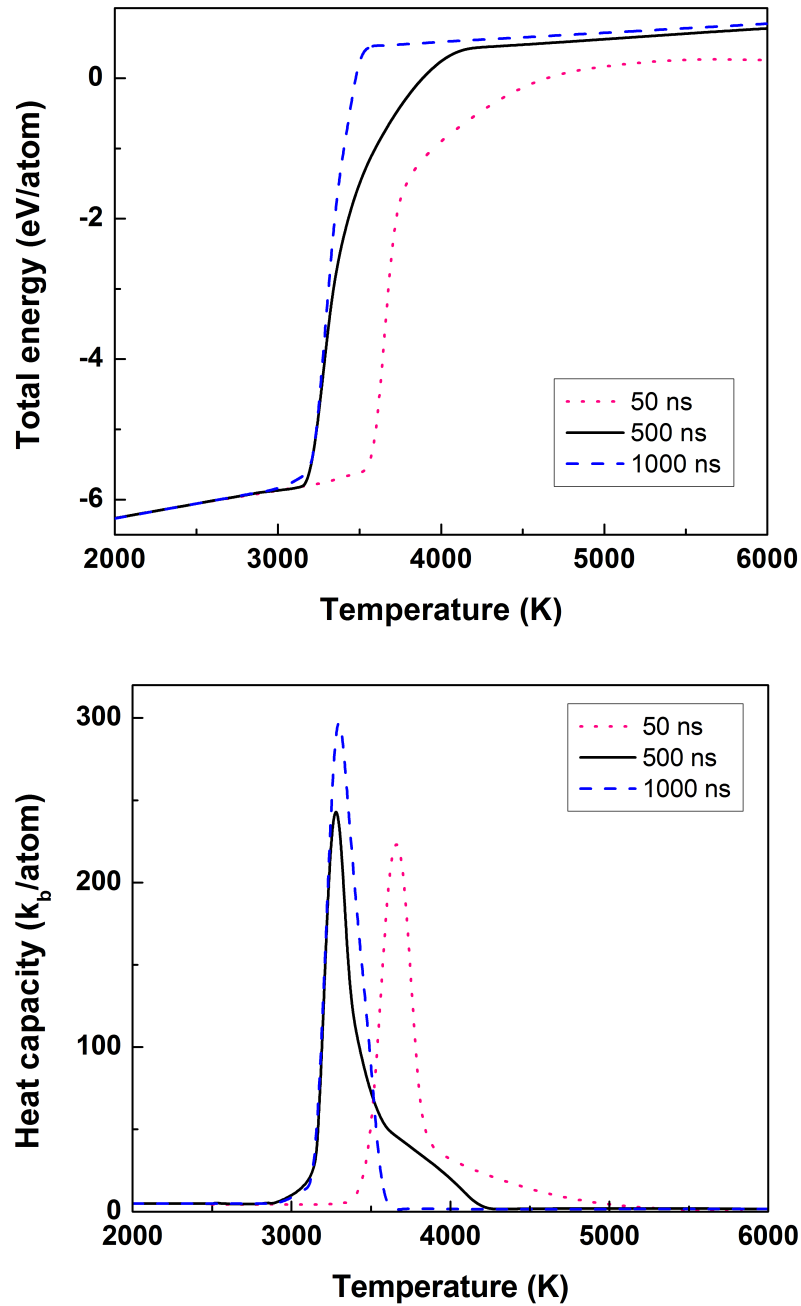


Figure 4.1: The caloric curves (top) and heat capacities (bottom) of  $C_{60}$ , as calculated using the Tersoff potential for three different simulation times (50 ns, 500 ns and 1000 ns). The figures demonstrate how the phase transition temperature is affected by the total simulation time. Note that the simulation volume is  $1.25 \times 10^8 \text{ \AA}^3$ .

and 1000 ns), as calculated using the Tersoff potential. All simulations were conducted in a constant volume of  $1.25 \times 10^8 \text{ \AA}^3$ , for temperatures between 2000–6000 K. Each heat capacity  $c_v$  is derived from its respective caloric curve by differentiating the total energy with respect to temperature,  $c_v = \frac{dE}{dT}$ . The significant peaks of the heat capacity plots indicate the finite-system analogue of a first-order phase transition. The temperature value of each peak in the heat capacity gives the *phase transition temperature*  $T_c$  of the system.

It is clear from Fig. 4.1 that the total simulation time affects the phase transition properties of  $C_{60}$ . For a 50 ns run, the phase transition temperature  $T_c$  is found to be 3660 K. However, when the simulation is ran ten times longer to 500 ns,  $T_c$  drops to 3285 K—a difference of more than 300 K. Thus, it can be concluded that a simulation of 50 ns is too short to give a stable phase transition temperature. In contrast, when the total simulation time is increased from 500 ns to 1000 ns, the phase transition temperature changes by a mere 5 K to 3290 K. Hence, we can consider the phase transition temperature to have converged at  $T_c = 3290$  K and that a simulation of 500 ns is sufficient to provide the correct time-averaged phase transition temperature.

Nevertheless, from Fig. 4.1, the trajectory-averaged caloric curve of the 500 ns simulation (solid black) does not have the sharp energy increase that is seen in the simulation of 1000 ns (dashed blue). In fact, the 500 ns simulation retains some of the statistical artifacts seen in the simulation of 50 ns (dotted red). This is more clearly seen in the heat capacity plot of Fig. 4.1, where both the 50 ns and 500 ns curves show an asymmetrical shoulder which is absent in the 1000 ns curve. Additionally, the sharpness of the 1000 ns caloric curve contributes to a higher and narrower heat capacity plot, when compared to the two remaining curves. Therefore, while the 500 ns simulation may accurately average the important phase transition temperature, the averages between 3290–4200 K is more qualitative. This is due to the fact that the  $C_{60}$  fragments at a timescale of about 500 ns at these temperatures. However, between 4200–6000 K, the  $C_{60}$  fragments before 500 ns. Thus, the heat capacity plots of the 500 ns and the 1000 ns simulations overlap in these temperatures. We can therefore consider the trajectory of the 500 ns sim-

ulation to have sufficiently (although not densely) sampled the phase space of the system. Hence, for the remaining of the work, all of the presented simulations were conducted for 500 ns unless indicated otherwise.

## 4.2 TOPOLOGY AND VOLUME EFFECTS

A topologically-free system is one that is free to generate all possible microstates determined by its statistical ensemble. Specifically, for a system of 60 carbon atoms in a constant volume  $V$  and at temperature  $T$ , the initial state of the system is free to evolve into any possible topological form, e.g. from a  $C_{60}$  fullerene to a nanotube structure, or to a gaseous state of 60 carbon atoms. The probability of the transition from the initial state to a myriad of possible final states will then depend on the statistical weighting of each initial state  $\leftrightarrow$  final state channel.

On the contrary, a topologically-constrained system is forced to explore only certain microstates in its statistical ensemble. Therefore the initial state of the system is steered to only evolve within specific channels, which have high statistical weightings, and restrained from evolving into other channels, which have very low statistical weightings. Hence, a topologically-constrained  $C_{60}$  may be much more likely to evolve into, e.g. a gas of 30 carbon dimers compared a graphene sheet of 60 carbon atoms. The difference in the weighting of the channels between the topologically-constrained and the topologically-free system will then depend on the potential used to describe the intramolecular interactions of the  $C_{60}$ .

In this work, the Tersoff potential is used to model a topologically-free  $C_{60}$ , while the Topologically-constrained forcefield is used to model the restricted  $C_{60}$ . In the following two subsections, we examine the dynamics and phase transition properties of both types of systems within two different simulation volumes: a large simulation box of side length 500 Å (giving a volume of  $1.25 \times 10^8 \text{Å}^3$ ) and a small simulation box of side length 20 Å (giving a volume of  $8 \times 10^3 \text{Å}^3$ ).

### 4.2.1 THE TOPOLOGICALLY-FREE $C_{60}$

We first investigate the topologically-free  $C_{60}$  using the Tersoff potential. In Fig. 4.2, we present the caloric curves and heat capacities of the system within the large simulation volume of  $1.25 \times 10^8 \text{Å}^3$  (solid black line) and the small simulation volume of  $8 \times 10^3 \text{Å}^3$  (dashed red line).

In the large simulation volume (solid black line), the caloric curve of  $C_{60}$  exhibits a sharp “S”-shape behaviour which is absent in the caloric curve of the small volume (dashed red line)—see inset (a) of Fig. 4.2 for a magnification of the respective caloric curve. Moreover, the caloric curve of the small volume (dashed red line) contains an almost “plateau”-like slope between 3600–4300 K, which is then followed by a rapidly increasing slope. As a result, the corresponding heat capacity curves in the two volumes are distinct. For the large  $1.25 \times 10^8 \text{Å}^3$  volume, the heat capacity shows a significant peak indicating the finite system analogue of a first-order phase transition. Contrastingly, the heat capacity of  $C_{60}$  calculated in the the small  $8 \times 10^3 \text{Å}^3$  volume shows an “S”-shaped curve, shown in Fig. 4.2(b). Differentiating this curve leads to a single pronounced peak, indicating a second-order-like phase transition of  $C_{60}$ , as can be seen in Fig. 4.2(c).

Let us first analyse the simulation results within the large  $1.25 \times 10^8 \text{Å}^3$  volume. Fig. 4.3 shows the time-dependent total energy per atom of the  $C_{60}$  (energy profile) at the phase transition temperature, indicated by the temperature of the peak in the heat capacity curve. The inset of Fig. 4.3 shows the energy profile of the complete trajectory of the system (1000 ns), while the main graph shows a magnification of the profile for simulation times 0–500 ns. Similar to the shape of the caloric curves presented in Figs. 4.1 and 4.2, the energy profile in the inset shows a sharp jump in the total energy, occuring around 500 ns. This energy jump signifies the occurrence of a phase transition in the system. While the energy fluctuations in the system after the phase transition is about a constant value, the energy fluctuatations occuring before the onset of phase transition is more complex.

In the main plot of Fig. 4.3, “steps” in the energy profile can be observed. These steps indicate that the system may be evolving through a

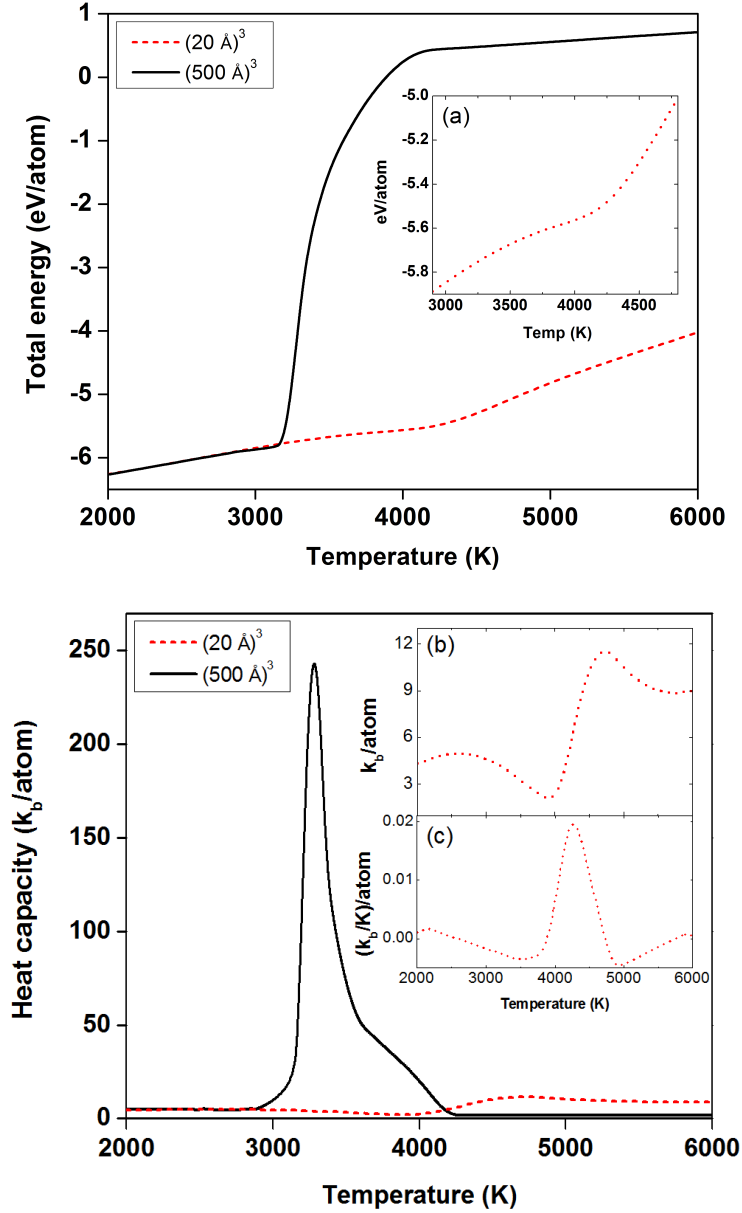


Figure 4.2: Caloric curves (top) and heat capacities (bottom) of  $C_{60}$ , as calculated using the Tersoff potential for volumes  $8 \times 10^3 \text{ \AA}^3$  (dashed red) and  $1.25 \times 10^8 \text{ \AA}^3$  (solid black). *Insets:* (a) and (b) are, respectively, magnifications of the caloric curve and heat capacity of  $C_{60}$  in a simulation volume of  $8 \times 10^3 \text{ \AA}^3$ ; (b) shows that the heat capacity has double extrema whose derivative, shown in (c), has a significant peak indicating a second-order-like phase transition. Note that the simulation time is 500 ns.

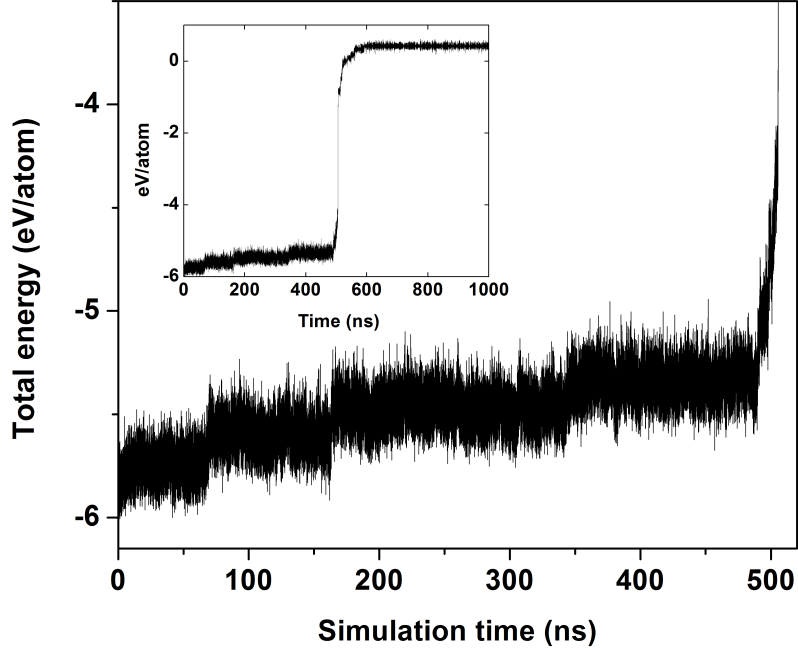


Figure 4.3: Total energy as a function of simulation time at the phase transition temperature of  $C_{60}$  as calculated with the Tersoff potential. The *inset* shows the behaviour of the total energy for the complete 1000 ns long simulation, while the main plot shows magnification of the inset between 0-500 ns, highlighting the steps in the total energy before fullerene fragmentation (see text for a discussion regarding the energy steps). Note that the simulation volume is  $1.25 \times 10^8 \text{ \AA}^3$ .

series of distinct topological states whose average energy can be given by the average value of the energy fluctuations in each distinct “step”. Thus, the phase transition in this system does simply occur from the intact  $C_{60}$  cage to some final state. Rather, prior to the phase transition, the system may have evolved into a different state such that the immediate structure just before the phase transition around 500 ns is no longer a fullerene. On the other hand, the energy fluctuations after the phase transition indicate that the final state of the system can be found as a constant topological state. The fact that these fluctuations occur about a value slightly above 0 eV signifies that the final state of the system is one where there is minimal interatomic interaction between the carbon atoms, hence, a gas of 60 noninteracting C



atoms.

To further analyse the pre-phase transition behaviour of  $C_{60}$ , we present in Fig. 4.4, snapshots of the trajectory at the phase transition temperature. The trajectory evolves as follows: the intact fullerene cage experiences a series of bond transformations, where the bonds in the cage breaks, flips and re-forms. As a result, the pentagons in the cage begin migrating about the  $sp^2$  network and the fullerene cage exhibits “sticks” and “handles” which are dangling bonds and dangling rings respectively. These “sticks” and “handles” are either re-incorporated back into the cage structure or they may be evaporated from the cage as C or  $C_2$ .

The bond transformations and carbon evaporation causes the cage structure to open and to form either a bowl-shaped or a tube-shaped structure, Fig. 4.4(b) and (c) respectively. The continuing deformation of the cage then leads to the the opening of the curved carbon network as all the pentagons are removed from the structure through the bond transformation process. Without a pentagon in the carbon network, there is a lack of curvature and the network of hexagons from a graphene sheet. Within the course of the simulations in the large  $1.25 \times 10^8 \text{Å}^3$  volume, we have only observed the occurrence of this graphene phase after the evaporation of at least 2 carbon atoms from the initial cage structure. Further evaporation of C or  $C_2$  from this graphene structure leads to a highly unstable mass of joined carbon chains and large rings which then fragments into smaller rings and chains before total fragmentation to a gas of C and  $C_2$ .

We turn our attention to the phase transition of  $C_{60}$  when it is confined in the small simulation volume of  $8 \times 10^3 \text{Å}^3$ . The relevant caloric curve and heat capacity plots are the red dashed lines in Figs. 4.2.

To further understand the structural transitions occurring in the  $C_{60}$  when simulated within this small volume, we have plotted in Fig. 4.5 the energy profiles corresponding to the three distinct regions in the caloric curve of Fig. 4.2: (a) the region in the caloric curve before 3600 K, (b) the region between 3600–4300 K and (c) the region after 4300 K. In Fig. 4.5(a), the system remains in a fullerene cage structure. However, when the temperature is increased and the system enters the “plateau” in the caloric curve,

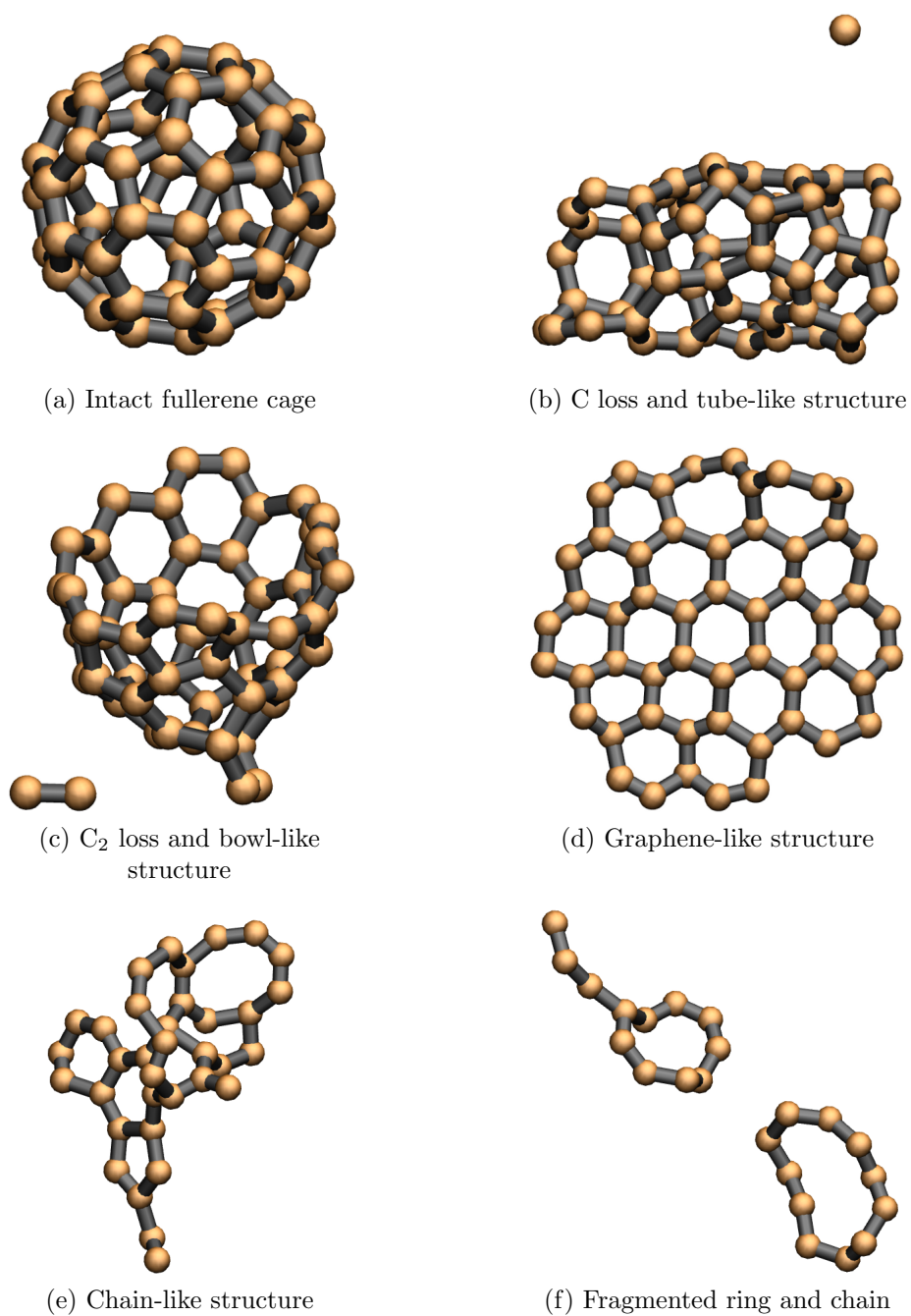


Figure 4.4: Snapshots of the  $C_{60}$  fragmentation process at the phase transition temperature (as calculated using the Tersoff potential). The snapshots (a)–(e) occur between 0–500 ns, prior to the total energy jump shown in Fig. 4.3. Note that the simulation volume is  $1.25 \times 10^8 \text{ \AA}^3$ .

Fig. 4.5(b) shows that while there is not much of an energy increase from the previous phase, the fullerene cage has unravelled into a graphene sheet. The system remains in this structure from 3600 K to 4300 K after which it disintegrates into disordered chains, as shown in Fig. 4.5(c).

As demonstrated in the previous subsection, fragmentation of  $C_{60}$  under the Tersoff potential is preceded by a transformation of the cage to a graphene-like structure. When the system is confined to a small volume, this graphene phase becomes a long-lived metastable state between temperatures 3600-4300 K. In the bigger volume of  $1.25 \times 10^8 \text{Å}^3$ ,  $C_{60}$  has already fragmented by 3300 K to a gaseous phase of carbon atoms and  $C_2$  dimers. However, in this small volume of  $8 \times 10^3 \text{Å}^3$ , the fullerene cage does not reach this gaseous phase even at 6000 K, as can be seen in Fig. 4.2(a) where the total energy per atom of the system remains well below 0 eV. Additionally in Fig. 4.5(c), one can observe that the system enters the interlinked-chain phase seen in the bigger  $1.25 \times 10^8 \text{Å}^3$  volume immediately prior to rapid fragmentation.

#### 4.2.2 VALIDATION OF THE TOPOLOGICALLY-CONSTRAINED FORCEFIELD

Before we discuss the results of  $C_{60}$  using the Topologically-constrained forcefield, we present a discussion of the accuracy of this novel forcefield. We first compare the Topologically-constrained forcefield to the Tersoff potential via the single-point energies of a small set of carbon clusters. Next, we compare the Topologically-constrained forcefield with the more advanced tight-binding method. The latter comparison is conducted through TCF simulations of the fragmentation distribution of  $C_{60}$  under constant-energy, as was done by Ref. [61] using the tight-binding technique.

In Table 4.2.2 we compare the energies of small carbon structures ( $C_2$ - $C_6$ ) as well as  $C_{60}$  calculated using TCF [1] and the Tersoff potential [53, 54]. As shown, the energies of structures calculated with TCF is in a reasonable agreement with those calculated using the Tersoff potential. The accuracy of TCF can be evaluated as being on the order of 5% for all species except

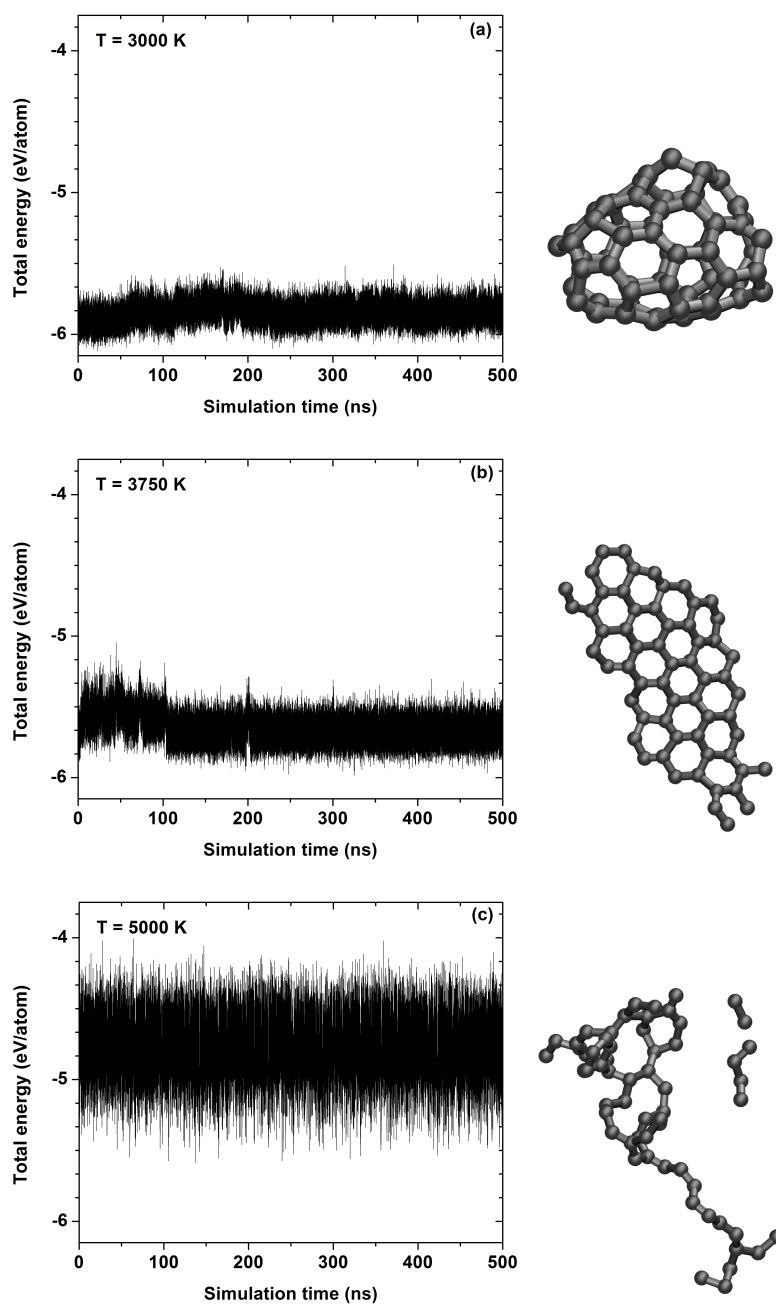


Figure 4.5: The energy profiles (left) and evolved structures (right) of  $C_{60}$ , as calculated using the Tersoff potential, for temperatures of (a) 3000 K, (b) 3750 K and (c) 5000 K. Note that the simulation volume is  $8 \times 10^3 \text{\AA}^3$ .

Species	Tersoff (eV)	Forcefield (eV)	Accuracy
C <sub>2</sub>	-5.165	-6.266(d)	19.2%
C <sub>3</sub>	-10.329	-10.082(s+d)	2.4%
C <sub>4</sub>	-15.493	-16.348 (2d+s)	5.3%
C <sub>5</sub>	-21.514	-20.164(2d+2s)	6.4%
C <sub>6</sub>	-30.121	-30.246(3d+3s)	0.4%
C <sub>60</sub>	-403.687	-416.5245 (30d+60s)	5.9%

Table 4.1: Comparison of the energies of the structures calculated with the topologically-constrained forcefield (TCF) and the Tersoff potential. TCF has two C-C energy parameters which we refer to as the single (s) bond and the double (d) bond. In the table below, we present the energies of the structures of the most stable linear (C<sub>2</sub> to C<sub>5</sub>) and planar (C<sub>6</sub>) isomers of small carbon clusters. The energies calculated within TCF are constrained by the fact that each carbon atom can have only one double bond.

the carbon dimer. However, the difference in the bond energies of the C<sub>2</sub> as calculated by TCF and the Tersoff potential has a minor influence on the results of the molecular dynamics simulations of the fullerene phase transition. This is because our primary motivation is to simulate only the C<sub>60</sub> ↔ 30C<sub>2</sub> channel. The accuracy in the energy of C<sub>2</sub> will only become important in the course of the simulations when there is a significant fragmentation of C<sub>2</sub> → 2C. However, the presence of single carbon atoms are observed only in small quantities at the temperatures of the phase transition (see the discussion in Section).

In Fig. 4.6, we present the fragmentation distribution of C<sub>60</sub> from the tight-binding simulations of Ref. [61] (in *blue*) and the distribution calculated using TCF (in *red*). The TCF simulations were conducted in a volume of 8·10<sup>9</sup> Å<sup>3</sup> for 1 ps. It is seen from our results that between 130–200 eV, there is an onset of a transition to the formation of small clusters ( $N < 30$ ). While at 300 eV, only fragments of sizes below 15 are obtained. It is worthwhile to point out that a significant proportion of small clusters in our distribution is in the form of C<sub>2</sub>. This is because the topologically-constrained forcefield was

developed to adequately describe the initial and final states of the system, in this case: the fullerene cage and the gas of  $C_2$  units.

The exact path in the phase space between  $C_2$  gas and  $C_{60}$  is not of primary importance since only these two states form at the statistical equilibrium, *i.e.* the most prominent minima on the free energy potential surface of the system. As a result, the distribution obtained using TCF will similarly show a prominent weighting for fragments of  $C_2$  and  $C_{60}$ , whereas the intermediate states are not fully represented. These factor thereby contribute to the resulting bimodal fragmentation distribution observed in our results, in contrast to the U-shape distribution obtained in [61] between 130–200 eV.

The comparison between TCF and the results of Ref. [61] is instructive in demonstrating the accuracy of TCF when compared to a more sophisticated potential. The deviation in the behaviour of the TCF and the tight-binding distribution between 130–200 eV is affected not only by the ability of each potential to describe the intermediate states, but also by the time of the simulations. Nevertheless, at high and low energies, there is a reasonable correspondence between the result obtained within the TCF and the tight-binding approach of [61].

### 4.2.3 THE TOPOLOGICALLY-CONSTRAINED $C_{60}$

We have previously shown that the dynamical trajectory of a topologically-free  $C_{60}$  spans many different topological states and that, depending on the simulation volume, may exhibit either a first-order or a second-order-like phase transition. We now investigate the dynamics and phase transition properties of the constrained  $C_{60}$  using the Topologically-constrained force-field.

The Topologically-constrained forcefield prevents the system from being trapped in a myriad of possible states during its trajectory. This is done through two methods: static neighbouring and a higher statistical weight to the  $C_{60}$  and  $C_2$  structures. The static neighbouring effectively prevents bond-flipping and the interchange of bonds. Instead, each atom has been assigned a fixed number of neighbours with whom it can form “covalent”-

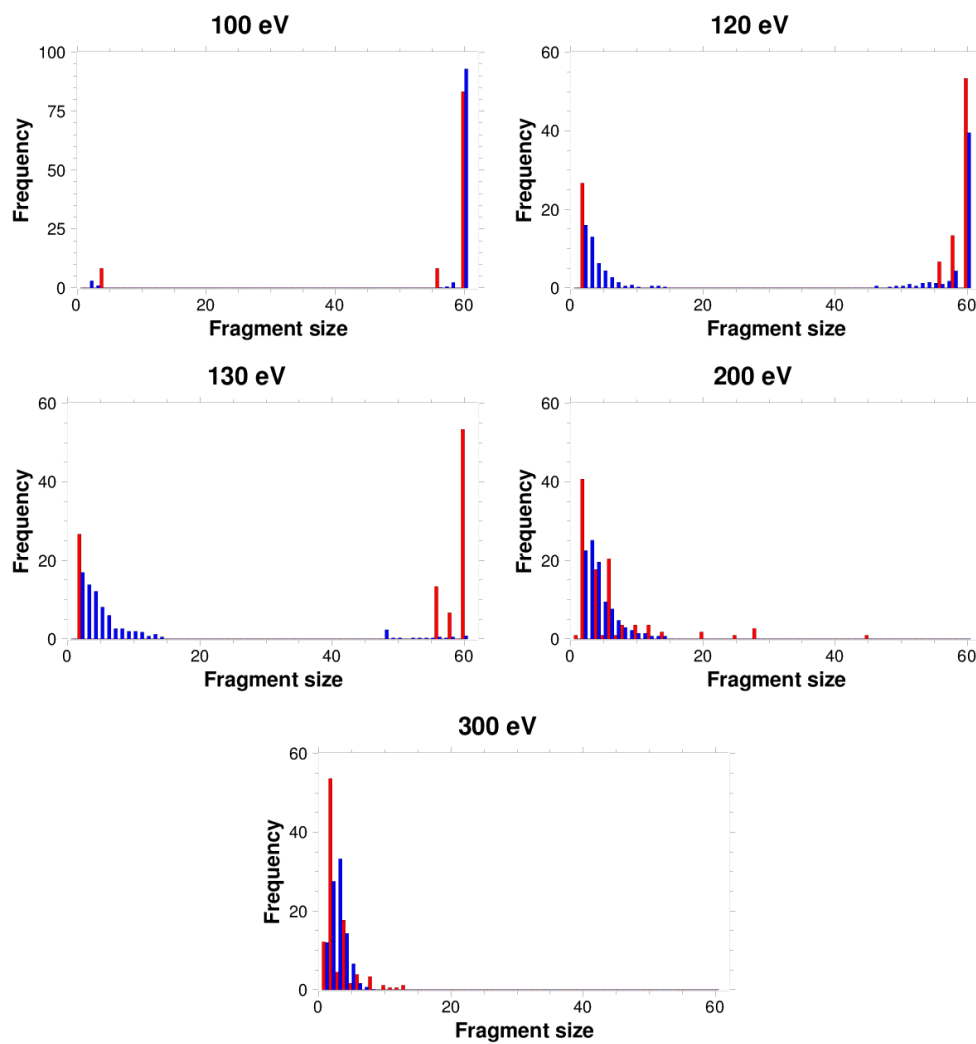


Figure 4.6: (colour online) Averaged number of fragments for selected excitation energies (100, 120, 130, 200 and 300 eV). In *red*: results obtained using TCF show a heavier weighting for  $C_2$  and  $C_{60}$  fragments. In *blue*: results of Ref. [61] using a tight-binding approach.

type bonding. The number of “covalent” neighbours assigned to each atom is 3, thus preventing the formation of any  $sp^3$  tetravalent structures such as nanodiamonds. In this way, the topologically-constrained system is steered to evolve within a specific number of channels.

We present in Fig. 4.7, the caloric curves and heat capacities as calculated using the *Topologically-constrained forcefield* for simulation volumes  $1.25 \times 10^8 \text{Å}^3$  (solid black line) and  $8 \times 10^3 \text{Å}^3$  (dashed red line). The caloric curve and heat capacity in the large  $1.25 \times 10^8 \text{Å}^3$  volume show a similar shape to the caloric curve of the topologically-free case (see Fig. 4.2). However, the caloric curve of the constrained  $C_{60}$  in the small  $8 \times 10^3 \text{Å}^3$  volume is very different from the topologically-free system. This is clear from the heat capacity plots in Fig. 4.7 which shows that the constrained  $C_{60}$  experiences only a first-order-like phase transition in either simulation volume.

Furthermore, the caloric curves of  $C_{60}$  in the small volume is different from that of the large volume only in the amplitude of the energy jump—which is shown correspondingly in heights of the respective heat capacity plots. This indicates that the final state of the system in the two volumes are different. Additionally, the phase transition temperatures obtained for the topologically-constrained  $C_{60}$  is much higher than the topologically-free case, although the phase temperature difference between the volumes is similar in both systems. This may signify that the topologically-constrained system is evolving within a high-temperature channel which is less accessible than the channels used by the topologically-free system.

We first consider the topologically-constrained  $C_{60}$  within the large  $1.25 \times 10^8 \text{Å}^3$  volume. In Fig. 4.8, we present the time-dependent total energy profile of the  $C_{60}$  at the phase transition temperature. The sharp “S”-shaped curve of the energy profile is similar to the case of the topologically-free  $C_{60}$ . However, the energy profile of the topologically-constrained system is absent of the energy “steps” seen in the free case. Rather, the total energy fluctuates about a constant value before and after the occurrence of a phase transition in the system, around 200 ns. This indicates that the trajectory only involves two topologically distinct states: one before the phase transition and one after—hence a two-state system. Thus, by constraining the system to



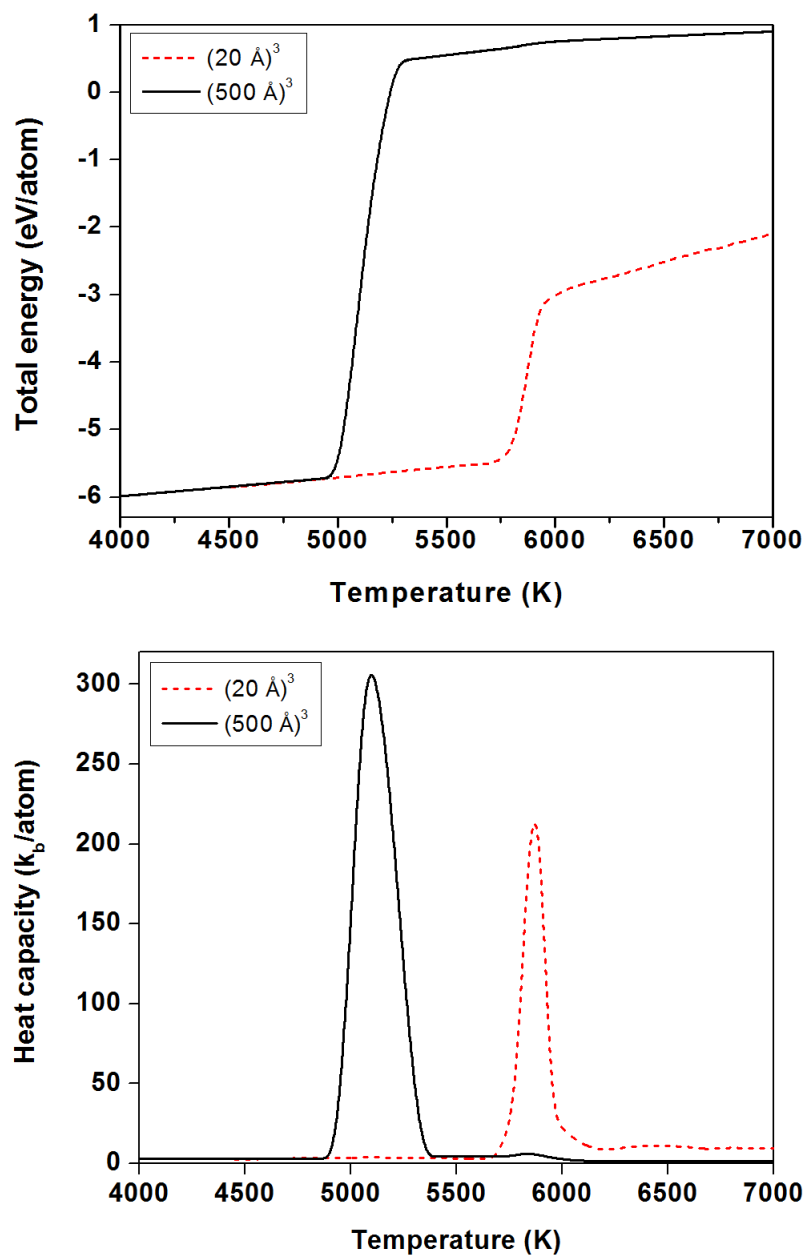


Figure 4.7: Caloric curves (top) and heat capacities (bottom) of  $C_{60}$ , as calculated using the Topologically-constrained forcefield for volumes  $8 \times 10^3 \text{ \AA}^3$  (dashed red) and  $1.25 \times 10^8 \text{ \AA}^3$  (solid black). Note that the simulation time is 500 ns.

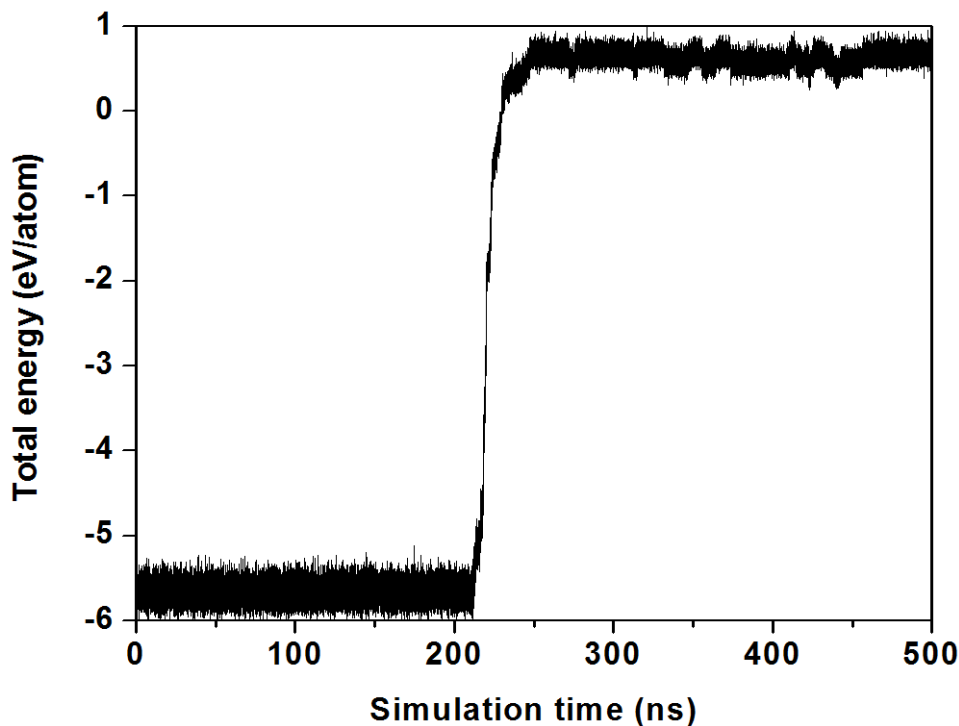


Figure 4.8: Total energy as a function of simulation time at a temperature of 5125 K—the phase transition temperature in  $C_{60}$  as calculated with the Topologically-constrained forcefield. Note that the simulation volume is  $1.25 \times 10^8 \text{ \AA}^3$  and the total simulation time is 500 ns.

explore only the  $C_{60} \leftrightarrow 30C_2$  channel, the system has been steered away from falling into intermediate states, such as the graphene phase shown in Fig. 4.5(b).

Indeed, in analysing the evolution of the constrained  $C_{60}$ , we have found no distinct short-lived metastable structures prior to the phase transition of the  $C_{60}$ . This can be seen in Fig. 4.9, where we have presented snapshots of  $C_{60}$  trajectory at the phase transition temperature. As shown, the system begins in an initial state of the intact fullerene cage. As the cage deforms from its spherical shape, bond breakage occurs within the  $sp^2$  network, leading to the formation of “sticks”, Fig. 4.9(b), which are dangling bonds. These “sticks” are often evaporated away in the form of  $C_2$  molecules as seen in Fig. 4.9(b), and in some cases, C atoms. Further evaporation leads to an

“unravelling” of the cage into a short-lived structure of dangling chains and rings, Figs. 4.9(c-d), which then completely disintegrate into a gaseous phase of carbon atoms, Fig. 4.9(e).

While the behaviour of both the topologically-constrained and topologically-free  $C_{60}$  in the large  $1.25 \times 10^8 \text{Å}^3$  volume has many qualitative similarities, the constrained  $C_{60}$  within the small volume is very different from its free counterpart, and also, distinct from the constrained case within the large volume. This is clearly seen in Fig. 4.10, the time-dependent total energy profile of the constrained  $C_{60}$  at its phase transition temperature, within the small  $8 \times 10^3 \text{Å}^3$  volume. Fig. 4.10 shows that the total energy continuously oscillates throughout the entire 500 ns simulation. In fact, the system repeatedly jumps from one state to another, beginning from the initial state of the fullerene cage, to the final state of the system. This final state is determined to be an interactive gas of carbon dimers and short chains/rings, with an average total energy of  $-3.8 \text{ eV/atom}$ . In comparison, note that the final state within the large  $1.25 \times 10^8 \text{Å}^3$  volume is a gas of noninteracting C atoms.

Furthermore, the successive oscillations in the total energy indicates that the system is experiencing a coexistence of phases as it jumps from one phase (the fullerene cage) to another phase (a gaseous phase of carbon chains/rings and dimers). In other words, such oscillations correspond to cycles of consecutive fragmentation and reassembly of the fullerene cage. In fact, this can be seen in Fig. 4.11, where a fullerene cage is seen to reassemble from short chains which were previously formed from the interaction between carbon dimers.

The presence of phase coexistence in the system signifies that the difference between the free energies of the two distinct phases (the fullerene cage and the gas of carbon dimers) is on the order of  $kT$  per atom at the phase transition temperature. Thus, by confining the system to a small volume, the energy fluctuations at the phase transition temperature is enough for the system to overcome the energy barrier between the two phases, hence leading to consecutive oscillations between the cage and the gas states. To the best of our knowledge, this work is the first where the processes of fragmentation

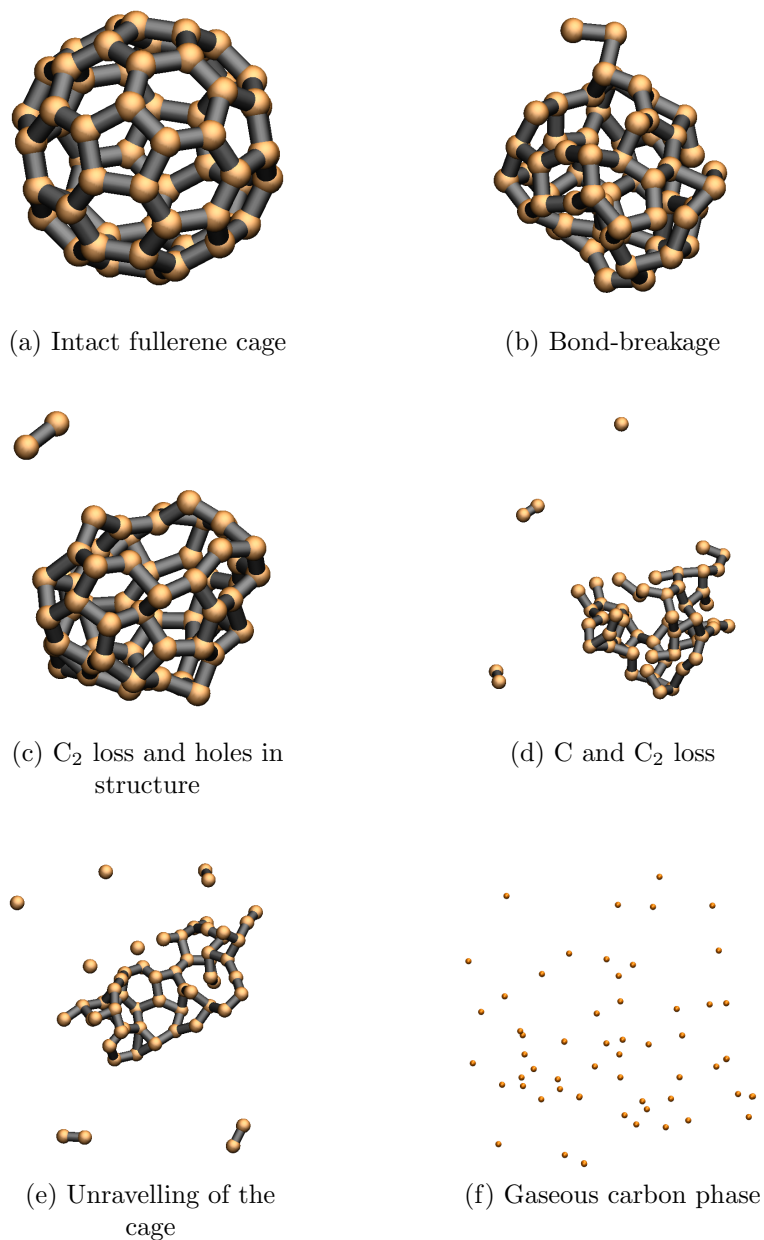


Figure 4.9: Snapshots of the  $C_{60}$  fragmentation process at the phase transition temperature (as calculated using the Topologically-constrained forced-field). The snapshots (a)–(e) occur between 0–200 ns, prior to the total energy jump shown in Fig. 4.8.

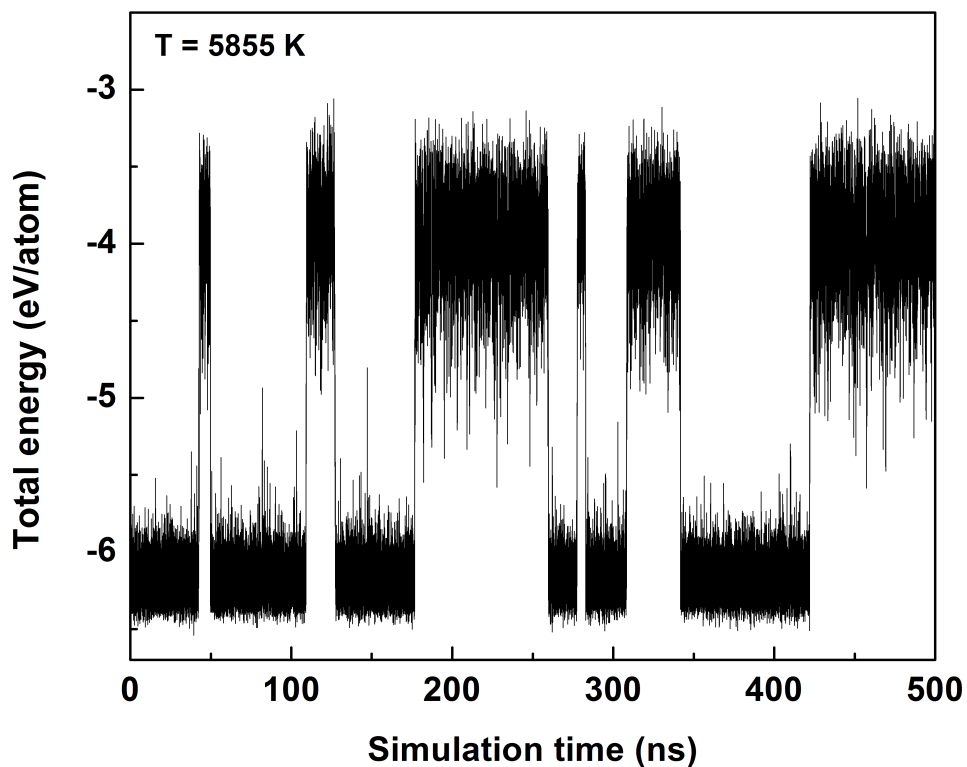


Figure 4.10: Consecutive oscillations in the time-dependent total energy of  $C_{60}$ , as calculated using the Topologically-constrained forcefield. The oscillations indicate that  $C_{60}$  shows a coexistence between the cage and gaseous phases—dynamically, this translates to consecutive fragmentation and re-assembly of the carbon cage at the phase transition temperature of 5855 K. Note that the simulation volume is  $8 \times 10^3 \text{ \AA}^3$  and the total simulation time is 500 ns.

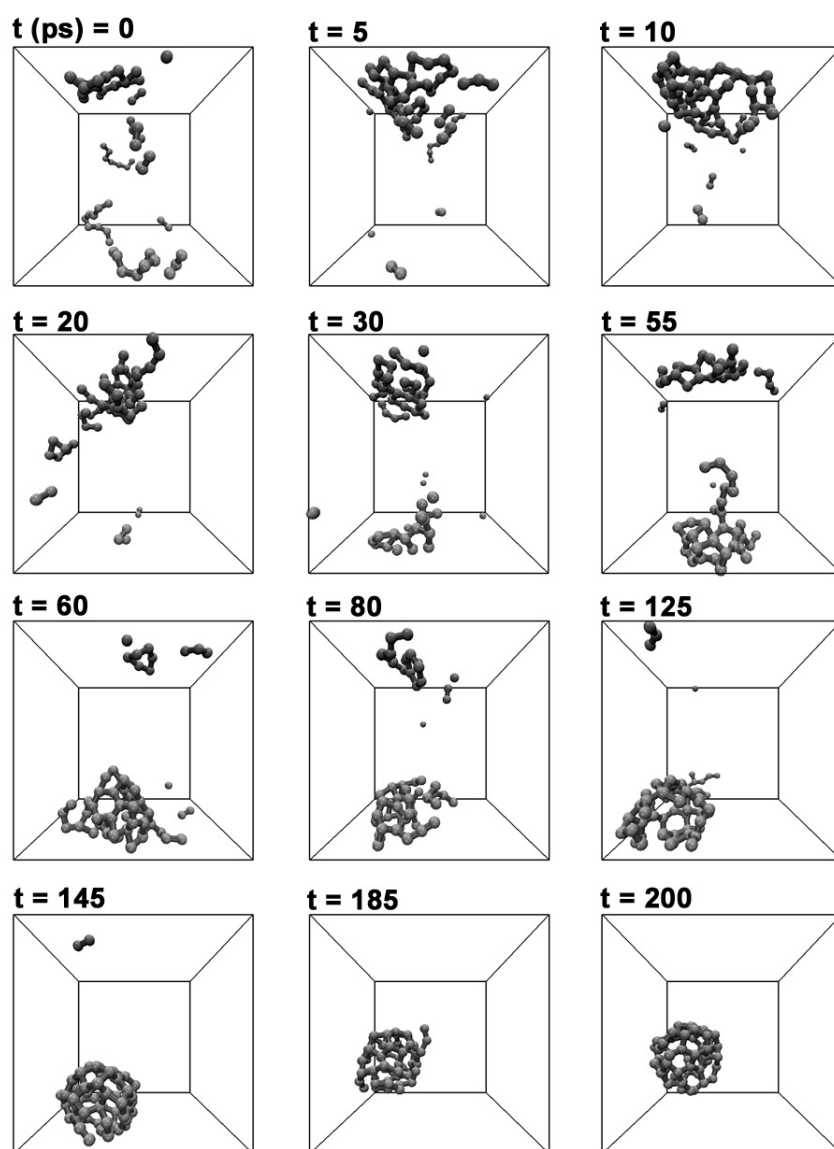


Figure 4.11: Reassembly of the  $C_{60}$  cage at the phase transition temperature using the Topologically-constrained forcefield. The times indicated above each panel refers to the relative time between panels. The simulation was conducted in a volume of  $8 \times 10^3 \text{ \AA}^3$ .

and formation of a fullerene are observed several times in the course of the simulation.

### 4.3 STATISTICAL MECHANICS MODEL

In the previous section, we have discussed the results of the molecular dynamics simulations for a topologically-free and topologically-constrained  $C_{60}$ , based on the Tersoff potential and the Topologically-constrained forcefield respectively. The topologically-free system exhibited a variety of metastable phases—either short-lived phases prior to a first-order phase transition (as is the case in the large simulation volume,  $1.25 \times 10^8 \text{Å}^3$ ), or as long-lived metastable graphene phases prior to a second-order-like phase transition (as seen in the small simulation volume,  $8 \times 10^3 \text{Å}^3$ ).

For the topologically-constrained  $C_{60}$ , the system was shown to experience only first-order-like phase transition in either simulation volume. However, in the small simulation volume, a phase coexistence between the  $C_{60}$  fullerene cage and a gaseous phase of carbon dimer, short chains and rings was obtained. Furthermore, in both simulation volumes, the topologically-constrained system is found to reduce to a simple two-state system. In this section, we develop a statistical mechanics model based on the results of the molecular dynamics simulations of the topologically-constrained  $C_{60}$  in the small simulation volume of  $8 \times 10^3 \text{Å}^3$ .

In order to construct the statistical mechanics model, we have assumed a two state system where the initial state is the  $C_{60}$  fullerene and the final state is a gas of 30  $C_2$  molecules. Therefore, the coexistence behaviour at the phase transition temperature corresponds to the continuous fragmentation and reassembly of the fullerene cage to, and from, a gas of 30  $C_2$  molecules only. Hence, we have only considered the  $C_{60} \leftrightarrow 30C_2$  channel within the statistical mechanics model. However, at low temperatures, this channel is unlikely to be prominent as small chains and rings are likely to play some role in formation and disintegration of the  $C_{60}$ . For this reason, the model is limited to only consider conditions where the temperatures are above 3000 K.

An example of such environment, is the high-temperature arc region of

fullerene-generating arc-discharge experiments—where temperatures within the arc zone are between 4000-6000 K [28] and the  $C_2$  concentration is much higher than  $C_3$  [158, 159]. We therefore base the statistical mechanics model on generalised temperature and pressure conditions in arc-discharge experiments, assuming local thermodynamic equilibrium. However, it should be noted that in the actual experimental conditions, a variety of factors influence the formation of fullerenes, including the temperature gradient, the presence of charged species, the temperature of the buffer gas, the presence of residual gas species and the emission of UV radiation from the arc. Additionally, it should be noted that the statistical mechanics model does not account for charged species. In its current form, it focuses only on the neutral case.

Within these conditions, we then consider a two-state system with an initial state of  $f$ , the  $C_{60}$  fullerene cage and a final state of  $g$ , the gas of 30  $C_2$ . Thus, at the phase transition temperature  $T_c$ , we can write the entropy change of the system as

$$\Delta S^0 = \frac{dU + P\Delta V}{T_c}, \quad (4.1)$$

where  $\Delta S^0 = S_g - S_f$  is the entropy difference between the gaseous  $S_g$  and the fullerene  $S_f$  phases,  $dU$  the change in internal energy,  $P$  the pressure and  $\Delta V$  the change in volume. Note that, instead of a gas of fullerene molecules, we are only considering the phase transition of a single  $C_{60}$  molecule to a gas of dimers, although the generalisation to an ensemble of  $N$  statistically-independent fullerene molecules is straightforward. We also assume that this final state of the system consists of 30 statistically independent carbon dimers. A further assumption is that these  $C_2$  molecules originate from the 30 (6-6) bonds in the  $C_{60}$ . As is known, the  $C_{60}$  has two types of bond lengths corresponding to the edges of a pentagon and a hexagon, the (5-6) bond, and to the edges of two hexagons, the (6-6) bond [119]. The pentagonal faces are necessary to introduce curvature into an otherwise planar sheet of hexagons. As a result, these (5-6) bonds are slightly longer than their (6-6) counterpart, and are known to be more reactive [31]. Hence, our work assumes that in the course of the fragmentation of  $C_{60}$ , all 60 of these (5-6) bonds are broken



to form a carbon gas of 30 C<sub>2</sub>. Therefore, the change in internal energy  $dU$  in equation (4.1) can be expressed as  $60E^s - \frac{5}{2}N_gkT_c$ , where the first term consists of the energy of the sixty broken (5-6) bonds, while the second term is the thermal energy of  $N_g$  (=30) dimers at the phase transition temperature. Thus, equation (4.1) can be expanded as

$$\begin{aligned}\Delta S^0 &= \frac{60E^s - \frac{5}{2}N_gkT_c + P\Delta V}{T_c} \\ &= \frac{60E^s - \frac{5}{2}N_gkT_c + (N_g - N_f)kT_c}{T_c} \\ &= \frac{60E^s}{T_c} - \frac{3}{2}N_gk + N_fk\end{aligned}\quad (4.2)$$

where the term  $P\Delta V$  refers to the work done in external pressure when the fullerene cage fragments to a gas of  $N_g$  dimers. The volume change  $\Delta V$  refers to the difference in the volumes of the dimer gas  $V_g$  and the fullerene gas  $V_f$  respectively. The Boltzmann constant is  $k$  and  $N_f$  is the number of fullerene molecules at a given temperature. The term  $P\Delta V$  has been rewritten as  $P(V_g - V_f) = (N_g - N_f)kT_c$  assuming ideal gas conditions.

Due to the nearest-neighbour restriction in the Topologically-constrained forcefield, the system could only explore a *single* C<sub>60</sub> ↔ 30C<sub>2</sub> channel in the simulations. In order to lift this restriction and to consider the case where the system is able to explore *all* possible C<sub>60</sub> ↔ 30C<sub>2</sub> channels, we need to add additional terms to the entropy change  $\Delta S = S_g - S_f$  between the gas  $S_g$  and the fullerene  $S_f$  phases:

$$\Delta S = \Delta S^0 + \Delta S^{corr} + \Delta S^{expt} \quad (4.3)$$

where  $\Delta S^0$  is the entropy change at 5855 K (the phase transition temperature obtained from the molecular dynamics simulation) as introduced in Eq. 4.1. The second and third terms are  $\Delta S^{corr}$ , the statistical correction term and  $S^{expt}$ , the pressure correction term.  $\Delta S^{corr}$  is necessary to amend for the static neighbours list of the Topologically-constrained forcefield. This static list causes each carbon atom to recognise only its 3 nearest-neighbours which

have been specified at the beginning of the simulation. Hence, it is only with these neighbours that each atom is able to form and break bonds, causing the system to be effectively constrained to only one particular bonding combination. To correct for this limitation, the term  $\Delta S^{corr}$  has been added to account for all the possible combinations that a system of 30 *indistinguishable* dimers can be arranged to form the  $C_{60}$  fullerene cage. Thus, there should be  $30! 2^{30}$  possible states available to the system—all of which would lead to the same  $C_{60}$  cage structure:

$$\Delta S^{corr} = -k \ln(2^{30} 30!). \quad (4.4)$$

Additionally, pressure corrections must also be accounted for. In arc discharge experiments, the chamber pressure is measured as the pressure of the buffer gas, which is usually helium. For the formation of fullerenes to occur, this buffer gas is necessary to cool down the hot gas of carbon dimers from the plasma arc. However, the concentration of the carbon and the buffer gas is not uniform in the chamber. Rather, in the vicinity of the electrodes, the concentration of carbon is high in comparison to the low concentration of helium due to the continuous flux of carbon from the electrode (see [28, 158–162] for experimental measurements of the dependencies of temperature and concentration on the distance from the electrodes). However, the pressure in the chamber can be considered as uniform since the process of pressure equilibration is much faster at experimental conditions than the process of concentration homogenisation. This is because the former is related to the speed of sound while the latter is related to diffusion within the chamber. With this assumption we will then refer to the pressure of the buffer gas as the pressure of carbon gas, in the vicinity of the high-temperature arc region, which we shall consider to be the fullerene formation region.

The pressure in our small simulation volume ( $\sim 0.4$  GPa) is much higher than the pressure at which experiments are performed due to the small volume of the box. To correct for this, we have added  $\Delta S^{expt}$  to the entropy change:

$$\begin{aligned}
\Delta S^{expt} &= 30k \ln \left( \frac{V_{expt}}{V_{sim}} \right) - k \ln \left( \frac{V_{expt}}{V_{sim}} \right) \\
&= 30k \ln \left( \frac{n_{sim}}{n_{expt}} \right) - k \ln \left( \frac{n_{sim}}{n_{expt}} \right) \\
&= 29k \ln \left( \frac{n_{sim}}{n_{expt}} \right),
\end{aligned} \tag{4.5}$$

where the first term refers to the entropy correction due to a gaseous state of 30 statistically independent dimers when varied from the small simulation volume  $V_{sim}$  to an arbitrary volume  $V_{expt}$ , e.g. the volume used in experimental conditions; while the second term is identical but refers to a fullerene molecule instead. In both cases, the entropy of the dimer gas (or fullerene molecule) is proportional to the logarithm of the volume accessible to it. The volume terms can then be rewritten in terms of concentrations  $n_{expt} = N/V_{expt}$  and  $n_{sim} = N/V_{sim}$ . However, if we assume ideal gas conditions, the concentration terms can be expressed as:

$$n_{expt} = \frac{P_p}{kT} \quad \text{and} \quad n_{sim} = \frac{30}{V_{box} - V_{exc}}, \tag{4.6}$$

where  $P_p$  and  $T$  are the  $C_2$  partial pressure and temperature terms in the experimental setup,  $k$  the Boltzmann constant and 30 refers to the fact that there are 30 dimers in the system when the fullerene has fully fragmented. The volume terms  $V_{box} = 8000 \text{ \AA}^3$  and  $V_{exc}$  refer respectively to the volume of the simulation box and the excluded volume due to the van der Waals repulsion between the atoms:

$$V_{exc} = 30 \left( \frac{4\pi}{3} \right) r^3, \tag{4.7}$$

where  $r$  is the minimum distance two atoms can approach each other. The excluded volume can be estimated through the distance at which the repulsion energy between dimers is equal to  $kT_c$ , where  $T_c = 5855 \text{ K}$  is the phase transition temperature determined from the simulations. This distance  $r(T)$  is then calculated as the root of the following equation:

$f_0$	$T_c$	$A$	$w_1$	$w_2$	$w_3$
0.0030	4347.5611	1.0404	$3.1556 \times 10^{-22}$	316.4865	374.3965

Table 4.2: Fitting parameters for the  $C_2$  molefraction

$$\epsilon \left[ \left( \frac{\sigma}{r} \right)^{12} - 2 \left( \frac{\sigma}{r} \right)^6 \right] = kT_c, \quad (4.8)$$

where  $\epsilon$  and  $\sigma$  are the parameters of the forcefield given in Table 2.2. Having determined  $r$ , we find that  $V_{exc}$  has a value of  $822 \text{ \AA}^3$ . With these, we can then rewrite  $\Delta S^{expt}$  as

$$\Delta S^{expt} = 29k \ln(n_{sim}) - 29k \ln \left( \frac{P_p}{kT} \right). \quad (4.9)$$

However the  $C_2$  partial pressure  $P_p$  can be rewritten as  $m(T) \times P$ , where  $m(T)$  is the temperature-dependent molefraction of  $C_2$  in the carbon vapour and  $P$  is the chamber pressure. The  $C_2$  molefraction function was derived from the temperature-dependent equilibrium concentration of the carbon vapour ( $C-C_5$ ) in an arc-discharge experiment, as given in Ref [159] Similar plots can be found in Refs. [158, 162] for different carbon vapour pressures. Using the distribution of Ref. [159], we have calculated the molefraction of  $C_2$  in a carbon vapour composed of C atoms and molecules of  $C_2$  and  $C_3$ . Although the original distribution contained the concentrations of  $C_4$  and  $C_5$  as well, we have neglected these two species in the current model as their concentrations are significantly much lower than  $C_2$ . Therefore, we have only accounted for the primary components of the carbon vapour (C,  $C_2$  and  $C_3$ ) at temperatures of 3000-7000 K.

The calculated molefractions are presented in Fig. 4.12, where the inset of the figure shows the curve of the temperature-dependent  $C_2$  molefraction that has been fitted with the following equation:

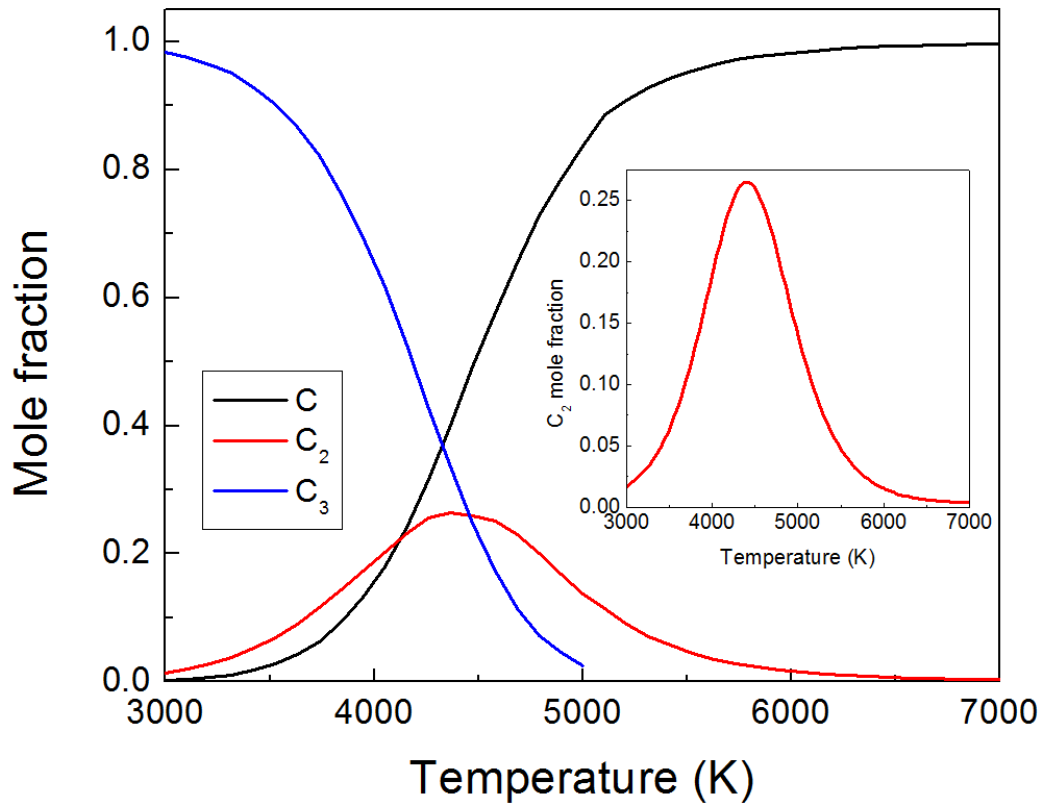


Figure 4.12: Molefraction of the carbon vapour consisting of the C, C<sub>2</sub> and C<sub>3</sub> species. The distribution is based on the equilibrium concentration of the carbon vapour in an arc-discharge experiment, as given in Ref. [159]. *Inset:* the C<sub>2</sub> molefraction fitted using equation 4.11 with parameters given in Table 4.3.

$$m(T) = f_0 + A \left( \frac{1}{1 + e^{-(2T-2T_c+w_1)/2w_2}} \right) \cdot \left( 1 - \frac{1}{(1 + e^{-(2T-2T_c-w_1)/2w_3})} \right), \quad (4.10)$$

where the values of each parameter is given in Table 4.3. Thus, while we may not specifically account for the presence of C and  $C_3$  molecules in our current model (as we are mainly interested in the  $C_{60} \leftrightarrow 30C_2$  channel), we can account for their influence in terms of the partial pressure. Using equation 4.11, we can then rewrite equation 4.9 as

$$\Delta S^{expt} = 29k \ln(n_{sim}) - 29k \ln \left( \frac{m(T) \cdot P}{kT} \right). \quad (4.11)$$

Therefore, for a system experiencing a transition between the phases of  $C_{60} \leftrightarrow 30C_2$ , we can evaluate its phase transition temperature as the root of the following equation:

$$\begin{aligned} T &= \frac{60E^s - \frac{5}{2}N_g kT + P\Delta V(T)}{\Delta S(P, T)} \\ &= \frac{60E^s - \frac{5}{2}N_g kT + (N_g - N_f)kT}{\Delta S^0 + \Delta S^{corr} + \Delta S^{expt}} \\ &= \frac{60E^s - \frac{3}{2}N_g kT + N_f kT}{\Delta S^0 + \Delta S^{corr} + \Delta S^{expt}} \end{aligned} \quad (4.12)$$

where the entropy term  $\Delta S(P, T)$  is dependent on the experimental chamber pressure  $P$  and temperature  $T$  respectively. As in equation 4.2,  $E^s$  is the energy of one single C-C bond,  $\Delta V$  is the change in volume between the fullerene and gaseous  $C_2$  states,  $N_g$  is the number of gaseous carbon dimers (=30),  $N_f$  is the number of fullerene molecules (=1),  $k$  is the Boltzmann constant and  $\Delta S^0$ ,  $\Delta S^{corr}$  and  $\Delta S^{expt}$  are respectively given in equations 4.2, 4.4 and 4.11.

In Fig. 4.13, we evaluate equation 4.12 and plot the relation of the phase transition temperature on pressure. The plot shows two main curves (solid

black and dashed red lines) corresponding to two different concentrations of  $C_2$  molecules in the carbon gas. The first curve (solid black line) describes the dependence of the phase transition temperature on pressure when the carbon gas consists entirely of  $C_2$  molecules, *i.e.* when the  $C_2$  molefraction is  $m(T) = 1$ . The second curve (dashed red line) describes the same dependence when the carbon gas is a mixture of C,  $C_2$  and  $C_3$  molecules in the proportions given by Ref. [159]. Namely, this second curve corresponds to the conditions when the molefraction of  $C_2$  is less than 0.3 according to the distribution in [159]. As seen in Fig. 4.13, this second curve demonstrates lower phase transition temperatures compared to the first curve (solid black line). Note that the second curve (red dashed line) is plotted from 3000 K as this is the starting temperature given in the distribution of Ref. [159].

Nevertheless, both curves show that lowering the pressure causes a decrease in the phase transition temperature. However, if the pressure is lowered considerably, the equilibration time increases exponentially with the decrease of the phase transition temperature, and at some point it should exceed the available experimental time limits. Conversely, if the pressure is significantly high, it is not possible to consider the gas of  $C_2$  dimers in the ideal gas approximation. Therefore, the thin black line of the curve in Fig. 4.13 marks the estimated upper and lower limits of pressure of our model.

In the inset shown in Fig. 4.13, we have plotted the chamber pressure and the temperature range of the arc-discharge experiments reported in Refs. [28, 158–161]. In these experiments, the temperature decreases with different gradients from the centre of the arc. The temperature values plotted in Fig. 4.13 correspond to the region 3–6 mm away from the arc centre. Since each of the experiments cited in Fig. 4.13 uses electrodes 6 mm in diameter, this corresponds to the region from the edge of the electrode (3 mm from the arc centre) to a further 3 mm away (6 mm from the arc centre). Note that we have only consider experiments where the currents are above 70 A, as this will ensure that the buffer gas plays has a minimal concentration in the arc zone [158, 162]. The experimental temperatures and pressures have a better agreement with the first curve (solid black line), where the

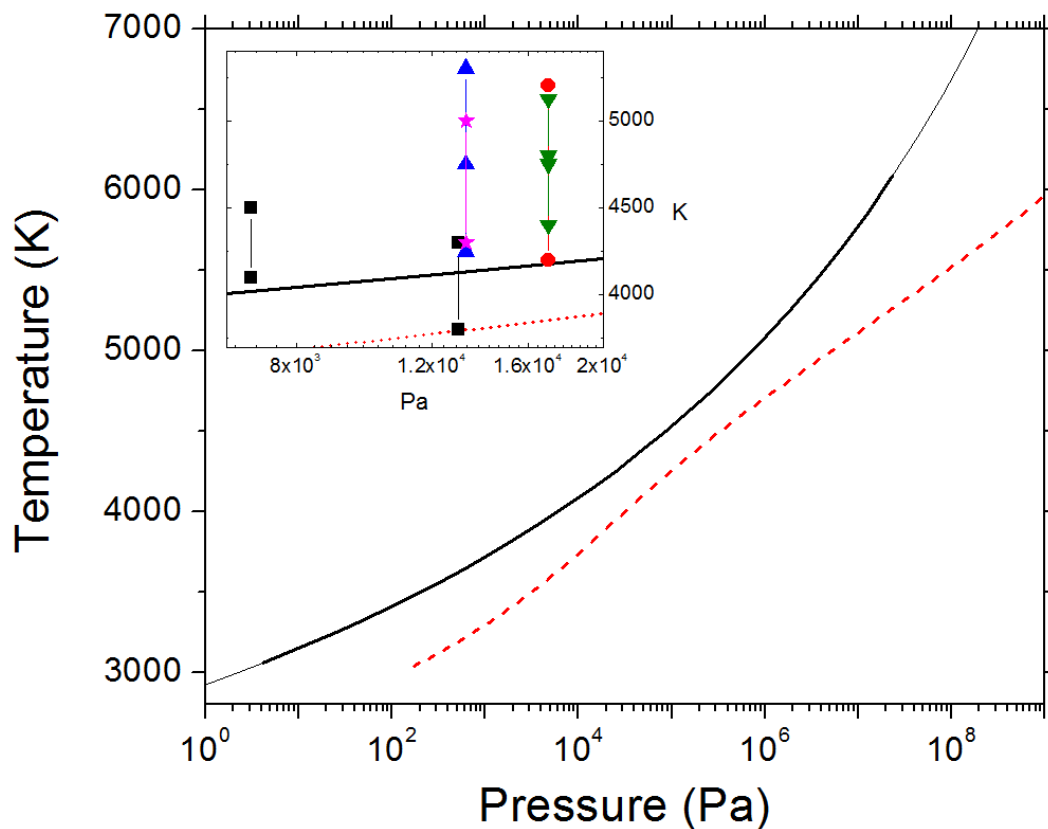


Figure 4.13: Dependence of the phase transition temperature on pressure. *Thick black line*: results of the model when the  $C_2$  partial pressure is equivalent to the chamber pressure. The model is estimated to be valid in the pressure range marked by the thick black line. *Dashed red line*: results of the model when the  $C_2$  partial pressure is given by the distribution in Ref. [159], see text for further details. *Inset*: all cited arc-discharge experimental works were conducted using a 6 mm electrode diameter. The current and chamber pressure are given in the brackets for each respective work. ★ [160] for (100 A, 13.3 kPa), ▲ [161] for (86 A and 131 A, 13.3 kPa), ▼ [158] for (88 A and 120 A, 17 kPa), ■ [28] for (100 A, 7 kPa) and (85 A, 13 kPa) and • [159] for (75 A, 17 kPa).



carbon gas comprises of only  $C_2$  molecules. Nonetheless, a few points must be noted together with this statement. As described previously, the plotted temperature values correspond to different regions away from the centre of the arc. However, it remains uncertain where the actual region of fullerene formation is located. Indeed, with the increasing distance away from the arc, the temperature continuously decreases until it reaches the temperature of the chamber wall (which would be room temperature unless the experiment is conducted in a temperature-controlled arc-furnace). Therefore, depending on the parameters of the experiment, the conditions in the arc-discharge chamber is likely to be strongly inhomogeneous, with many factors affecting the fullerene formation process, including the presence of residual gas species, such as nitrogen which adversely decreases the  $C_{60}$  yield [28].

Finally, one should keep in mind that although in all the cited experiments the formation of fullerenes is observed, the obtained yields of  $C_{60}$  compared to, *e.g.* soot or the total yield of fullerenes ( $C_{70}$ ,  $C_{84}$ , etc.), differ from one experiment to the other. It still remains unclear how the temperature and pressure conditions influence the final yields and ratios of the produced fullerene species. As the current statistical model only investigates the phase transition of  $C_{60}$ , the comparison shown in Fig. 4.13 between the model and arc-discharge experiments contains some ambiguity, and consequently should be considered as a qualitative comparison.

Despite so, some conclusions can be made. Fig. 4.13 indicates that if the phase transition of  $C_{60}$  is to take place within the  $C_{60} \leftrightarrow 30C_2$  channel, then this is more likely to occur when the concentration of  $C_2$  is dominant within the carbon vapour produced by the graphite arc. Therefore, the solid black curve of Fig. 4.13 can be considered as the upper limit of our model—denoting the occurrence of the  $C_{60}$  phase transition within 6 mm from the centre of the arc (4000-4500 K) at pressures of 10-100 kPa. Correspondingly, if the concentration of  $C_2$  in the carbon vapour is low, then at pressures 10-100 kPa, the phase transition of  $C_{60}$  occurs at a lower temperature (3500-4200 K) and takes place further away (about 8 mm) from the arc centre. Thus, the dashed red curve of Fig. 4.13 can be considered as the lower limit of our model.

## 4.4 CHAPTER SUMMARY

In this chapter, we have presented the results of the molecular dynamics simulations of  $C_{60}$  using the Tersoff and the Topologically-constrained forcedfield (TCF).

We have discussed the effect of the simulation time and volume on the phase transition properties of  $C_{60}$ , and have shown that the  $C_{60}$  exhibits a different behaviour within the topologically-free (Tersoff) and topologically-constrained (TCF) cases.

For the topologically-free system,  $C_{60}$  transforms into a series of metastable phases before multifragmentation into a carbon gas when simulated in a large ( $1.25 \times 10^8 \text{ \AA}^3$ ) simulation box. Within the small simulation volume ( $8 \times 10^3 \text{ \AA}^3$ ), the  $C_{60}$  transforms into a long-lived metastable phase of graphene and shows a continuous phase transition (second-order).

The behaviour of  $C_{60}$  within the large ( $1.25 \times 10^8 \text{ \AA}^3$ ) simulation volume, for the topologically-constrained case, is similar to that of the topologically-free  $C_{60}$ , with the exception that no metastable transformations were observed; only the single jump in energy indicating fullerene fragmentation. However, within the small simulation volume, the  $C_{60}$  exhibits a dynamic phase coexistence at the phase transition temperature. Effectively, the  $C_{60}$  continuously fragments and re-assembles back into the fullerene cage within a single trajectory. Based on this phase coexistence, we have developed a statistical mechanics model which generalises the simulation results to an idealised depiction of the typical conditions within arc-discharge experiments. Using this statistical mechanics model, we were able to indicate the temperature and pressure conditions of the fullerene formation and fragmentation within the  $C_{60} \leftrightarrow 30C_2$  channel, as shown in Fig. 4.13.

## CHAPTER 5

# NANOCARBON TRANSITIONS

In this chapter, we investigate the phase transition properties and the stabilities of fullerenes from  $C_{32}$  to  $C_{540}$ . In particular, we investigate the behaviour of these fullerenes prior to multifragmentation to a phase of carbon gas. We then further this discussion by considering the stabilities and transformations of a cluster of 240 carbon atoms in the form of a fullerene, a graphene, a buckyball, a  $C_{60}@C_{180}$  carbon onion and an uncapped (10,10) nanotube fragment [2].

## 5.1 STABILITY OF FULLERENES LARGER THAN C<sub>60</sub>

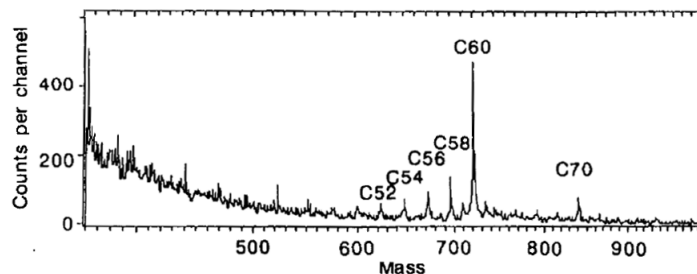


Figure 5.1: Typical time-of-flight mass spectra indicating the high abundance of C<sub>60</sub>. This particular spectra was produced by resistive heating of graphite rods [27]

The extraordinary abundance of C<sub>60</sub> in fullerene-generating experiments is well-known, though the underlying origin of this phenomena is yet to be fully understood. In the twenty-five years since its discovery, considerable work has gone into understanding the stability of C<sub>60</sub> and the conditions leading to high C<sub>60</sub> yields. A decisive factor for this was the discovery of a simple yet effective method for generating macroscopic quantities of C<sub>60</sub>—resistive heating of graphite [27], and its successor, the arc-discharge method [28, 160, 160, 161]. In contrast, there is no specific method to produce fullerenes of larger sizes in bulk—especially giant fullerenes. Rather, fullerenes of larger sizes are usually created in small proportions together with C<sub>60</sub> in arc-discharge and laser vapourisation experiments.

The only exception to this is the production of C<sub>70</sub> in combustion methods, where the maximum ratio of C<sub>70</sub> to C<sub>60</sub> yield can be as high as 129% [164]. However, arc-discharge experiments using boron-doped graphite electrodes have been demonstrated to produce larger fullerenes whose yields are twice as high as in conventional arc-discharge methods employing pure graphite rods [163].

The effect of the buffer gas temperature has also been shown to influence the proportion of C<sub>60</sub> to larger fullerenes in the soot generated. The arc furnace experiment of Song *et. al.* showed that with a buffer gas temperature

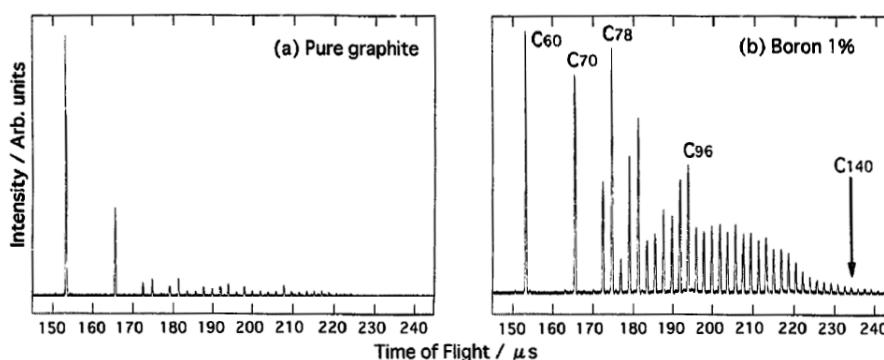


Figure 5.2: Time-of-flight mass spectra of carbon extracted soot prepared by the arc-discharge of (a) a pure graphite rod and (b) 1% boron-doped graphite rod [163].

of 500°C, the yields of larger fullerenes is dominant [165]. However, it should be noted that at this temperature, the total fullerene yield is just under 5%, while at 200°C where the  $C_{60}$  yield is dominant, the total fullerene yield is 30.6% of the total soot content. Therefore, it is entirely possible that increasing the buffer gas temperature affects mostly  $C_{60}$  formation but may not significantly increase the formation of larger fullerenes. A related experiment involving a laser furnace also demonstrated the dependence of  $C_{60}$  yields on the buffer gas temperature. However the investigators also showed that the soot which contains mostly larger fullerenes is formed further away from the graphite target, while the soot containing  $C_{60}$  and  $C_{70}$  occurred nearer to the graphite target [166]. Such a result may indicate kinetic effects in the annealing process of the hot carbon vapour.

In fact, kinetic factors and the particular formation mechanism may play significant roles in explaining the abundance spectra of fullerenes. Energetically, it is known that all fullerenes larger than  $C_{60}$  should be more stable according to their binding energies. However, the discrepancy between the results of the abundance spectra and the predictions of the binding energy has shown that binding energy is not a good criterion for describing fullerene stability. Alternative criteria such as chemical reactivity or the HOMO-LUMO gaps may show some selective stability for the  $C_{60}$ , although the magnitude

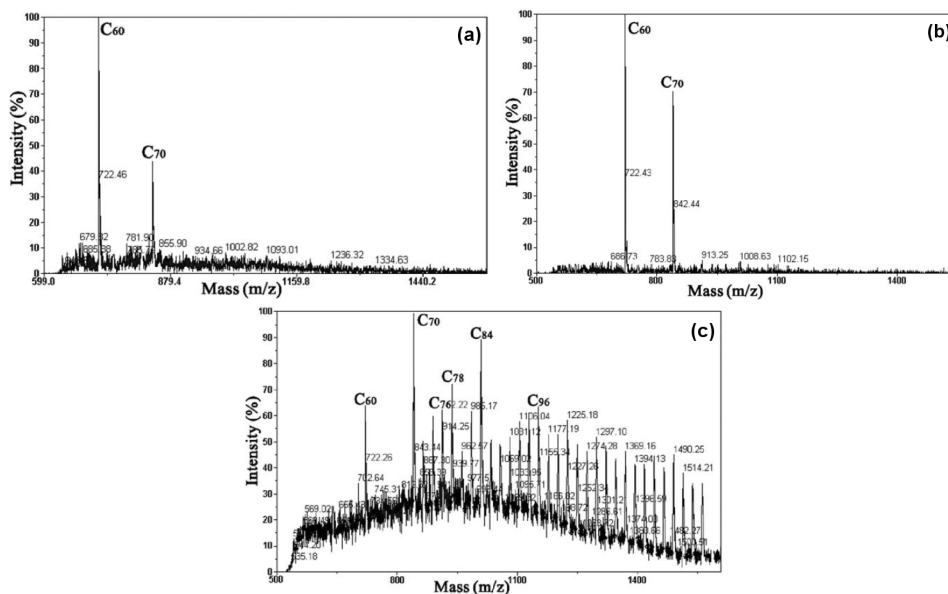


Figure 5.3: Time-of-flight mass spectra of the raw soot produced in an arc furnace [165] at: (a) room temperature, (b) 200°C and (c) 500°C.

of the difference between  $C_{60}$  and larger fullerenes is not significantly pronounced enough to explain the particular stability of  $C_{60}$ —or the particular instability of larger fullerenes. Moreover, the instability of larger fullerenes is also seen in the solid state [167]. 70% of a sample of  $C_{84}$  stored as a solid in air and “semi-darkness” for a period of two years was shown to have degraded into material insoluble in all fullerene solvents; while 100% of a sample of  $C_{2v}(\text{II})$ -isomer of  $C_{78}$  did not dissolve after 20 weeks within the same conditions. In comparison, a solid sample of  $C_{60}$  stored in air for *seven years* can still be dissolved in a fullerene solvent, albeit with some amount of insoluble material.

### 5.1.1 PHASE TRANSITIONS OF $C_{32}$ TO $C_{540}$

In this subsection, we will extend our study from  $C_{60}$  to a family of fullerenes—in particular:  $C_{32}$ ,  $C_{70}$ ,  $C_{80}$ ,  $C_{90}$ ,  $C_{180}$ ,  $C_{240}$  and  $C_{540}$ , as depicted in in Fig. 5.4. As with  $C_{60}$  in Chapter 4, we have performed molecular dynamics simulations using the Tersoff potential. However, we have only conducted

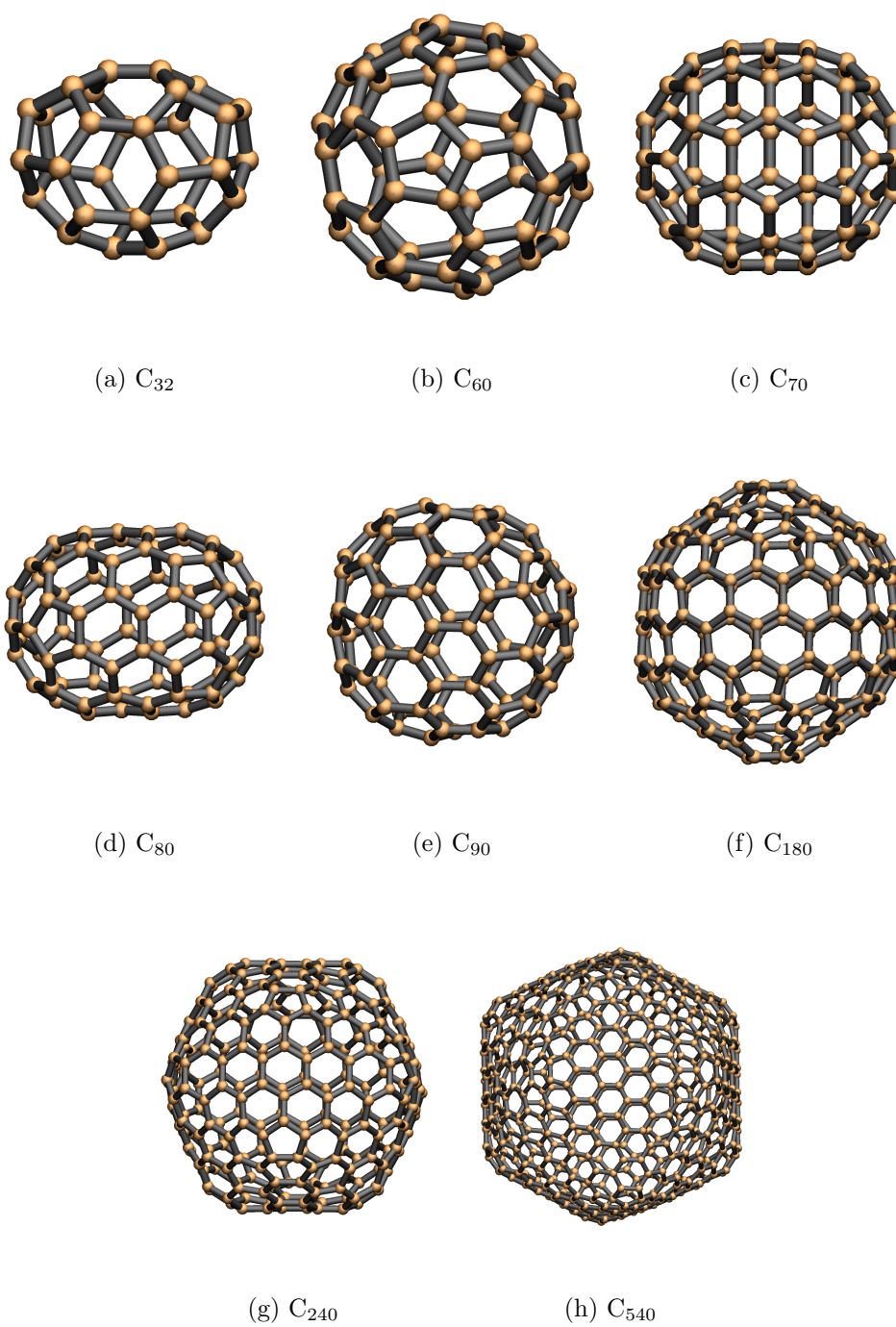


Figure 5.4: Fullerenes investigated in this subsection.

short simulations of 50 ns, although longer simulations of 500 ns were performed for selected fullerenes (namely  $C_{32}$ ,  $C_{70}$  and  $C_{240}$ ).

In Fig. 5.5, we present the resulting caloric curves and heat capacity plots as derived from the molecular dynamics simulations. Note that we have used the results of the 50 ns simulations for the caloric curve and heat capacity of  $C_{60}$ . For comparison with the results of longer simulations, please refer to Chapter 4.

As is evident from Fig. 5.5, the phase transition temperature—determined from the peak of the maximum of the heat capacity plots—increases with increasing fullerene size. Thus, the caloric curves indicate that, the bigger the fullerene is, the higher is the energy (higher temperature) needed to pump into the system such that the fullerene cage is totally disintegrated into a system of non-interacting gaseous carbon atoms. At the same time, the caloric curves also suggest that the stability threshold of the fullerene cage increases with increasing size. However, this inference can be misleading and a cursory glance at the corresponding heat capacity plots indicates that the situation is more complicated.

The heat capacity plots in Fig. 5.5 show that the heat capacity per atom (the specific heat capacity) decreases after a maximum value at  $C_{60}$ . In fact, the heat capacity per atom of  $C_{240}$  and  $C_{540}$  are about five times smaller than  $C_{60}$ . From this, one can infer that perhaps different mechanisms are at play during the fragmentation of the fullerene to a system of gaseous carbon atoms, such that the energy required for fragmentation is somehow distributed in different fullerene sizes. Nevertheless, it is also important to keep in mind that these are heat capacity plots of 50 ns long simulations. As have been discussed in Section 4.1 of Chapter 4, with increasing simulation time, the heat capacity becomes sharper due to a similar sharpening in the jump of the caloric curve.

The observation of an increasing phase transition temperature with size is associated with the monotonic increase of binding energy per atom with fullerene size. As the number of carbon atoms increases, the fullerene starts to approach the case of an ideal graphite crystal (or an ideal graphene sheet, as the fullerene is a monolayer). Thus, while the  $C_{60}$  is often associated



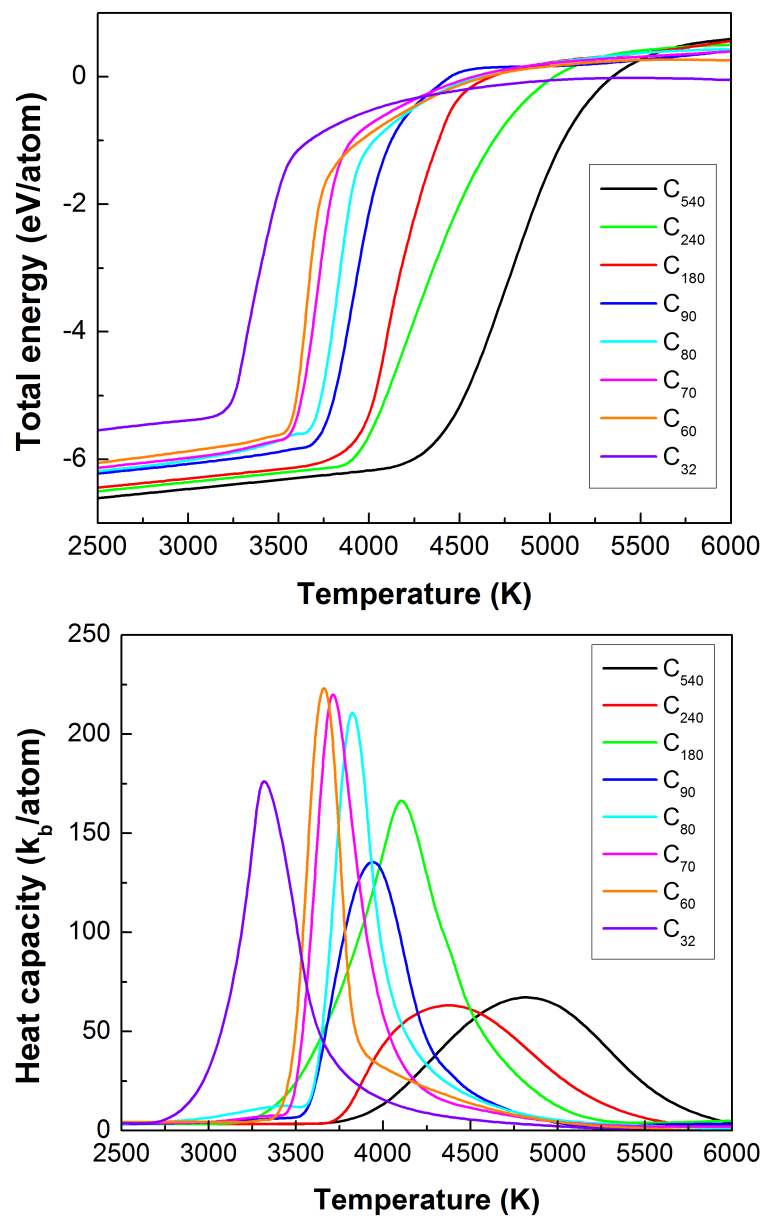


Figure 5.5: Caloric curves (top) and heat capacities (bottom) of fullerenes  $C_{32}$  to  $C_{540}$ . The phase transition temperatures indicated by the maximum of the heat capacity peaks are  $C_{32}$ : 3320 K,  $C_{60}$ : 3658 K,  $C_{70}$ : 3715 K,  $C_{80}$ : 3820 K,  $C_{90}$ : 3945 K,  $C_{180}$ : 4103 K,  $C_{240}$ : 4388 K and  $C_{540}$ : 4825 K.

with being the most “stable” fullerene, due to its surprisingly high yields in fullerene-producing experiments, this stability is in fact not due to energetic reasons, but is more likely to be attributed to kinetic factors or specific formation mechanisms.

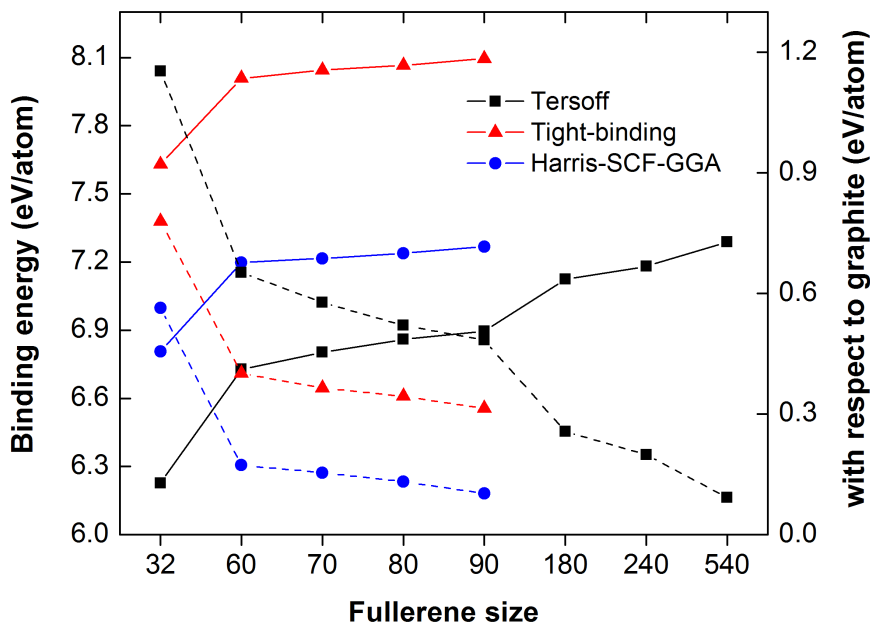


Figure 5.6: *Solid lines* indicate the binding energy as calculated using the Tersoff potential (black squares), tight-binding method (red triangles) and Harris-SCF-GGA (blue circles). *Dashed lines* show the binding energy of each fullerene with respect to the binding energy of graphite ( $E_{\text{graphite}} - E_{\text{fullerene}}$ ), as calculated within each method.

In Fig. 5.6, we present the change in binding energy with fullerene size as calculated using: the Tersoff potential (this work), tight-binding method [168] and Harris-GGA with SCF-GGA corrections [169]. Although the agreement is not tight between the absolute values of the binding energies calculated using different methods, the trends displayed are very similar. Namely, that the binding energy increases with size and that above 90 carbon atoms, the fullerene binding energy closely approaches that of graphite.

### 5.1.2 FRAGMENTATION DYNAMICS

Thermal heating of larger fullerenes in an oven has been conducted by Cross and Saunders for  $C_{70}$ ,  $C_{76}$ ,  $C_{78}$  and  $C_{84}$  [170]. No decomposition of the fullerenes were found at  $650^\circ\text{C}$  after 40 s in the oven. However, decomposition was observed from  $1050^\circ\text{C}$ , though it should be noted that this should not be considered a “phase transition”-like fragmentation as the original fullerene source was not completely decomposed. Specifically,  $C_{76}$  was found to decay into  $C_{70}$  and  $C_{60}$ ; while  $C_{78}$  and  $C_{84}$  both decayed to  $C_{76}$  and  $C_{60}$  (and additionally  $C_{68}$  for  $C_{84}$ ). However, when  $C_{70}$  was heated, there was no decomposition to  $C_{60}$ .

Similarly, surface-induced dissociation of  $C_{70}$  and  $C_{164}$  were investigated on pyrolytic graphite [171], silicon and gold surfaces, as well as self-assembled monolayers [172]. In these works, it was shown that the main mechanism of decay is through  $C_2$  loss below a certain fragmentation threshold, above which multifragmentation occurs. Additionally, the type of the surface also affects the resilience of fullerenes. Computationally, surface-induced fragmentation of  $C_{60}$ ,  $C_{100}$  and  $C_{240}$  have also been studied where it was shown that  $C_{60}$  is the most stable structure against fragmentation, while  $C_{240}$  the least [63].

The primary mechanism in these highlighted experiments is the decay of fullerenes via sequential loss of  $C_2$  whilst retaining their closed-cage structure:



where  $n$  is the number of carbon atoms in the original fullerene. This decay mechanism is also known as “fission”, “evaporation” and “shrink-wrapping”, and has been demonstrated to occur in a variety of different experiments, including photofragmentation, electron impact ionisation, molecular and surface-induced collisions. In fact, the “shrink-wrapping” mechanism has been recently captured via TEM-STM microscopy showing the successive  $C_2$  loss and shrinkage of a giant fullerene  $C_{1300}$  trapped inside a cavity of a multi-walled nanotube heated to high temperatures [31].

The fragmentation energy of equation 5.1 has been referred to as the “ $C_2$

binding energy”, the “evaporation energy” and the “dissociation energy”, and is simply determined as the difference between the energies of the products and reactants. The  $C_2$  fragmentation energy has now been accepted to be in the range of 11-12 eV after significant debate between the discrepancy of the value found in experiments and theoretical work. In contrast to the considerable work done in this direction with regards to  $C_{60}$ , not much is known about the fragmentation energy of larger fullerenes. Recent theoretical and experimental work has evaluated the  $C_2$  binding energy of  $C_{80}$  between 8.7-9.0 eV—3 eV lower than neutral  $C_{60}$ .

Aside from  $C_2$  loss, fullerenes can also decay through thermionic emission (also known as delayed ionisation), blackbody radiation (or radiative cooling) and through fusion or multifragmentation of the cage into a number of small fragments (cage shattering or cleavage). In this section, we will focus mainly on  $C_2$  evaporation and multifragmentation of fullerenes.

#### PHASE TRANSFORMATION AND MULTIFRAGMENTATION

In Chapter 4, we have presented the fragmentation dynamics of  $C_{60}$  where the  $C_{60}$  was shown to transform into metastable tube, bowl and graphene-like structures before multifragmentation to a gas phase. Similar behaviour was also found for fullerenes  $C_{32}$  and  $C_{70}$ , shown in Fig. 5.7, where  $C_{32}$  transforms into a graphene, and  $C_{70}$  unfurls into a bowl-like structure from which it becomes a graphene sheet—much like  $C_{60}$ . Simultaneous with these transformations is the evaporation of a number of  $C_2$  molecules from the carbon structure before rapid and successive  $C_2$  loss leading to total fragmentation.

In contrast, fullerenes  $C_{80}$  to  $C_{540}$  do not display such transformations. Instead these fullerenes only initially evaporate  $C_2$  molecules (or C atoms), alongside rapid bond breaking and flipping, leading to an almost amorphous-like carbon structure, from which multifragmentation takes place. This can be seen in Fig. 5.8 for  $C_{90}$ ,  $C_{240}$  and  $C_{540}$ .

To further understand this difference in the fragmentation pathway, Table 5.1 shows the difference in the energies between the optimised fullerene and graphene structures of  $C_{32}$  to  $C_{240}$ . Two things immediately stand out.

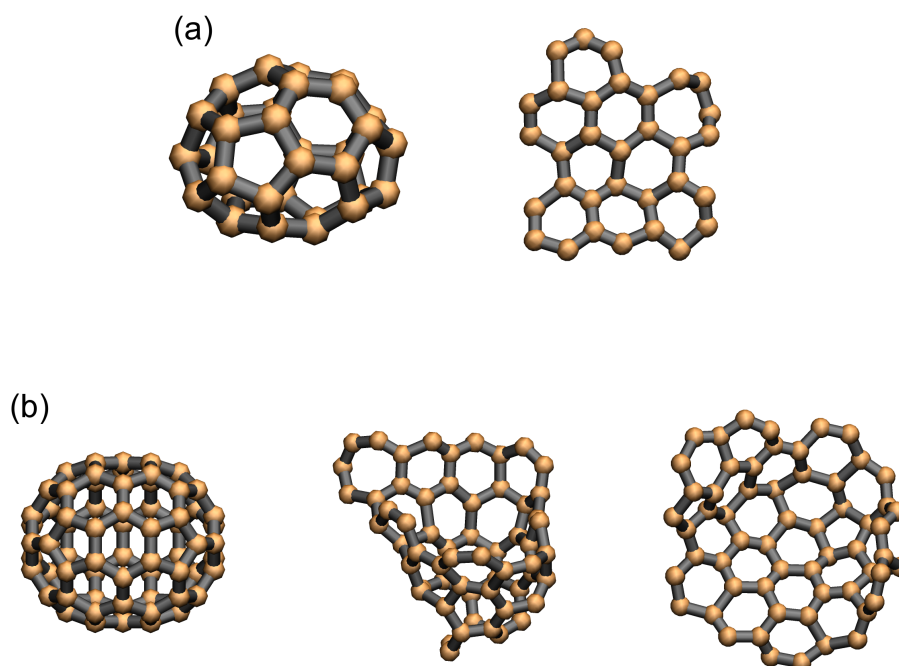


Figure 5.7: Transformation to graphene prior to multifragmentation for (a)  $C_{32}$  and (b)  $C_{70}$ .

Firstly, the optimised graphene structure of  $C_{32}$  is energetically competitive with the  $C_{32}$  fullerene. This result is in line with the fact that stable fullerene structures are known to begin from  $C_{32}$ ; while the Pentagon Road mechanism surmises the formation of fullerenes from graphene-like sheets that fold into “open graphitic cups”. Secondly, the energetic barrier between the graphene and fullerene structures of  $C_{80}$  is less than that for  $C_{70}$ , although from the molecular dynamics simulations,  $C_{80}$  does *not* show transformation to graphene prior to multifragmentation, while  $C_{70}$  does. This however, can be attributed to entropic factors. With increasing cluster size, the entropy of the system would lead to less likely formation of ordered graphene structures, compared to “amorphous” carbon-like structures which were seen in Fig. 5.8 before multifragmentation to carbon gas. Nevertheless, it should be noted that the energetic barrier between the graphene and fullerene structure of  $C_{80}$

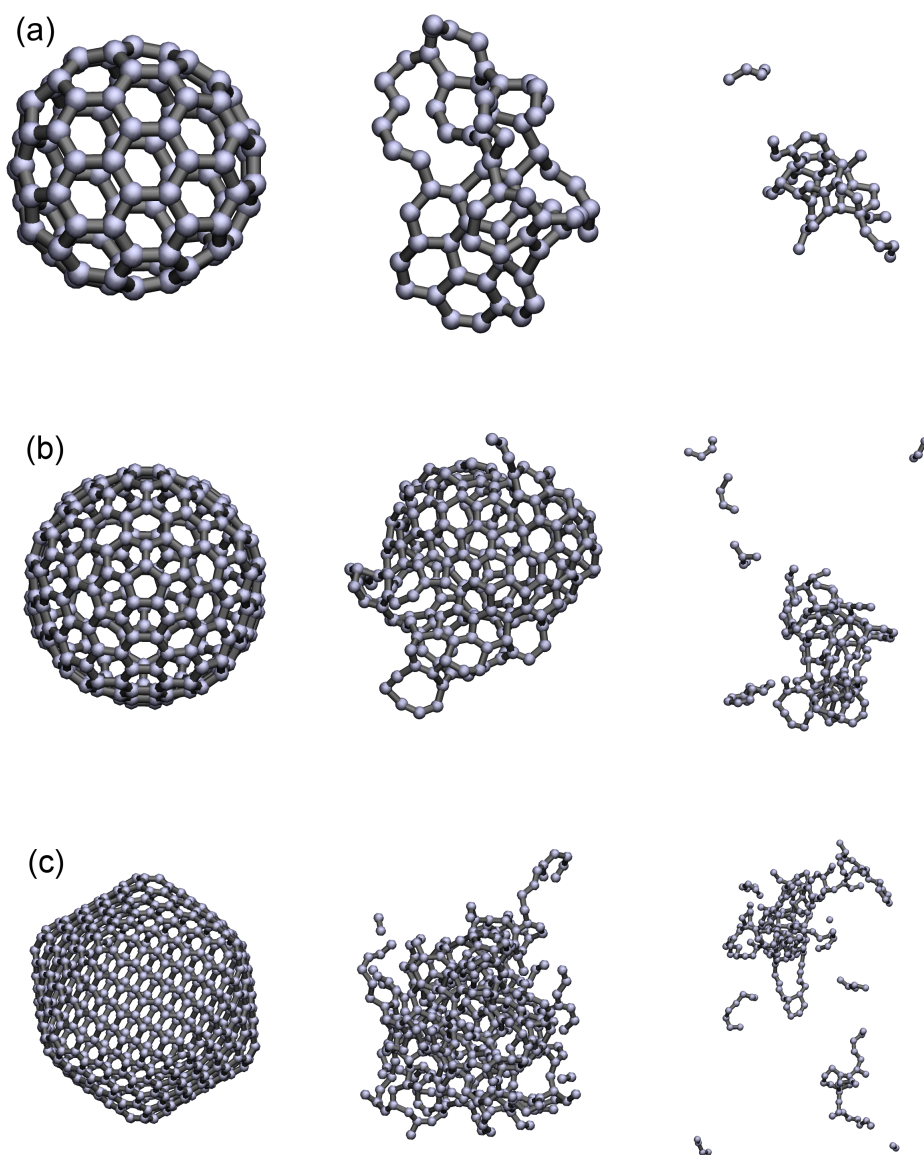


Figure 5.8: Fullerenes larger than  $C_{70}$  do not show transformation to graphene, but show rapid multifragmentation, as shown for (a)  $C_{90}$ , (b)  $C_{240}$  and (c)  $C_{540}$ .

Table 5.1: Energetics of fullerene and graphene structures

Size	Fuller. (eV/atom)	Graph. (eV/atom)	G-F (eV/atom)	G-F (eV)
32	-6.227	-6.241	-0.013	-0.431
60	-6.728	-6.613	0.115	6.832
70	-6.803	-6.659	0.144	10.067
80	-6.859	-6.752	0.107	8.581
90	-6.896	-6.771	0.125	11.281
240	-7.181	-6.950	0.231	55.440

is about 8-9 eV—the range of the C<sub>2</sub> fragmentation energy. While the energy barrier for C<sub>60</sub> is on the range of 7 eV, less than its known C<sub>2</sub> evaporation energy of 11-12 eV. It is therefore possible that there is a competition between the entropy, the C<sub>2</sub> binding energy associated with successive C<sub>2</sub> loss leading to multifragmentation and transformation to metastable graphene state for the fullerene molecules in a canonical ensemble, although this point will need further investigation.

In addition to this, the difference in the behaviour of the “small” (C<sub>32</sub>, C<sub>60</sub> and C<sub>70</sub>) and “big” (C<sub>80</sub>, C<sub>90</sub>, C<sub>180</sub>, C<sub>240</sub> and C<sub>540</sub>) fullerenes is also demonstrated in the energy profiles of these structures. The time-dependent instantaneous total energy plot of C<sub>32</sub>, C<sub>70</sub> and C<sub>240</sub> is shown in Fig. 5.9. For the former two fullerenes, the energy profiles display “steps” in the energy prior to the jump in energy. These energetic “steps” signal a phase transformation to metastable bowl or graphene structures while the jump in the energy indicates total fragmentation to carbon vapour. However, such energy “steps” are not prominent in the profile of C<sub>240</sub>.

It should be noted however, that Fig. 5.9 displays results from a longer 500 ns simulation of C<sub>32</sub>, C<sub>70</sub> and C<sub>240</sub>. As discussed in the previous chapter, a longer simulation shifts the phase transition temperature to lower temperatures and causes the caloric curve to become sharper. Hence, the tempera-

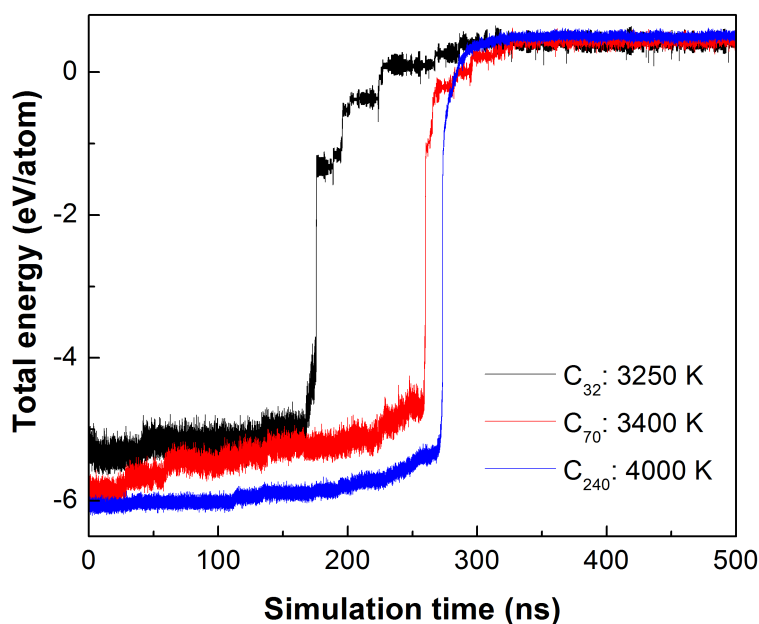


Figure 5.9: Time-dependent total energy per atom of  $C_{32}$ ,  $C_{70}$  and  $C_{240}$ . Steps in the energy profiles of  $C_{32}$  and  $C_{70}$  can be seen, similar to those found for  $C_{60}$  in Chapter 4.

tures shown in Fig. 5.9 correspond to the shifted phase transition temperature for a simulation length 500 ns. For  $C_{70}$  and  $C_{240}$ , the difference in the phase transition temperatures between the shorter 50 ns run and the longer 500 ns run is about 300-400 K, while for  $C_{32}$  it is less than 100 K. This can be attributed to the size-effect of the structures, with bigger fullerenes needing a similarly longer simulation run.

## 5.2 NANOCARBON STRUCTURES

The discovery of fullerenes and its subsequent method of mass production marked the onset of a revolution in the field of nanoscience. While fullerenes remain one of the most popular objects of investigations, carbon nanotubes—and currently graphene—are leading the wave of intensive research in this field.

Carbon nanotubes were discovered shortly after fullerenes, in 1991, from



the soot deposit of carbon-arc discharge. These nanotubes are nano-sized in diameter, but with lengths that may grow up to centimetres—such that their length-to-diameter ratio may exceed  $10^7$ . Nanotubes may grow as a monolayer, also known as single-wall nanotubes (SWNT), or as nested multi-layers, known as multi-walled nanotubes (MWNT). Much like fullerenes, nanotubes are generated by both arc-discharge and laser ablation techniques. However, these techniques are resource-intensive, thus much of the current method of nanotube synthesis is done through chemical vapour deposition. Nanotubes are used in a variety of applications, including catalysis [173, 174], filtration [175, 176], increasing the tensile strength of materials [177, 178], as capacitors [179–181] and as thermally and electrically-conductive material [182, 183].

Carbon onions, identified [104] in 1992, are spherical or polyhedral structures made up of concentric shells—in other words, multi-walled fullerenes. They are formed by high-energy electron irradiation of carbon soot [104, 184], but are known to be unstable at room temperature [185]. Spherical and quasi-spherical carbon onions are known to have many defects and dangling bonds [186]. These defects are also thought to be the presence of heptagonal and additional pentagonal rings [187]. When carbon onions are subjected to high heat and/or high electron or ion irradiation, the core of the carbon onion can be transformed into nanodiamonds [188–191], due to extremely high pressures (higher than 20 GPa) in which the carbon onions resemble nanoscopic pressure cells [188] for diamond formation. In fact, the reverse transformation of nanodiamond to carbon onion has also been demonstrated both computationally [192–195] and experimentally [186, 196], where it was also shown that the generated carbon onions can be re-transformed back into nanodiamonds by heating at 500°C in air [186].

Since it was first isolated in 2004 [105, 197], graphene has been one of the most intensively researched material amongst the nanocarbon structures. Graphene is a single layer of carbon atoms arranged in a hexagonal network of  $sp^2$  bonds. It can be easily produced by the mechanical exfoliation of highly-ordered graphite, although such technique produces quite uneven films and is both time-consuming and labour-intensive. A more scaleable method of

production involves growing graphene epitaxially [198, 199] on a SiC wafer at high temperatures, via various chemical methods [200–202] including chemical vapour deposition [203–206]. Similar to nanotubes, graphene also possesses remarkable mechanical and conductive properties, with applications in liquid crystal display [207] and solar cells [208] and is ideally hoped to be used as transistors to replace silicon in integrated circuits.

We now consider five phases of nanocarbon when  $N$ , the number of carbon atoms, is 240. These phases are the fullerene, nanotube, buckyball, graphene and carbon onion structures that are presented in Fig. 5.10 alongside their corresponding optimised total energies per atom [2]. The nanotube analysed in this work has a chirality of (10,10) and is uncapped, while the carbon onion is a “double-walled” fullerene consisting of a  $C_{60}$  encapsulated by a  $C_{180}$  to form  $C_{60}@C_{180}$ . The buckyball structure is made up of a  $C_{540}$  fullerene that has had 300 atoms removed from its cap. As was done previously, all structures were optimised prior to conducting molecular dynamics simulations using the Tersoff potential.

For the remaining of the chapter, the cluster of 240 carbon atoms whose structure may be that of a fullerene, a nanotube, a buckyball, a carbon onion or a graphene, is collectively referred as  $C_{240}$ . The fullerene structure is exclusively annotated as  $C_{240}$ , while the nanotube, buckyball and graphene structures are referred to as  $C_{240}^n$ ,  $C_{240}^b$  and  $C_{240}^g$  respectively. The carbon onion is simply denoted as  $C_{60}@C_{180}$ .

### 5.2.1 PHASE TRANSITIONS OF $C_{240}$

We present in Fig. 5.11 the caloric curves and respective heat capacities of the  $C_{240}$  structures. As can be seen, the  $C_{240}$  fullerene is the most thermodynamically stable structure, followed by the carbon onion, the buckyball and graphene. The uncapped (10,10) nanotube is found to be least thermodynamically-stable structure. The thermodynamical stability, however, does not concur with the binding energies (shown in Fig. 5.10), of the structures in which, for example, the nanotube  $C_{240}^n$  is more energetically favourable than buckyball  $C_{240}^b$ . However, in terms of heat capacity,

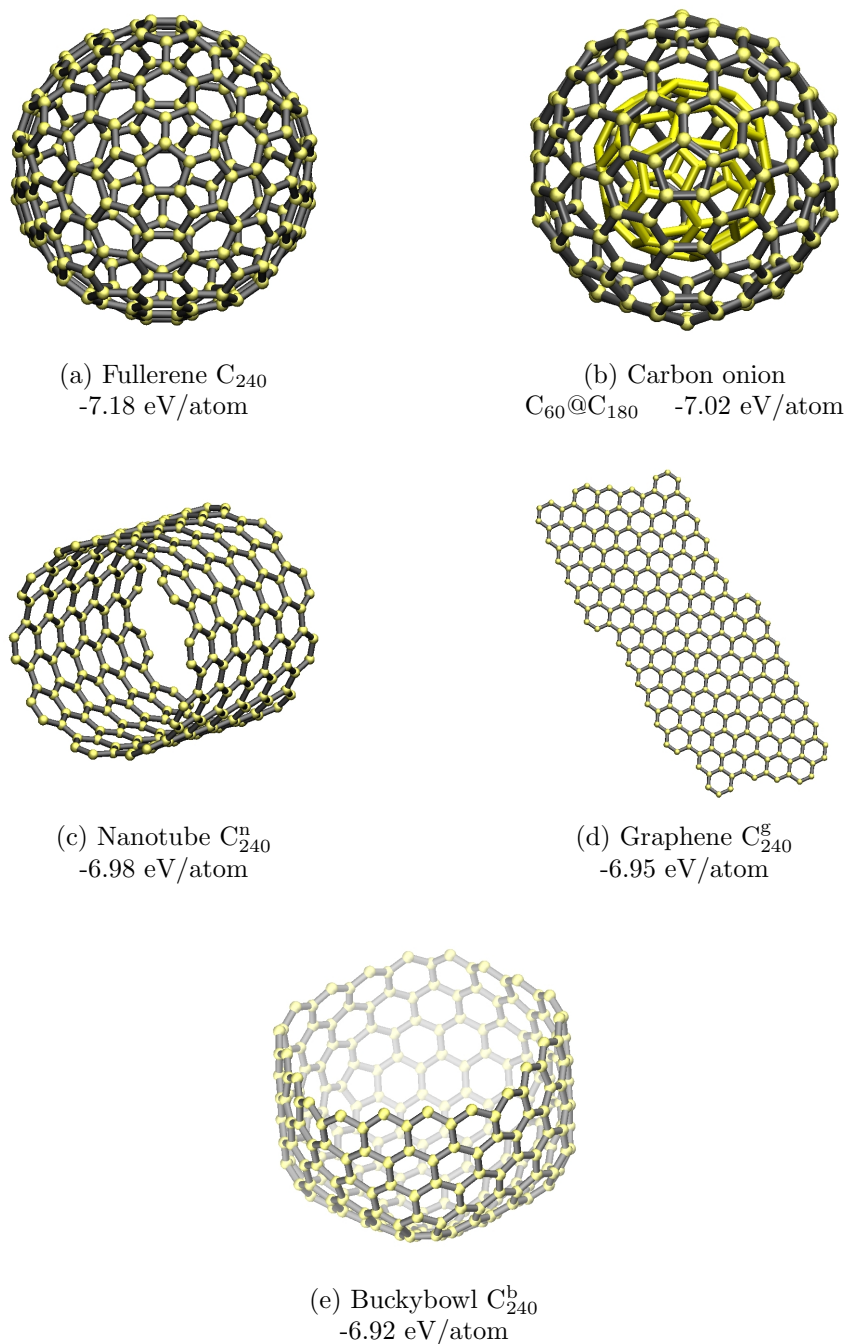


Figure 5.10: The  $C_{240}$  nanocarbon phases considered in this work: (a)  $C_{240}$  fullerene, (b)  $C_{60}@C_{180}$  carbon onion, (c) uncapped  $C_{240}^n$  nanotube with chirality of (10,10), (d)  $C_{240}^g$  graphene sheet and (e)  $C_{240}^b$  buckybowl.

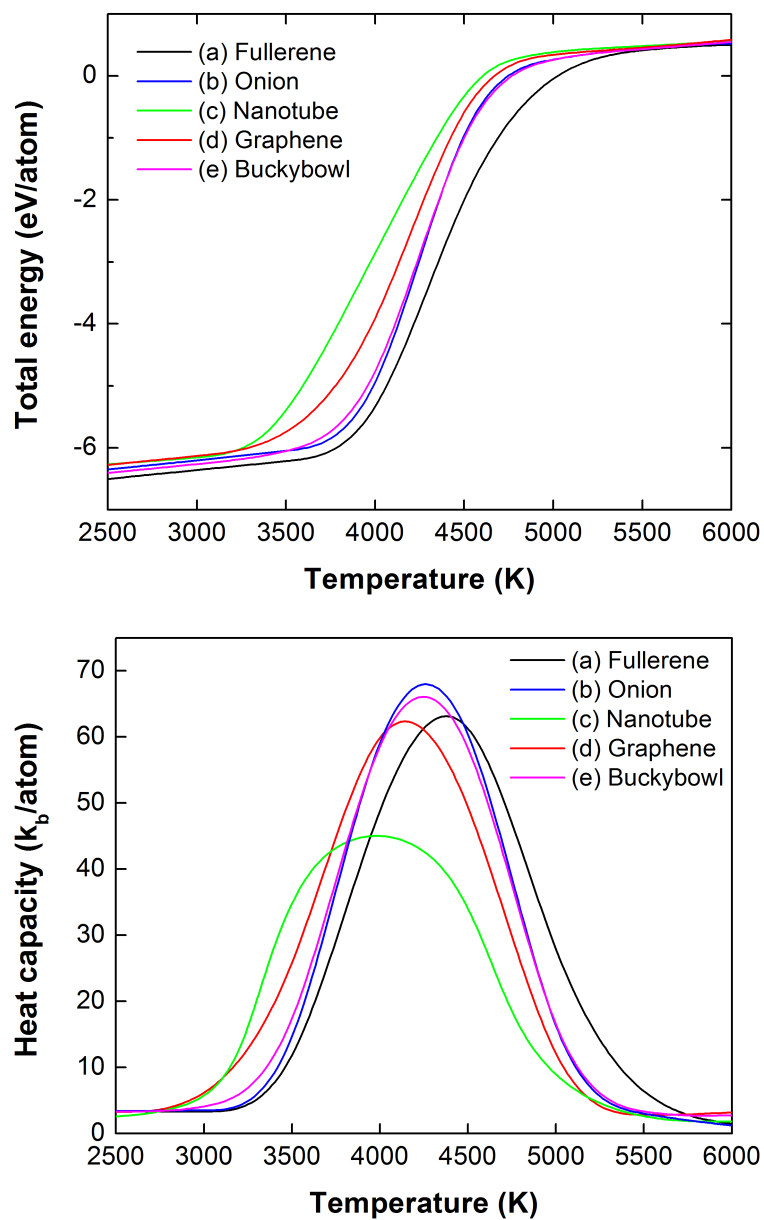


Figure 5.11: Caloric curves (left) and respective heat capacities (right) for the  $C_{240}$  structures considered in this work.

the carbon onion and buckyball structures have higher heat capacities per atom at the phase transition temperature; while the values for graphene and fullerene are almost equivalent. As noted previously, these curves correspond to 50 ns simulations, thus the caloric curves presented are “smooth” and not sharp as in the 500 ns and 1000 ns simulations.

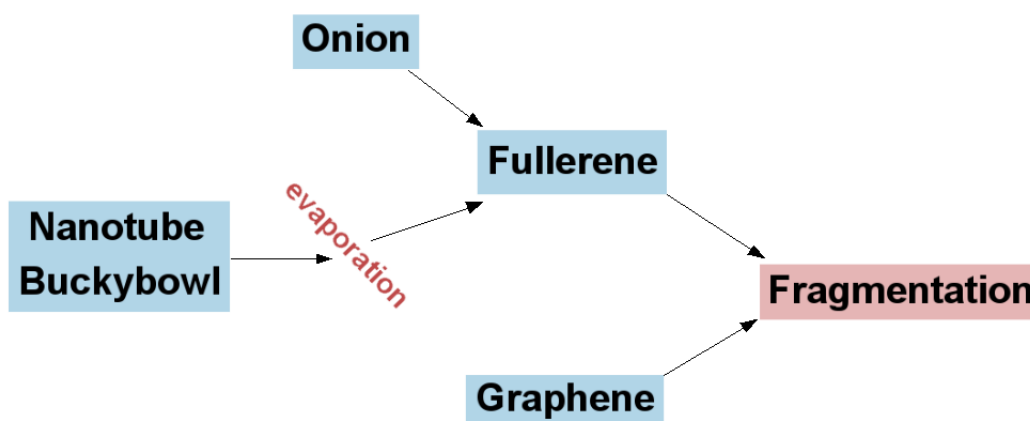


Figure 5.12: Transformation of the  $C_{60}@C_{180}$  to a  $C_{240}$  fullerene before fragmentation

However in the course of the molecular dynamics simulations, we have observed the following transformations of the nanocarbon phases before the onset of fragmentation. In Fig. 5.12 we demonstrate the direction of the fragmentation process. Fullerene and graphene maintain their structures before quick successive evaporation of C or  $C_2$  units leading to multifragmentation. On the other hand, the molecular dynamics simulations have demonstrated that the carbon onion, buckyball and nanotube structures undergo a different fragmentation route compared to the fullerene and graphene. The  $C_{60}$  encapsulated in the  $C_{180}$  undergoes bond breaking and fragmentation, where the fragmented atoms are incorporated into the larger  $C_{180}$  shell, shown in Fig. 5.13, and migrates through the  $C_{180}$  via Stone-Wales transformation, until the entire  $C_{60}$  molecule is consumed, creating a  $C_{240}$  fullerene. Only from this fullerene structure does multifragmentation to carbon gas occurs.

On the other hand, the nanotube and buckyball structures begin their

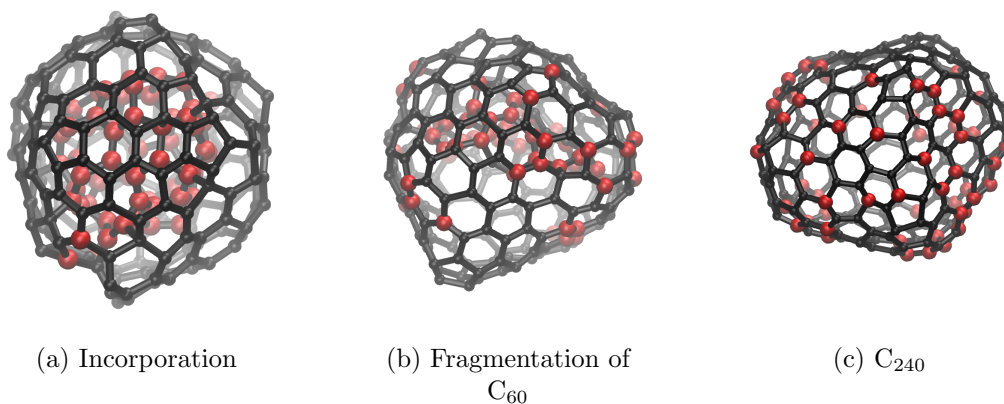


Figure 5.13: The transformation of  $C_{60}@C_{180}$  to  $C_{240}$  begins with (a) incorporation of C atoms from  $C_{60}$  into the  $C_{180}$  shell, followed by (b) the fragmentation of the  $C_{60}$  cage as its atoms fuel the growth of  $C_{180}$  to form the final  $C_{240}$  structure in (c).

onset to fragmentation by evaporation of C or  $C_2$  units. However, unlike fullerene and graphene that disintegrate due rapid and successive evaporation, these structures transform into cage-like structures, resembling deformed and elongated fullerenes. Again, both systems remain in this fullerene-like state. The transformation of these structures to a  $C_{240}$  fullerene may be expected as the binding energy of  $C_{240}$  shows that it is the most energetically favourable structure for 240 carbon atoms. Moreover, no transition from the fullerene, buckybowl, nanotube and carbon onion structures to graphene were found. Thus, the multifragmentation of graphene to carbon vapour can be surmised to follow a different fragmentation pathway.

### 5.3 CHAPTER SUMMARY

In this chapter, we have explored the phase transition properties and stabilities of fullerenes  $C_{32}$  to  $C_{540}$  and nanocarbon clusters of 240 carbon atoms. Analysis of the binding energies and the caloric curves of the fullerenes show that fullerene stability should increase with size. However, this is in contrary to experimental findings, in particular the significant abundance of  $C_{60}$  to

larger fullerenes in fullerene-generating experiments, such as arc-discharge. Thus, the special stability of  $C_{60}$  may be the result of kinetic factors and/or specific formation mechanisms.

We have also demonstrated that “small” fullerenes ( $C_{32}$ ,  $C_{70}$  and  $C_{60}$ ) show a transformation to a graphene phase prior to multifragmentation to carbon vapour. This behaviour, however, was not observed for “big” fullerenes ( $C_{80}$  to  $C_{540}$ ), where rapid multifragmentation is seen to occur from successive evaporation of  $C_2$  or  $C$  atoms. The absence of a graphene phase in the fragmentation pathway can be attributed to entropic factors related to increasing size of the system. Additionally, we have also investigated the energetic barrier between the fullerene and graphene phases. Results indicate that the graphene phase is competitive with the fullerene phase for  $C_{32}$ ; while the energetic barrier for  $C_{60}$  and  $C_{80}$  are less or close to the range of energies associated with the  $C_2$  binding energy.

We then discussed the phase transition properties of a cluster of 240 carbon atoms in the form of a fullerene, graphene, buckybowll, an uncapped (10,10) nanotube fragment and a  $C_{60}@C_{180}$  carbon onion. Results of the molecular dynamics simulation show that the fullerene structure is the most thermodynamically stable, while the nanotube is the least. However, the carbon onion, nanotube and buckybowll structure all transform into a fullerene prior to multifragmentation into a carbon gas. This can be attributed to the fact that the  $C_{240}$  fullerene structure is the most energetically favourable structure (with the largest binding energy). However, no transformation of graphene to any other phases were observed. Thus, graphene can be surmised to follow a different fragmentation pathway.





## CHAPTER 6

# INTERACTION OF CARBON WITH A METAL CLUSTER

Carbon nanotubes are now commonly synthesised using chemical vapour deposition (CVD). In this method, a substrate is prepared with a layer of catalytic metal clusters, often nickel, cobalt or iron. The substrate is then heated to temperatures of 500°C or higher. To initiate the growth of nanotubes, a carbon-based feedstock gas is pumped into the CVD chamber. The interaction of the feedstock gas and the catalyst at high temperatures leads to the growth of nanotubes on the metal cluster. However, despite the widespread use of this technique, the growth mechanism of this process is still not yet well understood [110].

In addition to this, carbon nanotubes are also known to be synthesised using arc-discharge and laser vapourisation techniques when the graphite target is mixed with some metal particles. Furthermore, the production of higher fullerenes in arc-discharge was also shown to increase when the graphite rods were doped with boron [163].

In this chapter, the interaction of carbon with a metal nanocluster, Ni<sub>147</sub>, is investigated. Specifically, we investigate how the melting temperature of the nickel cluster is affected by the presence of a carbon atom or a C<sub>2</sub> molecule. We also investigate the diffusion of the carbon impurity within the nickel nanocluster. This question is relevant because, during the nanotube growth process, it is thought that the carbon atoms may migrate into the

metal nanocluster, causing “poisoning” of the catalytic particle and halting the growth process of the nanotubes. Thus, knowledge of the specific role of a carbon impurity in the Ni catalytic nanoparticle may ascertain whether the carbon nanotube structure and its growth kinetics can be controlled. Moreover, understanding how the metal nanocluster reacts with the carbon impurity will help shed light on controlling the production yields of higher fullerenes.

## 6.1 PURE AND CARBON-DOPED CLUSTERS

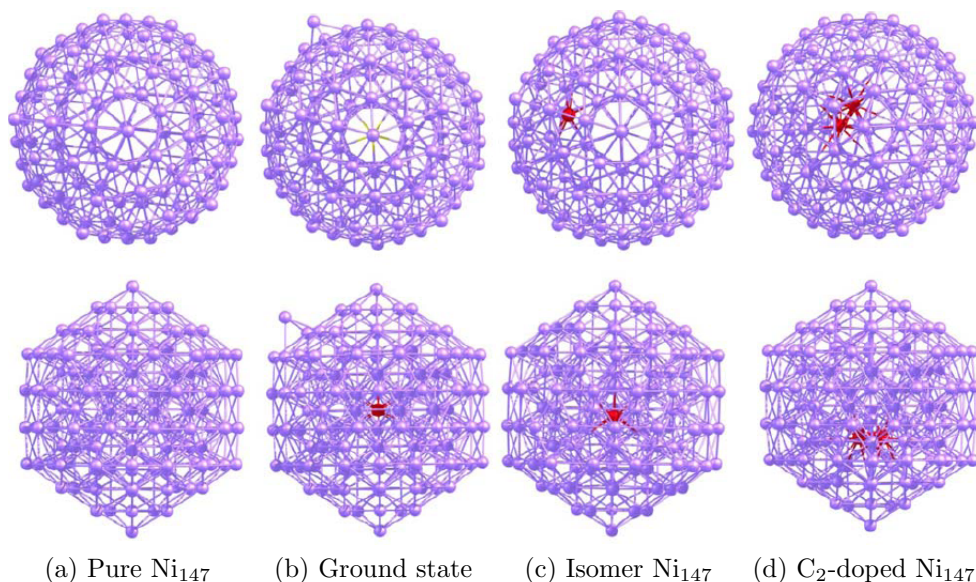


Figure 6.1: The four nickel structure that are investigated, (a) the optimised structure of a pure  $\text{Ni}_{147}$  cluster; (b) the *ground* state structure of the C-doped  $\text{Ni}_{147}$  cluster; (c) the *isomer* state structure of the C-doped  $\text{Ni}_{147}$  cluster; (d) the optimised structure of the  $\text{C}_2$ -doped  $\text{Ni}_{147}$  cluster.

In Fig. 6.1, we present four structural configurations of  $\text{Ni}_{147}$  nickel and carbon-doped nickel clusters. In agreement with previous calculations, we have found that the optimised structure of the pure  $\text{Ni}_{147}$  cluster is a perfect icosahedron[209, 210]—a motif that is prevalent in small nickel clusters, par-

ticularly around the sizes of a complete Mackay icosahedra [126, 210–212]. For the C-doped  $\text{Ni}_{147}$  cluster, Fig. 6.1b, we have found that the ground state of the structure has a similar icosahedral motif, although one Ni atom protrudes out of the icosahedral shell, displaced by the C dopant which now resides in the core of the cluster. The energetically closest isomer of the C-doped  $\text{Ni}_{147}$  cluster is a deformed icosahedron, Fig. 6.1c, in which the C dopant is located in the vicinity of the cluster core. The impurity atom causes a local distortion between the first and second closed shells of the icosahedron, leading to a difference in the binding energy of 0.002 eV between the isomer state and the ground state structure of C-doped  $\text{Ni}_{147}$ . Additionally, this isomer state is metastable since a transformation from this structure to the ground state necessitates overcoming an energy barrier. Instead of the ground state of the C-doped  $\text{Ni}_{147}$  nickel cluster (C in the core), the following case study will consider the metastable isomer (C in between the first and second shells) instead. The motivation for this comes from the fact that the isomer state is more likely to be found in nanotube growth experiments, due to successive migration of the C atom from the surface of the nickel catalyst towards its centre. The final cluster considered in this case study, shown in Fig. 6.1d, is the optimised  $\text{C}_2$ -doped  $\text{Ni}_{147}$  cluster.

All these structures were optimised using an efficient scheme of global optimisation, known as the Cluster Fusion Algorithm [213–215]. Using these structures, we conducted molecular dynamics simulations based on the Sutton-Chen, Morse and Tersoff potentials to describe the Ni-Ni, Ni-C and C-C bondings respectively. The Sutton-Chen potential [121] is a many-body potential that has been shown to reproduce bulk and surface properties of transition metals and their alloys with sufficient accuracy (see, e.g., Refs. [122–126] and references therein).

For the Ni-C interaction, we have used a Morse potential whose parameters were obtained by fitting the results of an *ab initio* density-functional calculation of the Ni-C interaction [127–129]. The form of the Sutton-Chen and Morse potentials, as well as further discussion regarding the potential parameters was already given in Chapter 2.

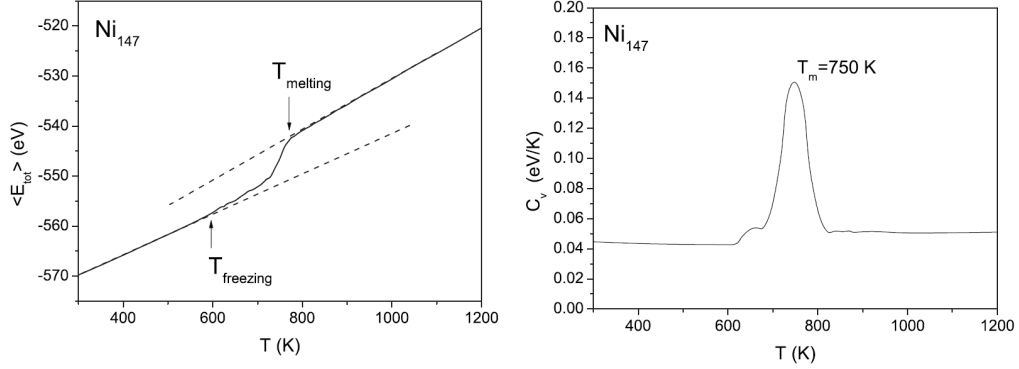
6.1.1 PURE  $\text{Ni}_{147}$  CLUSTERS

Figure 6.2: Caloric curve (left) and heat capacity (right) of the pure  $\text{Ni}_{147}$  cluster. Temperatures  $T < T_{\text{freeze}}$  and  $T > T_{\text{melt}}$  correspond respectively to the completely frozen and molten states. The melting temperature of the cluster,  $T_m = 750$  K, is given by the maximum of the heat capacity.

In Fig. 6.2, we present the caloric curve and heat capacity plots of the pure  $\text{Ni}_{147}$  cluster. The heat capacity has been derived from the caloric curve using  $C_v = (\partial E / \partial T)_v$ . The change in the gradient of the caloric curve indicates the occurrence of a thermal phase transition, of which the height of the jump in the vicinity of the phase transition point gives an estimate of the latent heat, *i.e.* the energy which associated with the destruction of the ordered lattice.

For the pure  $\text{Ni}_{147}$  cluster, the onset of the melting transition occurs from  $T_{\text{freeze}} \approx 600$  K, before which the cluster is completely frozen. While the cluster can be considered to be molten by  $T_{\text{melt}} > 800$  K. The intermediate interval  $T_{\text{freezing}} < T < T_{\text{melting}}$  corresponds to the mixed state where both solid and the liquid phases coexist. As have been discussed in the previous chapter, such a phase coexistence is a typical behaviour of finite systems, in comparison to the abrupt and discontinuous change in the caloric curve when bulk matter melts.

The peak of the temperature-dependent heat capacity curve of Fig. 6.2 gives the melting temperature of the pure  $\text{Ni}_{147}$  cluster,  $T_m = 750$  K. This melting temperature is considerably smaller than the melting temperature

for the bulk nickel  $T_m^{bulk} = 1728$  K[216], due to a substantial increase in the relative number of weakly-bounded atoms on the surface of the cluster compared to the bulk.

The heat capacity curve of Fig. 6.2 displays an additional maximum at  $T \approx 660$  K, suggesting a stepwise melting process. This small peak corresponds to a “pre-melted” state, where the cluster surface melts while the core of the cluster remains frozen—an example of static phase coexistence, or phase separation. The exact delimitation of the two phases is relative but can be defined from the difference in mobility of atoms taken from the cluster surface and its core. However, it should be noted that this occurs *before* the phase transition temperature of 750 K, where (as we see below) dynamic phase coexistence can be observed.

Figures 6.3(a), 6.3(b), and 6.3(c) present the time dependence of the instantaneous values of the total energy (the energy profiles) calculated for the Ni<sub>147</sub> cluster at the temperatures 600 K, 750 K, and 800 K, respectively. The total simulation time is 10 ns.

As can be seen, the instantaneous total energy values oscillate about their time-averaged values in Fig. 6.3(a) and (c), corresponding to  $T = 600$  K and  $T = 800$  K respectively. At either temperature, the pure Ni<sub>147</sub> cluster is either completely frozen (600 K) or completely molten (800 K).

At the phase transition temperature of 750 K however, the energy profile shows successive oscillations between the two time-averaged values corresponding to the frozen and molten. As such, Fig. 6.3(b) shows that the Ni<sub>147</sub> cluster spends part of its time in the frozen state and part of its time in the molten state—rapidly oscillating between both states. Such a behaviour indicates dynamic phase coexistence, typical of many finite systems [217, 218].

Note that, in the interval of temperatures  $T_{freezing} < T < T_{melting}$ , it is necessary to perform the molecular dynamics simulations for a relatively long time (on the order of 10 ns) to achieve time independence of the averaged total energy  $\langle E_{tot} \rangle$  of the system. The average life-time of the system in the frozen and the molten states depends upon the temperature of the cluster, resulting in a smooth change of the  $\langle E_{tot} \rangle$  from the frozen to the molten state as a function of temperature. Therefore, Fig. 6.3(b) clearly demonstrates

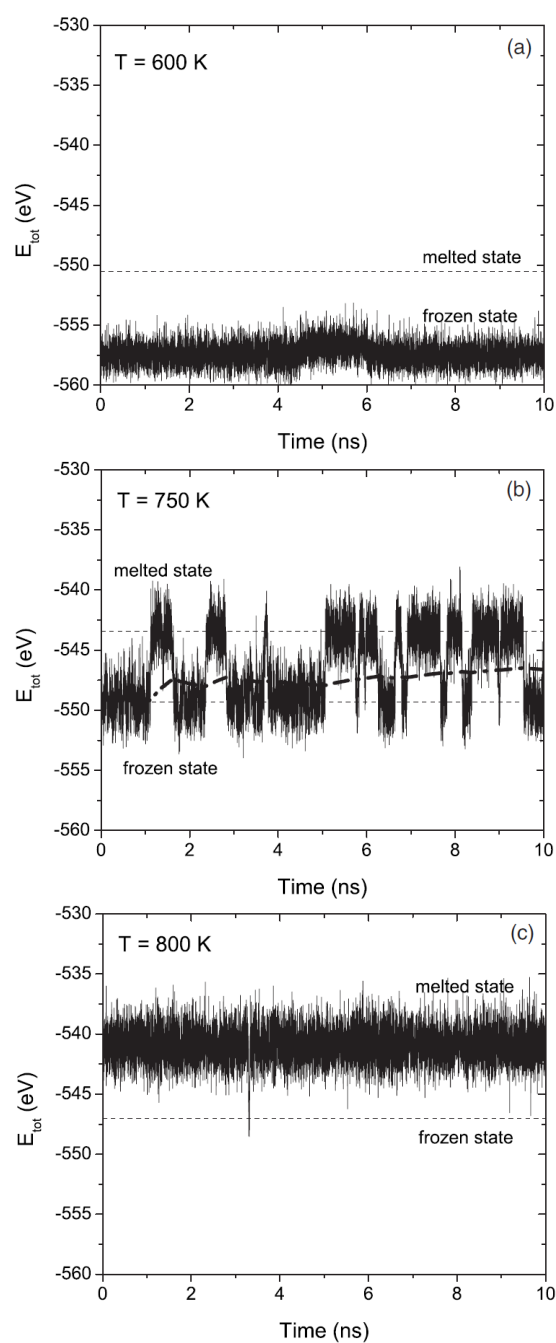


Figure 6.3: Time dependence of the instantaneous values of the total energy calculated for the  $\text{Ni}_{147}$  cluster: (a)  $T = 600$  K, frozen state; (b)  $T = 750$  K, phase transition; (c)  $T = 800$  K, molten state. The dashed-dotted lines demonstrate the time-averaged total energy of the system.

dynamic coexistence of two thermodynamic phases at the phase transition temperature.

### 6.1.2 CARBON-DOPED $\text{Ni}_{147}$ CLUSTERS

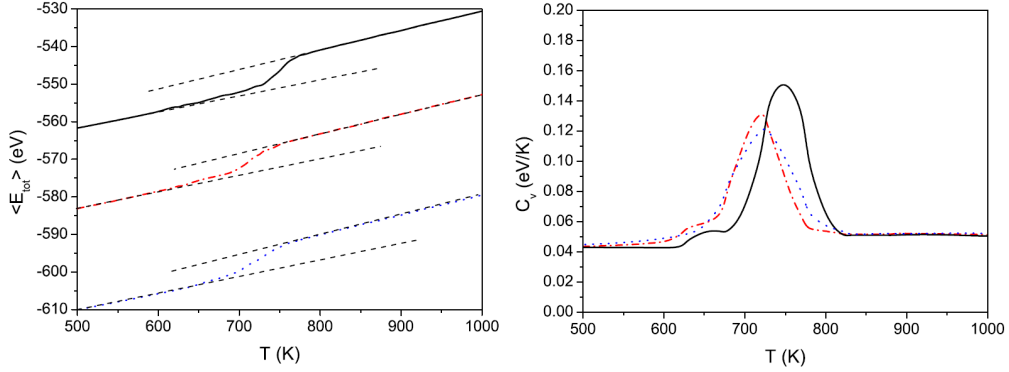


Figure 6.4: Caloric curves (left) and heat capacities (right) of the pure  $\text{Ni}_{147}$  cluster (solid line), the C-doped  $\text{Ni}_{147}$  cluster (dashed-dotted line) and the  $\text{C}_2$ -doped  $\text{Ni}_{147}$  cluster (dotted line). The melting temperatures are  $T_m = 750$  K,  $720$  K and  $725$  K for the  $\text{Ni}_{147}$ , C-doped  $\text{Ni}_{147}$  and  $\text{C}_2$ -doped  $\text{Ni}_{147}$  clusters respectively.

By introducing an impurity (C or  $\text{C}_2$ ) into the pure  $\text{Ni}_{147}$  cluster, the icosahedral lattice of the original  $\text{Ni}_{147}$  cluster becomes deformed, leading to altered thermodynamic properties—which are the focus of this section. Note that the C-doped  $\text{Ni}_{147}$  cluster under investigation is the isomer state with the carbon impurity located between the first and second icosahedral shells.

In Fig. 6.4, we present the caloric curves and heat capacities of the pure  $\text{Ni}_{147}$  cluster, the C-doped  $\text{Ni}_{147}$  cluster and the  $\text{C}_2$ -doped  $\text{Ni}_{147}$  cluster. From the heat capacities, the derived phase transition temperatures for the doped clusters are:  $T_m = 720$  K for C-doped  $\text{Ni}_{147}$  and  $T_m = 725$  K for  $\text{C}_2$ -doped  $\text{Ni}_{147}$ , in comparison to  $T_m = 750$  K for the pure  $\text{Ni}_{147}$  cluster. Hence, doping of the  $\text{Ni}_{147}$  cluster with a single C impurity reduces its melting temperature by 30 K.

The decrease in the melting temperature of the doped clusters from the pure  $\text{Ni}_{147}$  cluster, can be explained as a result of the local distortions of the

cluster's icosahedral structure near the impurity. The C atom introduces a strain in the cluster lattice which decreases the stability of the cluster thus, its melting temperature. Note that the C<sub>2</sub> atom in the C<sub>2</sub>-doped Ni<sub>147</sub> cluster does not dissociate in the course of the simulation. Thus the C<sub>2</sub> impurity can be considered as a single dopant with simply a larger radius. In general, Fig. 6.4 shows that the doping of a cluster consisting of hundreds of atoms by merely a single impurity results in a significant change of its melting temperature.

As the carbon impurity in C-doped Ni<sub>147</sub> is located between the first and second icosahedral shells, it does not significantly influence the surface melting of the cluster. This can be seen from the heat capacity plot in Fig. 6.4, where the onset of the pre-melting peak still occurs from 600 K, much like in the pure Ni<sub>147</sub> cluster.

#### MELTING TRANSITIONS

Melting transitions can also be recognised from the analysis of the trajectories of individual atoms and their diffusion in the volume of the cluster. The melting transition occurs when atoms begin their Brownian motion instead of the thermal vibrations around their equilibrium positions in the ordered cluster's lattice. Such a transition can be seen as a step in the temperature dependence of the diffusion coefficient. The diffusion coefficient of the atom  $i$  in a media is defined as (see, e.g., Refs. [217, 219]):

$$D_i = \frac{1}{6} \frac{d}{dt} \langle r_i^2(t) \rangle, \quad (6.1)$$

where  $\langle r_i^2(t) \rangle$  is the mean-square displacement averaged along the atom's trajectory

$$\langle r_i^2(t) \rangle = \frac{1}{n_t} \sum_{j=1}^{n_t} (\mathbf{R}_i(t_{0j} + t) - \mathbf{R}_i(t_{0j}))^2. \quad (6.2)$$

Here  $\mathbf{R}_i(t)$  is a radius vector of an atom  $i$  at the time  $t$ , and  $n_t$  is the number of time origins,  $t_{0j}$ , considered along the trajectory. Equation (6.1) is valid for the simulation time smaller than the time required for a particle to migrate



across the diameter of the cluster.

Figure 6.5 demonstrates the two-dimensional projection of trajectories calculated for the Ni atom in the center of the C-doped Ni<sub>147</sub> cluster (filled dots), the Ni atom from the vertex of the cluster surface (stars) and the C impurity (open dots). The temperature of the cluster ranges from 400 K to 800 K, as is shown in Fig. 6.5. The output time step is 1 ps with the total simulation time of 2 ns.

As seen in Fig. 6.5, for a low temperature,  $T = 400$  K, all selected atoms in the C-doped Ni<sub>147</sub> cluster vibrate around their equilibrium positions. At this temperature, the cluster is frozen—as per the analysis of the caloric curve and the heat capacity calculated for the C-doped Ni<sub>147</sub> cluster, see Figs. 6.4 and 6.4).

It has been discussed above that the temperature dependence of the heat capacity of the C-doped Ni<sub>147</sub> cluster exhibits two maxima corresponding to surface and volume melting of the cluster. It is seen from Fig. 6.4 that the first maximum in the temperature dependence of the heat capacity appears when the cluster is at  $T = 640$  K (surface melting), while the second maximum appears at  $T = 720$  K (volume melting). The temperature of 680 K corresponds to the intermediate state when the surface of the cluster has already melted but the cluster core is still frozen, as confirmed by the analysis of the atomic trajectories. As can be seen in Fig. 6.5 at  $T = 680$  K, the surface Ni atom begins to diffuse on the surface, while the central Ni atom and the C impurity are still vibrating around their equilibrium positions. Note, that the icosahedral surface is inhomogeneous and consists of 12 vertices, 20 faces and 30 edges. The binding energies of the atoms taken from the vertices, faces and edges are thus slightly different. Hence, these atoms begin diffusion at different temperatures.

Finally at the temperature of 800 K, cluster has completely melted as can be observed from the temperature behavior of the heat capacity presented in Fig. 6.4. Figure 6.5 demonstrates that the Ni atoms are moving in the entire volume of the cluster. The C impurity is also moving randomly in the cluster volume although the movement only occurs in the central part of the cluster. Hence, this supposes the heterogeneous distribution of the C atoms

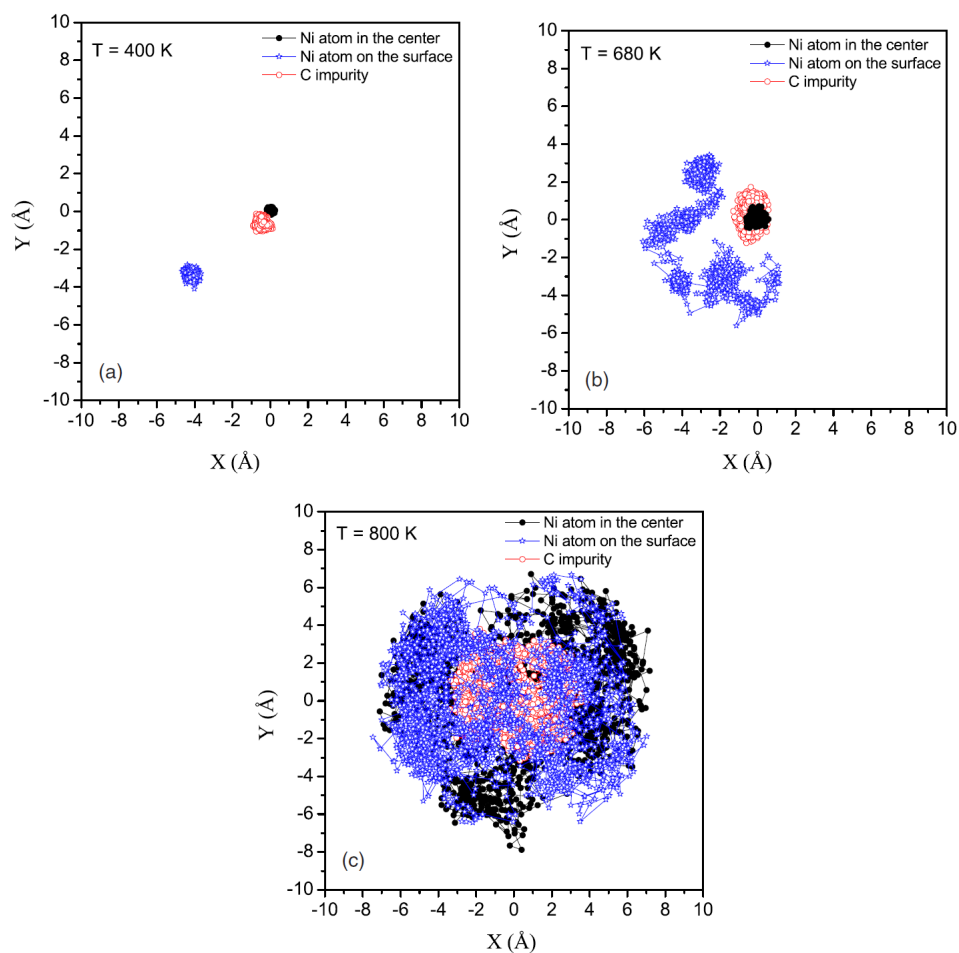


Figure 6.5: The two-dimensional projection of trajectories calculated for the Ni atom in the center of the C-doped Ni<sub>147</sub> cluster (filled dots), the Ni atom from the vertex of the cluster surface (stars) and the C impurity (open dots) for the cluster temperatures  $T = 400$  K, 680 K, and 800 K. The output time step is 1 ps and the total simulation time is 2 ns.

in the melted  $\text{Ni}_{147}$  clusters at  $T=800$  K.

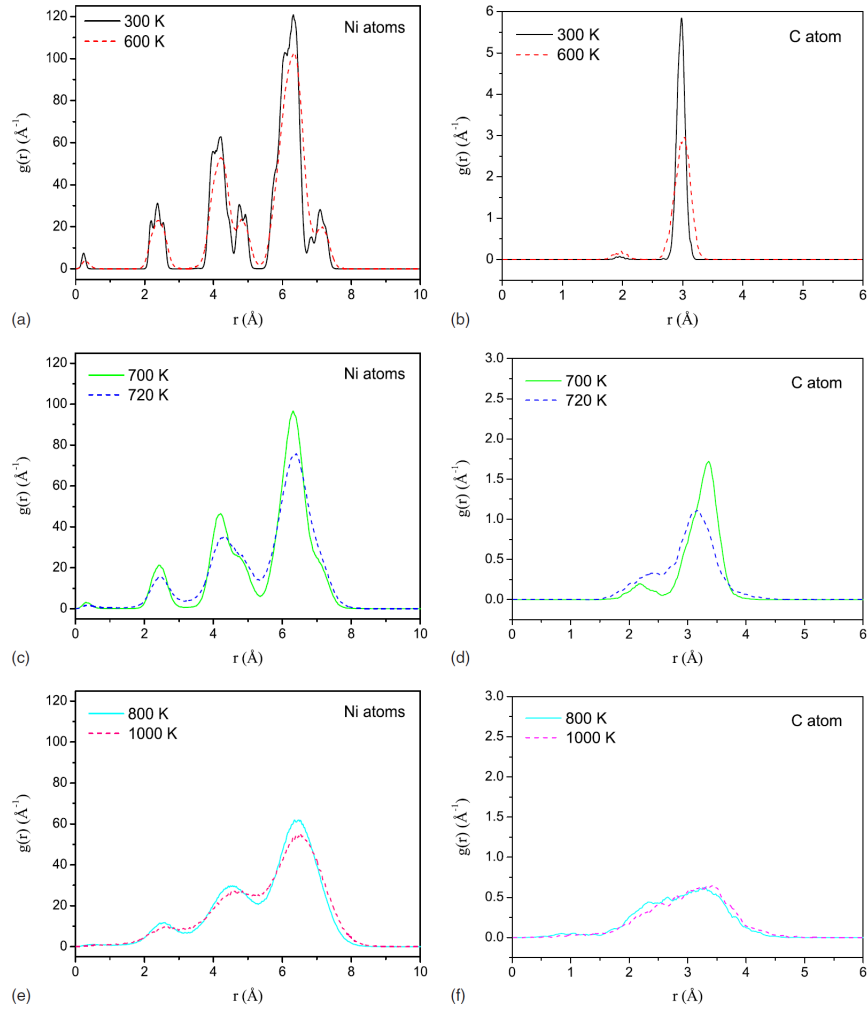


Figure 6.6: The time-averaged radial distribution function  $g(r)$  calculated for the Ni and C atoms in the C-doped  $\text{Ni}_{147}$  cluster at different temperatures.

The change in cluster structure upon melting is clearly seen in the time-averaged radial distribution of atoms in the cluster. The radial atomic distribution function  $g(r)$  is defined as:

$$g(r) = dN(r)/dr, \quad (6.3)$$

where  $dN(r)$  is the number of atoms in the spherical layer at distances between  $r$  and  $r + dr$  from the center of mass of the cluster.

Figure 6.6 demonstrates the time-averaged radial distribution function  $g(r)$  for Ni and C atoms in the C-doped Ni<sub>147</sub> cluster calculated at cluster temperatures of  $T = 300$  K, 600 K, 700 K, 720 K, 800 K, and 1000 K. The chosen range of temperatures allows for the analysis of the cluster structure in the frozen, transitional and molten states.

At the low cluster temperature,  $T = 300$  K, one can see the icosahedral shell structure of the nickel subsystem of the C-doped Ni<sub>147</sub> cluster, consisting of the central atom and three icosahedral shells. The second and third shells are split—corresponding to atoms in vertex (12 atoms per shell) and non-vertex positions. Heating the cluster up to 600 K washes out the subshell splitting, nonetheless the icosahedral shells remain well separated.

With increase in the cluster temperature, up to 700 K, the second and the third shells begin to merge, although the first and the second shells are still separated (i.e., the radial distribution function  $g(r)$  is equal to zero in the space between shells). At the temperature corresponding to the maximum in the heat capacity of the C-doped Ni<sub>147</sub> cluster,  $T = 720$  K, the first and second icosahedral shells merge.

Finally, at the temperatures corresponding to the molten state (800 K and 1000 K in Fig. 6.6), the distribution of Ni atoms become more homogeneous and the sharp shell structure washes out. Nevertheless, even at  $T = 1000$  K, some radial order with maxima at 2.6 Å, 4.6 Å, and 6.5 Å still remains, suggesting that even a molten cluster of a finite size manifests some signs of a shell structure. This effect might be a general feature of finite systems, similar to the surface-induced ordering in liquid crystals or the layering effect at free liquid surfaces [220–222].

Figure 6.6 demonstrates that, at cluster temperatures 300 K and 600 K, the time-averaged radial distribution function calculated for the C impurity atom exhibits a sharp maximum at distances 3 Å from the center of mass of the C-doped Ni<sub>147</sub> cluster. Thus, at these temperatures, the C impurity is located between the first and the second icosahedral shells of the Ni atoms. By further increasing the cluster temperature to temperatures near the phase

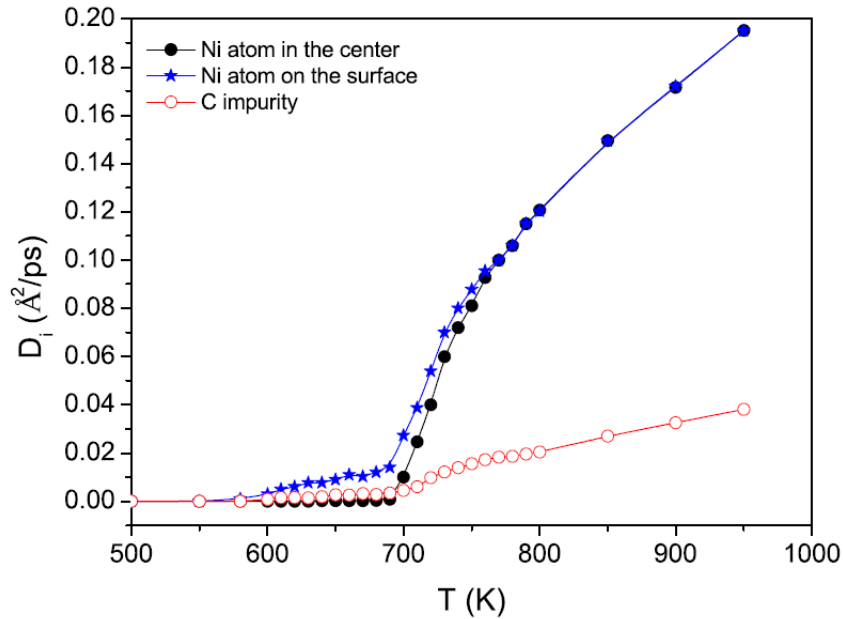


Figure 6.7: Temperature dependence of diffusion coefficients calculated for the Ni atom in the center of the C-doped Ni<sub>147</sub> cluster (filled dots), the Ni atom on the cluster surface (stars) and the C impurity (open dots).

transition region, the radial distribution  $g(r)$  of the C impurity becomes wider and the appearance of a second maximum at distances  $\approx 2 \text{ \AA}$  can be observed. While at  $T > 800 \text{ K}$ , the C impurity can be found to be distributed in the central part of the cluster.

Figure 6.7 demonstrates the temperature dependence of diffusion coefficients calculated for the selected atoms in the C-doped Ni<sub>147</sub> cluster. It is seen from Fig. 6.7 that the Ni atom on the cluster surface begins to diffuse at temperature of 600 K, while Ni atom in the cluster center and the C impurity remain frozen.

As has been shown above, the caloric curve calculated for the C-doped Ni<sub>147</sub> cluster (see Fig. 6.4) clearly demonstrates a stepwise melting behavior. In the temperature interval  $600 < T < 700 \text{ K}$ , the slope of the caloric curve changes slightly in comparison with that for the frozen state, suggesting the existence of a pre-melted state. For the temperatures  $700 < T < 760$

the time-averaged total energy  $\langle E_{tot} \rangle$  growing rapidly and finally reaches its asymptotic behavior at  $T > 760$  K. The variations in the slope of the caloric curve result in the appearance of the two maxima in the temperature dependence of the heat capacity. These maxima are associated with the surface and core (volume) melting of the C-doped  $\text{Ni}_{147}$  cluster. This proposition is fully confirmed by the analysis of the temperature dependence of the diffusion coefficients for the Ni atoms from: (a) the cluster surface and (b) the cluster center.

Thus, in the temperature interval of  $600 < T < 700$  K, only surface atoms diffuse, confirming that the initial melting of the cluster surface. The Ni atom located in the cluster center then begins to diffuse at  $T = 700$  K. The diffusion coefficients calculated for Ni atoms located on the cluster surface and in the core are different up to  $T = 760$  K. The difference in the diffusion coefficients show that the surface and the core atoms are not yet fully mixed in the cluster volume. The difference disappears at cluster temperatures of  $T > 760$  K, when the C-doped  $\text{Ni}_{147}$  cluster has become completely molten.

Figure 6.7 demonstrates that the C impurity begins to diffuse at  $T \approx 700$  K—similar to the central Ni atom. However, values of the diffusion coefficients calculated for the C impurity are considerably lower than those for the Ni atoms. Knowledge of the diffusion coefficients of the C impurity in a nickel cluster can be used for building a reliable kinetic model of carbon nanotube growth [223].

## 6.2 MODIFYING THE NI-C INTERACTION

We now investigate what occurs when the Ni-C interaction is modified. The purpose of this is to study in detail how changing the interaction can induce or release strain in the lattice of the C-doped  $\text{Ni}_{147}$  cluster, leading to a change in its thermodynamic behaviour.

To do this, we have performed calculations of the melting temperature of the cluster for a set of different parameters  $\rho$  and  $r_0$  in the Morse potential (2.26)—in other words, modeling the variation in the Ni-C interaction.

Curve 1 in Fig. 6.8 presents the dependence of the Morse potential  $V^{\text{Ni-C}}(r)$

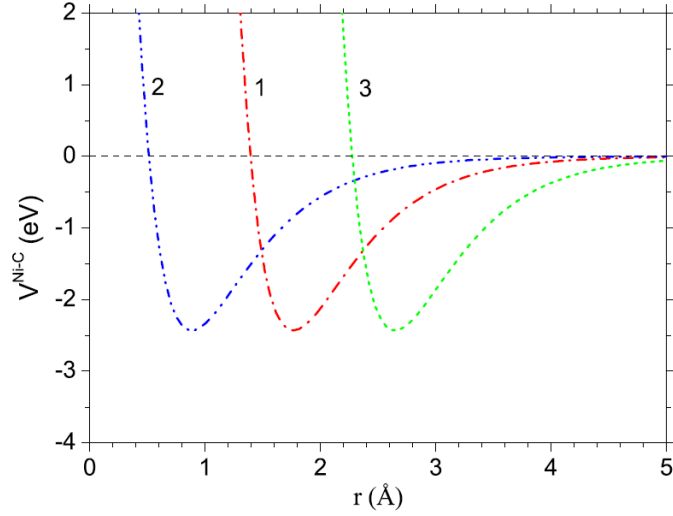


Figure 6.8: Morse potential for the Ni – C interaction with different values of parameters  $\rho$  and  $r_0$ . *Curve 1*,  $\rho = 3.295$ ,  $r_0 = 1.763 \text{ \AA}$  (optimal values); *Curve 2*,  $\rho = 1.648$ ,  $r_0 = 0.882 \text{ \AA}$  (reduced bonding); *Curve 3*,  $\rho = 4.943$ ,  $r_0 = 2.645 \text{ \AA}$  (enlarged bonding). The depth of the potential well is kept constant  $\varepsilon_M = 2.431 \text{ eV}$ .

on the interatomic distance  $r$  calculated for the optimal values of the parameters  $\varepsilon_M$ ,  $\rho$ , and  $r_0$ . Curve 2 in Fig. 6.8 presents the potential  $V^{Ni-C}(r)$  when the bond constant  $r_0$  and parameter  $\rho$  are reduced by the factor 0.5 in comparison to their optimal values; while curve 3 in Fig. 6.8 presents the interaction potential  $V^{Ni-C}(r)$  when the parameters  $r_0$  and  $\rho$  are enlarged by the factor 1.5. Hence, the potentials presented in Fig. 6.8 by curves 2 and 3 model the impurity effect with the local compression and expansion of the cluster lattice respectively.

To illustrate the effect of variation in the Ni–C interaction on cluster structure we present, in Figs. 6.9(a)-(c), the histogram of the radial distribution of the number of Ni atoms located at distances between  $r$  and  $r + \Delta r$  from the center of mass of the C-doped  $\text{Ni}_{147}$  cluster (where the width of the radial interval is  $\Delta r = 0.001 \text{ \AA}$ ). The change in the cluster structure, due to varying the parameters of  $\rho$  and  $r_0$  in the Morse potential, can thus be clearly seen. For comparison, Fig. 6.9(d) represents the histogram of the

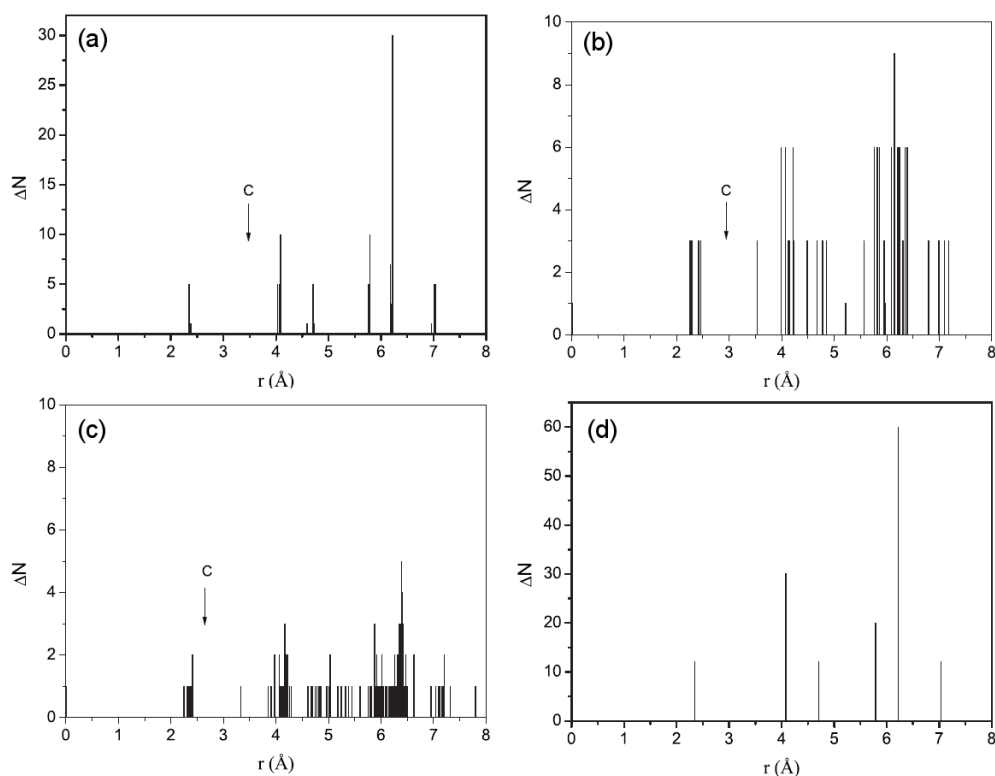


Figure 6.9: The number of Ni atoms  $\Delta N$  at distances between  $r$  and  $r + \Delta r$  from the center of mass of the C-doped  $\text{Ni}_{147}$  cluster calculated for different values of the parameters  $\rho$  and  $r_0$ : (a)  $\rho = 1.648$ ,  $r_0 = 0.882$  Å (reduced bonding); (b)  $\rho = 3.295$ ,  $r_0 = 1.763$  Å (optimal values); (c)  $\rho = 4.943$ ,  $r_0 = 2.645$  Å (enlarged bonding); (d) pure  $\text{Ni}_{147}$  cluster for comparison. The radial interval  $\Delta r$  is  $0.001$  Å.

radial distribution of the number of Ni atoms in the pure  $\text{Ni}_{147}$  cluster.

In the case of the reduced bonding between the C impurity and the Ni atoms, the overall icosahedral shell structure of the cluster remains preserved—although there exists some relaxation of the lattice, Fig. 6.9(a). The increase of the effective radius of the Morse potential for the Ni – C interaction results in strong distortions of the icosahedral shell structure of the cluster, Figs. 6.9(b) and 6.9(c). Such distortions reduce the stability of the cluster in comparison to the compact icosahedral structure.

Figure 6.10 demonstrates the temperature dependence of the caloric curve



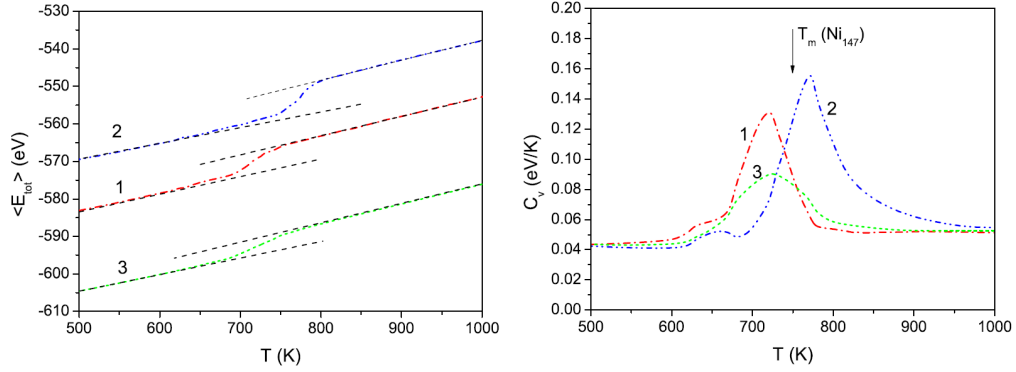


Figure 6.10: (Left) caloric curves for the C-doped  $\text{Ni}_{147}$  cluster calculated for the different values of parameters  $\rho$  and  $r_0$ . *Curve 1*,  $\rho = 3.295$ ,  $r_0 = 1.763$  Å (optimal values); *Curve 2*,  $\rho = 1.648$ ,  $r_0 = 0.882$  Å (reduced bonding); *Curve 3*,  $\rho = 4.943$ ,  $r_0 = 2.645$  Å (enlarged bonding). The depth of the potential well is kept constant  $\varepsilon_M = 2.431$  eV. (Right) heat capacity for the C-doped  $\text{Ni}_{147}$  cluster calculated for the different values of parameters  $\rho$  and  $r_0$ . *Curve 1*,  $\rho = 3.295$ ,  $r_0 = 1.763$  Å (optimal values); *Curve 2*,  $\rho = 1.648$ ,  $r_0 = 0.882$  Å (reduced bonding); *Curve 3*,  $\rho = 4.943$ ,  $r_0 = 2.645$  Å (enlarged bonding). The depth of the potential well is kept constant  $\varepsilon_M = 2.431$  eV. Arrow indicates the melting temperature of the pure  $\text{Ni}_{147}$  cluster.

and the heat capacity of the C-doped  $\text{Ni}_{147}$  cluster calculated for the different parameters of the Morse potential  $V^{\text{Ni-C}}(r)$ . Curves 1 in Figs. 6.10 and 6.10 present the caloric curve and the heat capacity calculated with the optimal values of parameters for the Ni – C interaction.

Decreasing the effective radius of the Morse potential (see curve 2, Fig. 6.8) by a factor 0.5 (*c.f.* the optimal values) results in the contraction of the cluster lattice in the vicinity of impurity. This contraction releases the strain in the icosahedral structure, therefore leading to an increase of the cluster stability. In this case the, melting temperature of the impurity doped  $\text{Ni}_{147}$  cluster increases by 21 K, compared the pure cluster (see curve 2 in Fig. 6.10).

An increase in the effective radius of the Morse potential for Ni – C interaction to its optimal value (see curve 1 in Fig. 6.8) results in the appearance of an additional strain in the cluster lattice. Therefore, the melting temperature of the C-doped  $\text{Ni}_{147}$  cluster decreases compared to the pure  $\text{Ni}_{147}$  cluster.

The further increase in the effective radius of the Ni – C interaction creates a strong deformation and rearrangement in the cluster structure, see Fig. 6.9(c). In this case, location of the impurity in the vicinity of the cluster center becomes energetically unfavourable. Thus, the impurity atom shifts towards the cluster surface to minimize the destruction of the icosahedral lattice. This effect prevents the further decrease in the melting temperature of the cluster, as an impurity located on the cluster surface will not have much influence on the melting transition of the core.

### 6.3 CHAPTER SUMMARY

Doping of Ni<sub>147</sub> with a carbon impurity lowers its melting temperature by 30 K due to excessive stress on the cluster lattice. The magnitude of the change induced is dependent upon the parameters of the interaction between the nickel atoms and the carbon impurity. We have demonstrated that an induced contraction of the icosahedral clusters lattice in the vicinity of the impurity results in an increase of the melting temperature of the cluster; whereas additional strain in the lattice results in the reduction of the melting temperature. Therefore, the melting temperature of atomic clusters can be effectively tuned by the addition of an impurity of a particular type.

Doping by a C impurity changes the melting temperature of the cluster, consequently this means that doping affects the mobility of the atoms in the Ni cluster. This effect has to be taken into consideration in particular applications with metal clusters when the entire process depends on the thermodynamic state of the cluster. An example of such experiment is the process of the catalytically activated growth of carbon nanotubes. The kinetics of the carbon nanotube growth depends upon diffusion of carbon atoms through the metal catalyst. Presence of the impurities can considerably change the flux, thereby affecting the growth rate of the carbon nanotube. The additional change in the thermodynamic state of the catalytic particle in the nanotube growth process might also depend on the strength of the interaction of the particle with a substrate.

## CHAPTER 7

# CONCLUSIONS

In this thesis, we have presented a study of phase transitions in nanocarbon systems, with a particular emphasis on fullerenes. Fullerenes can be considered as atomic clusters—finite systems that are a bridge between quantum objects and bulk matter. The work presented in this thesis is largely theoretical in nature, employing as a tool, molecular dynamics simulations to probe the dynamic stability of fullerenes and associated nanocarbon structures such as graphenes and nanotubes.

We have first investigated the phase transition of buckminsterfullerene  $C_{60}$ , using the Tersoff potential and a novel forcefield that we have developed—the Topologically-constrained forcefield [1]. With the Tersoff potential, we have conducted simulations up to 1000 ns, and have shown that short simulations of length 50 ns or less may overestimate the phase transition temperature involved in the sublimation of fullerenes. However, the result of the 500 ns simulation converges with that of the 1000 ns. Within this potential, the  $C_{60}$  was observed to transform into a series of phases prior to multifragmentation into a carbon gas. These phases are tube-like, bowl-like and graphene-like in structure respectively. Together with these phase transformations, the  $C_{60}$  was also seen to evaporate a  $C_2$  or C atom. However, by compressing the simulation volume (thus, increasing the pressure), the transient graphene phase was shown to become metastable between 3600–4300 K. Analysis of the caloric curves and heat capacities of  $C_{60}$  within the two different volumes show that  $C_{60}$  experiences a first-order-like phase tran-

sition in the larger volume, and a second-order-like phase transition in the smaller (higher pressure) volume. These simulations were repeated using the Topologically-constrained forcefield. Within this novel potential, the  $C_{60}$  did not exhibit transient phase transformations prior to multifragmentation. However, in the smaller volume, the  $C_{60}$  showed a dynamic phase coexistence where successive and repetitive fullerene fragmentation and formation was observed within the trajectory of the system at the phase transition temperature.

These results using the Topologically-constrained forcefield was then used in a statistical mechanics model that was developed to investigate the  $C_{60} \leftrightarrow 30C_2$  channel of fullerene formation and destruction. Using the statistical mechanics model, we were able to correspond the conditions of the dynamic phase coexistence of  $C_{60}$  to the generalised pressure and temperature conditions in typical arc-discharge experiments, although the correspondence is quite idealised due to the complex nature of the experimental conditions which may include nonequilibrium effects.

Furthermore, we have studied the phase transitions in fullerenes  $C_{32}$ ,  $C_{70}$ ,  $C_{80}$ ,  $C_{90}$ ,  $C_{180}$ ,  $C_{240}$  and  $C_{540}$ . The results of the molecular dynamics simulations show that larger fullerenes should be more stable than  $C_{60}$ , in correspondence to the fact that higher fullerenes have higher binding energies than  $C_{60}$ . However, this is despite the fact that  $C_{60}$  has been shown to be more abundant than any other fullerene size in various fullerene-generating methods. Thus, thermodynamic and energetic criteria alone are ill-equipped to describe the stability of fullerenes.

Moreover, the fragmentation pathways are different for fullerenes the size of  $C_{70}$  and smaller, compared to fullerenes  $C_{80}$  to  $C_{540}$ . Small fullerenes were shown to transform into transient graphene-like phases before multifragmentation to the carbon gas phase. Whereas no such phase were observed for the larger fullerenes. Such a behaviour may be attributed to entropic factors which would make transformation to the graphene-like phase unlikely.

We have also investigated the phase transitions of a cluster of 240 carbon atoms in the form of a fullerene, a buckybowl, a  $C_{60}@C_{180}$  carbon onion, a graphene element and an uncapped (10,10) nanotube [2]. In this study, we

have found that the carbon onion, nanotube and buckyball structures transform into a fullerene before a phase transition to carbon gas. The graphene fragment, on the other hand, showed no transformation to other phases prior to disintegration, allowing one to surmise that it follows a different fragmentation pathway.

Finally, we have investigated how the addition of a carbon atom or a  $C_2$  molecule considerably influences the melting temperature of a nickel cluster,  $Ni_{147}$  [15]. This effect has to be taken into consideration, particularly in applications with metal clusters when the entire process depends on the thermodynamic state of the cluster. The relevant example of such an application is the catalytically-activated growth of carbon nanotubes using chemical vapour deposition. As the carbon nanotube growth depends upon diffusion of carbon atoms through the metal catalyst, the presence of impurities can considerably change the flux, thereby affecting the growth rate of the carbon nanotube. The additional change in the thermodynamic state of the catalytic particle in the nanotube growth process might also depend on the strength of the interaction of the particle with a substrate.

The study of the phase transition of  $C_{60}$ , as well as that of small nanocarbon structures, is an important step in the understanding of the stability and resilience of these structures, as well as their formation mechanisms and their transformations from one phase to another. Moreover, knowledge of the phase transition of carbon nanostructures is important is the construction of a nanocarbon phase diagram which would allow one to know the upper and lower limits of the stability of a nanocarbon phase for a given temperature, pressure and number of atoms. Such information would be indispensable in any application involving nanocarbon structures, in particular, for nanoelectronics.



## BIBLIOGRAPHY

- [1] A. Hussien, A. V. Yakubovich, A. V. Solovyov, and W. Greiner. Phase transition, formation and fragmentation of fullerenes. *The European Physical Journal D - Atomic, Molecular, Optical and Plasma Physics*.
- [2] Adilah Hussien, Alexander V. Yakubovich, and Andrey V. Solov'yov. Studying phase transition in nanocarbon structures. In Andrey Solov'yov and Eugene Surdutovich, editors, *The Fourth International Symposium, Atomic Cluster Collisions: Structure and dynamics from the nuclear to the biological scale (ISACC 2009)*, volume 1197, pages 152–173, Ann Arbor (Michigan), December 2009. AIP.
- [3] Francesca Baletto and Riccardo Ferrando. Structural properties of nanoclusters: Energetic, thermodynamic, and kinetic effects. *Rev. Mod. Phys.*, 77(1):371–423, 2005.
- [4] M. Bixon and Joshua Jortner. Energetic and thermodynamic size effects in molecular clusters. *J. Chem. Phys.*, 91(3):1631–1642, 1989.
- [5] Joshua Jortner. Cluster size effects. *Z. Phys. D.*, 24(3):247–275, 1992.
- [6] Alexandre A. Shvartsburg and Martin F. Jarrold. Solid clusters above the bulk melting point. *Phys. Rev. Lett.*, 85(12):2530, 2000.
- [7] Yoshiyuki Kawazoe, Kaoru Ohno, and Tamotsu Kondow. *Clusters and nanomaterials*. Springer, 2002.
- [8] Gary A. Breaux, Robert C. Benirschke, Toshiki Sugai, Brian S. Kinnear, and Martin F. Jarrold. Hot and solid gallium clusters: Too small to melt. *Phys. Rev. Lett.*, 91(21):215508, 2003.

- [9] Hellmut Haberland, Thomas Hippler, Jörn Donges, Oleg Kostko, Martin Schmidt, and Bernd von Issendorff. Melting of sodium clusters: Where do the magic numbers come from? *Phys. Rev. Lett.*, 94(3):035701, 2005.
- [10] Jean-Patrick Connerade and Andrey Solov'yov. *Latest advances in atomic cluster collisions*. Imperial College Press, 2008.
- [11] Andrey V. Solovyov. *The Fourth International Symposium Atomic Cluster Collisions*. American Institute of Physics, 2009.
- [12] H. Kroto, J. Heath, S. O'Brien, R. Curl, and R. Smalley. C<sub>60</sub>: Buckminsterfullerene. *Nature*, 318:162–163, 1985.
- [13] Ulrich Heiz and Uzi Landman. *Nanocatalysis*. Springer, 2007.
- [14] Sarah Darby, Thomas V. Mortimer-Jones, Roy L. Johnston, and Christopher Roberts. Theoretical study of Cu–Au nanoalloy clusters using a genetic algorithm. *J. Chem. Phys.*, 116(4):1536–1550, 2002.
- [15] Andrey Lyalin, Adilah Hussien, Andrey V. Solov'yov, and Walter Greiner. Impurity effect on the melting of nickel clusters as seen via molecular dynamics simulations. *Phys. Rev. B*, 79(16):165403, 2009.
- [16] Ado Jorio, Gene Dresselhaus, and M. S. Dresselhaus. *Carbon nanotubes*. Springer, 2008.
- [17] February 2010 Google Scholar estimate for publications containing at least the word “fullerene” or “C<sub>60</sub>” or “buckyball” in the title.
- [18] Harold Kroto. Symmetry, space, stars and C<sub>60</sub>. *Rev. Mod. Phys.*, 69(3):703, 1997.
- [19] Robert F. Curl. Dawn of the fullerenes: experiment and conjecture. *Rev. Mod. Phys.*, 69(3):691, 1997.
- [20] Richard E. Smalley. Discovering the fullerenes. *Rev. Mod. Phys.*, 69(3):723, 1997.



- [21] D. E. H. Jones. *New Scient.*, page 245, 1966.
- [22] E. Osawa. *Kagaku*, 25:854, 1970.
- [23] Z. Yoshida and E. Osawa. Aromaticity. *Kagakudojin*, 1971.
- [24] D. A. Bochvar and E. G. Gal'pern. *Dokl. Akad. Nauk SSSR*, 203:610, 1973.
- [25] Robert A. Davidson. Spectral analysis of graphs by cyclic automorphism subgroups. *Theor. Chem. Acc.*, 58(3):193–231, 1981.
- [26] A. D. J. Haymet. Footballene: a theoretical prediction for the stable, truncated icosahedral molecule  $C_{60}$ . *J. Am. Chem. Soc.*, 108(2):319–321, 1986.
- [27] W. Krätschmer, L. D. Lamb, K. Fostiropoulos, and D. R. Huffman. Solid  $C_{60}$ : a new form of carbon. *Nature*, 347:354 – 358, 1990.
- [28] K. Säidane, M. Razafinimanana, H. Lange, A. Huczko, M. Baltas, A. Gleizes, and J-L. Meunier. Fullerene synthesis in the graphite electrode arc process: local plasma characteristics and correlation with yield. *J. Phys. D: Appl. Phys.*, 37:232, 2004.
- [29] T. Wakabayashi and Y. Achiba. A model for the  $C_{60}$  and  $C_{70}$  growth mechanism. *Chem. Phys. Lett.*, 190(5):465–468, 1992.
- [30] T. Wakabayashi, K. Kikuchi, H. Shiromaru, S. Suzuki, and Y. Achiba. Ring-stacking consideration on higher fullerene growth. *Z. Phys. D.*, 26(0):258–260, 1993.
- [31] J. Y. Huang, Feng Ding, Kun Jiao, and Boris I. Yakobson. Real time microscopy, kinetics, and mechanism of giant fullerene evaporation. *Phys. Rev. Lett.*, 99:175503, 2007.
- [32] Hiroaki Takehara, Masashi Fujiwara, Mineyuki Arikawa, Michael D. Diener, and J. Michael Alford. Experimental study of industrial scale fullerene production by combustion synthesis. *Carbon*, 43(2):311–319, 2005.

- [33] Andreas Hirsch and Michael Brettreich. *Fullerenes: Chemistry and Reactions*. Wiley-VCH, 1 edition, 2005.
- [34] Gonzalo Otero, Giulio Biddau, Carlos Sanchez-Sanchez, Renaud Cail-  
lard, Maria F. Lopez, Celia Rogero, F. Javier Palomares, Noemi Ca-  
bello, Miguel A. Basanta, Jose Ortega, Javier Mendez, Antonio M.  
Echavarren, Ruben Perez, Berta Gomez-Lor, and Jose A. Martin-Gago.  
Fullerenes from aromatic precursors by surface-catalysed cyclodehydro-  
genation. *Nature*, 454(7206):865–868, 2008.
- [35] S. C. O’Brien, J. R. Heath, R. F. Curl, and R. E. Smalley. Photophysics  
of buckminsterfullerene and other carbon cluster ions. *J. Chem. Phys.*,  
88:220, 1988.
- [36] T. Sommer, T. Kruse, and P. Roth. Thermal stability of fullerenes: a  
shock tube study on the pyrolysis of and. *J. Phys. B: At. Mol. Opt.  
Phys.*, 29:4955–4964(10), 1996.
- [37] A. Reinköster, B. Siegmann, U. Werner, B. A. Huber, and H. O. Lutz.  
Multi-fragmentation of C<sub>60</sub> after collisions with Ar<sup>z+</sup> ions. *J. Phys. B:  
At. Mol. Opt. Phys.*, 35:4989–4997, 2002.
- [38] Thomas Kunert and Rüdiger Schmidt. Excitation and fragmentation  
mechanisms in ion-fullerene collisions. *Phys. Rev. Lett.*, 86:5258–5261,  
2001.
- [39] R. Ehlich, M. Westerburg, and E. E. B. Campbell. Fragmentation of  
fullerenes in collisions with atomic and molecular targets. *J. Chem.  
Phys.*, 104:1900–1911, 1996.
- [40] B. Concina, S. Tomita, N. Takahashi, T. Kodama, S. Suzuki,  
K. Kikuchi, Y. Achiba, A. Gromov, J.U. Andersen, and P. Hvelplund.  
Delayed ionisation of C<sub>76</sub>. *Int. J. Mass Spectrom.*, 252:96 – 99, 2006.
- [41] C. Bordas, B. Baguenard, B. Climen, M.A. Lebeault, F. Lépine, and  
F. Pagliarulo. Time-dependent spectrum of thermionic emission from  
hot C<sub>60</sub>. *Eur. Phys. J. D*, 34:151–155, 2005.

- [42] E. E. B. Campbell and R. D. Levine. Delayed ionization and fragmentation en route to thermionic emission: Statistics and Dynamics. *Annual Review of Physical Chemistry*, 51(1):65–98, 2000.
- [43] F. Rohmund, A. G. Glotov, K. Hansen, and E. E. B. Campbell. Experimental studies of fusion and fragmentation of fullerenes. *J. Phys. B: At. Mol. Opt. Phys.*, 29:5143–5161, 1996.
- [44] A. Rentenier, D. Bordenave-Montesquieu, P. Moretto-Capelle, and A. Bordenave-Montesquieu. Kinetic energies of charged fragments resulting from multifragmentation and asymmetric fission of the  $C_{60}$  molecule in collisions with monocharged ions (2-130 keV). *J. Phys. B: At. Mol. Phys.*, 36:1585–1602, 2003.
- [45] B. L. Zhang, C. Z. Wang, C. T. Chan, and K. M. Ho. Thermal disintegration of carbon fullerenes. *Phys. Rev. B*, 48:11381–11384, 1993.
- [46] B. L. Zhang, C. Z. Wang, K. M. Ho, and C. T. Chan. Melting of carbon cages. *Z. Phys. D*, 26:285–287, 1993.
- [47] C. Z. Wang, C. H. Xu, C. T. Chan, and K. M. Ho. Disintegration and formation of  $C_{60}$ . *J. Phys. Chem.*, 96:3563 – 3565, 1992.
- [48] Seong Gon Kim and David Tománek. Melting the fullerenes: A molecular dynamics study. *Phys. Rev. Lett.*, 72:2418–2421, 1994.
- [49] Eunja Kim, Young Hee Lee, and Jae Young Lee. Fragmentation of  $C_{60}$  and  $C_{70}$  clusters. *Phys. Rev. B*, 48:18230–18234, 1993.
- [50] I.u László. Tight-binding molecular dynamics simulation of the disintegration of fullerenes. *Fullerenes, Nanotubes, Carbon Nanostruct.*, 5:2:375–388, 1997.
- [51] L. A. Openov and A. I. Podliavev. Numerical simulation of the thermal fragmentation process in fullerene  $C_{60}$ . *JETP Lett.*, 84:68, 2006.

- [52] C.H. Xu, C. Z. Wang, Chan C. T., and K. M. Ho. A transferable tight-binding potential for carbon. *J. Phys.: Condens. Matt.*, 4:6047–6054, 1992.
- [53] J. Tersoff. New empirical approach for the structure and energy of covalent systems. *Phys. Rev. B*, 37(12):6991, 1988.
- [54] J. Tersoff. Empirical interatomic potential for carbon, with applications to amorphous carbon. *Phys. Rev. Lett.*, 61(25):2879–2882, 1988.
- [55] D. W. Brenner, O. A. Shenderova, J. A. Harrison, S. J. Stuart, and S. B. Sinnott. A second-generation reactive empirical bond order (rebo) potential energy expression for hydrocarbons. *J. Phys.: Condens. Matter*, 14:783–802, 2002.
- [56] S. Serra, S. Sanguinetti, and L. Colombo. Pre-fragmentation dynamics of c60. a molecular dynamics investigation. *Chemical Physics Lett.*, 225(1-3):191–195, July 1994.
- [57] M.J. López, P.A. Marcos, A. Rubio, and J.A. Alonso. Thermal behaviour of carbon clusters and small fullerenes. *Zeitschrift fr Physik D Atoms, Molecules and Clusters*, 40(1):385–388, May 1997.
- [58] P. A. Marcos, J. A. Alonso, A. Rubio, and M. J. López. Simulating the thermal stability and phase changes of small carbon clusters and fullerenes. *Eur. Phys. J. D*, 6:221–233, 1999.
- [59] W. Zhang, Z. Xu, and Z. Zhu. Study of Thermal Stability of Fullerenes by Molecular Dynamics. *Int. J. Mod. Phys. B*, 19:2892–2898, 2005.
- [60] Chunhui Xu and Gustavo E. Scuseria. Tight-binding molecular dynamics simulations of fullerene annealing and fragmentation. *Phys. Rev. Lett.*, 72:669–672, 1994.
- [61] L. Horváth and T. A. Beu. Tight-binding molecular dynamics simulations of radiation-induced fragmentation of C<sub>60</sub>. *Phys. Rev. B*, 77:075102, 2008.

- [62] R. C. Mowrey, D. W. Brenner, B. I. Dunlap, J. W. Mintmire, and C. T. White. Simulations of buckminsterfullerene (C<sub>60</sub>) collisions with a hydrogen-terminated diamond 111 surface. *J. Phys. Chem.*, 95(19):7138–7142, 1991.
- [63] Ryan T. Chancey, Lene Oddershede, Frank E. Harris, and John R. Sabin. Fragmentation of fullerenes. *Phys. Rev. A*, 67(4):043203, Apr 2003.
- [64] Yueyuan Xia, Yuelin Xing, Chunyu Tan, and Liangmo Mei. Molecular-dynamics simulation of fragmentation of c60 colliding with h2. *Phys. Rev. B*, 52(1):110–115, Jul 1995.
- [65] Toshimori Sekine. Diamond recovered from shocked fullerites. *Proceedings of the Japan Academy. Ser. B: Physical and Biological Sciences*, 68(7):95–99, 1992.
- [66] Y. Iwasa, T. Arima, R. M. Fleming, T. Siegrist, O. Zhou, R. C. Haddon, L. J. Rothberg, K. B. Lyons, H. L. Carter, A. F. Hebard, R. Tycko, G. Dabbagh, J. J. Krajewski, G. A. Thomas, and T. Yagi. New phases of C<sub>60</sub> synthesized at high pressure. *Science*, 264(5165):1570–1572, 1994.
- [67] M. E. Kozlov, K. Yase, N. Minami, P. Fons, H.-A. Durand, A. N. Obraztsov, K. Nozaki, and M. Tokumoto. Observation of diamond crystallites in thin films prepared by laser ablation of hard fullerene-based carbon. *J. Phys. D: Appl. Phys.*, 29(3):929–933, 1996.
- [68] T. R. Ravindran and J. V. Badding. Ultraviolet raman analysis of the formation of diamond from C<sub>60</sub>. *Solid State Communications*, 121(6-7):391–393, 2002.
- [69] X. D. Zhu, Y. H. Xu, H. Naramoto, K. Narumi, A. Miyashita, and K. Miyashita. Ion-beam-assisted hexagonal diamond formation from C<sub>60</sub> fullerene. *J. Phys.: Condens. Matt.*, 15(17):2899–2906, 2003.

- [70] Nataliya F. Goldshleger. Fullerenes and fullerene-based materials in catalysis. *Fullerenes, Nanotubes, Carbon Nanostruct.*, 9(3):255, 2001.
- [71] V.M. Davidenko, S.V. Kidalov, F.M. Shakhov, M.A. Yagovkina, V.A. Yashin, and A.Ya. Vul'. Fullerenes as a co-catalyst for high pressure - high temperature synthesis of diamonds. *Diamond and Related Materials*, 13(11-12):2203–2206, 2004.
- [72] S. Kidalov, F. Shakhov, V. Davidenko, V. Yashin, I. Bogomazov, and A. Vul. Effect of carbon materials on the graphite-diamond phase transition at high pressures and temperatures. *Physics of the Solid State*, 50(5):981–985, 2008.
- [73] J Haines, Jm Leger, and G Bocquillon. SYNTHESIS AND DESIGN OF SUPERHARD MATERIALS. *Annual Review of Materials Research*, 31(1):1–23, 2001.
- [74] V. Blank, S. Buga, G. Dubitsky, N. Serebryanaya, M. Popov, and V. Prokhorov. Properties and applications of superhard and ultrahard fullerites. In *Perspectives of Fullerene Nanotechnology*, pages 223–233. 2002.
- [75] Takashi Horikawa, Kaichi Suito, Michihiro Kobayashi, and Ryuichiro Oshima. High-Pressure synthesis of superhard material from C<sub>60</sub>. *Jpn. J. Appl. Phys.*, 44:3141–3146, 2005.
- [76] Wolfgang Harneit. Fullerene-based electron-spin quantum computer. *Phys. Rev. A*, 65(3):032322, 2002.
- [77] Dieter Suter and Kyungwon Lim. Scalable architecture for spin-based quantum computers with a single type of gate. *Phys. Rev. A*, 65(5):052309, 2002.
- [78] J. Twamley. Quantum-cellular-automata quantum computing with endohedral fullerenes. *Phys. Rev. A*, 67(5):052318, 2003.

- [79] Simon C. Benjamin, Arzhang Ardavan, G. Andrew D. Briggs, David A. Britz, Daniel Gunlycke, John Jefferson, Mark A. G. Jones, David F. Leigh, Brendon W. Lovett, Andrei N. Khlobystov, S. A. Lyon, John J. L. Morton, Kyriakos Porfyraakis, Mark R. Sambrook, and Alexei M. Tyryshkin. Towards a fullerene-based quantum computer. *J. Phys.: Condens. Matt.*, 18(21):S867–S883, 2006.
- [80] Ming-Sen Chang and Jeng-Shong Shih. Fullerene-cryptand-coated piezoelectric crystal membrane glucose enzyme sensor. *Sensors and Actuators B: Chemical*, 67(3):275–281, 2000.
- [81] Jeng-Shong Shih, Yun-Ching Chao, Mine-Fag Sung, Guann-Jou Gau, and Chyow-San Chiou. Piezoelectric crystal membrane chemical sensors based on fullerene C<sub>60</sub>. *Sensors and Actuators B: Chemical*, 76(1-3):347–353, 2001.
- [82] I. Szymanska, H. Radecka, J. Radecki, and D. Kikut-Ligaj. Fullerene modified supported lipid membrane as sensitive element of sensor for odorants. *Biosensors and Bioelectronics*, 16(9-12):911–915, 2001.
- [83] J. R. Baena, M. Gallego, and M. Valcrcel. Fullerenes in the analytical sciences. *TrAC Trends in Analytical Chemistry*, 21(3):187–198, 2002.
- [84] Bailure S. Sherigara, Wlodzimierz Kutner, and Francis D’Souza. Electrocatalytic properties and sensor applications of fullerenes and carbon nanotubes. *Electroanalysis*, 15(9):753–772, 2003.
- [85] R. Sijbesma, G. Srdanov, F. Wudl, J. A. Castoro, Charles Wilkins, Simon H. Friedman, Dianne L. DeCamp, and George L. Kenyon. Synthesis of a fullerene derivative for the inhibition of HIV enzymes. *J. Am. Chem. Soc.*, 115(15):6510–6512, 1993.
- [86] Simon H. Friedman, Dianne L. DeCamp, Rint P. Sijbesma, Gordana Srdanov, Fred Wudl, and George L. Kenyon. Inhibition of the HIV-1 protease by fullerene derivatives: model building studies and experimental verification. *J. Am. Chem. Soc.*, 115(15):6506–6509, 1993.

- [87] Gian Luca Marcorin, Tatiana Da Ros, Sabrina Castellano, Giorgio Stefancich, Irena Bonin, Stanislav Miertus, and Maurizio Prato. Design and synthesis of novel [60]Fullerene derivatives as potential HIV aspartic protease inhibitors. *Organic Lett.*, 2(25):3955–3958, 2000.
- [88] Silvia Marchesan, Tatiana Da Ros, Giampiero Spalluto, Jan Balzarini, and Maurizio Prato. Anti-HIV properties of cationic fullerene derivatives. *Bioorganic & Medicinal Chemistry Lett.*, 15(15):3615–3618, 2005.
- [89] Tadahiko Mashino, Kumiko Shimotohno, Noriko Ikegami, Dai Nishikawa, Kensuke Okuda, Kyoko Takahashi, Shigeo Nakamura, and Masataka Mochizuki. Human immunodeficiency virus-reverse transcriptase inhibition and hepatitis c virus RNA-dependent RNA polymerase inhibition activities of fullerene derivatives. *Bioorganic & Medicinal Chemistry Lett.*, 15(4):1107–1109, 2005.
- [90] S. Nakamura and T. Mashino. Biological activities of water-soluble fullerene derivatives. *J. Phys.: Conf. Ser.*, 159:012003, 2009.
- [91] Tadahiko Mashino, Dai Nishikawa, Kyoko Takahashi, Noriko Usui, Takao Yamori, Masako Seki, Toyoshige Endo, and Masataka Mochizuki. Antibacterial and antiproliferative activity of cationic fullerene derivatives. *Bioorganic & Medicinal Chemistry Lett.*, 13(24):4395–4397, 2003.
- [92] P J Krusic, E Wasserman, P N Keizer, J R Morton, and K F Preston. Radical reactions of C<sub>60</sub>. *Science (New York, N.Y.)*, 254(5035):1183–1185, 1991.
- [93] Najla Gharbi, Monique Pressac, Michelle Hadchouel, Henri Szwarc, Stephen R Wilson, and Fathi Moussa. [60]fullerene is a powerful antioxidant in vivo with no acute or subacute toxicity. *Nano. Lett.*, 5(12):2578–2585, 2005.
- [94] L L Dugan, D M Turetsky, C Du, D Lobner, M Wheeler, C R Almlı, C K Shen, T Y Luh, D W Choi, and T S Lin. Carboxyfullerenes



- as neuroprotective agents. *Proceedings of the National Academy of Sciences of the United States of America*, 94(17):9434–9439, 1997.
- [95] Anya Maan-Yuh Lin, Su-Feng Fang, Shin-Zong Lin, Cheng-Kong Chou, Tieng-Yau Luh, and Low-Tone Ho. Local carboxyfullerene protects cortical infarction in rat brain. *Neuroscience Research*, 43(4):317–321, 2002.
- [96] Ya-Wen Chen, Kuo Chu Hwang, Cheng-Chieh Yen, and Yih-Loong Lai. Fullerene derivatives protect against oxidative stress in RAW 264.7 cells and ischemia-reperfused lungs. *Am. J. Physiol. Regul. Integr. Comp. Physiol.*, 287(1):R21–26, 2004.
- [97] M Bisaglia, B Natalini, R Pellicciari, E Straface, W Malorni, D Monti, C Franceschi, and G Schettini. C3-fullero-tris-methanodicarboxylic acid protects cerebellar granule cells from apoptosis. *J. Neurochem.*, 74(3):1197–1204, 2000.
- [98] D Monti, L Moretti, S Salvioli, E Straface, W Malorni, R Pellicciari, G Schettini, M Bisaglia, C Pincelli, C Fumelli, M Bonaf, and C Franceschi. C<sub>60</sub> carboxyfullerene exerts a protective activity against oxidative stress-induced apoptosis in human peripheral blood mononuclear cells. *Biochemical and Biophysical Research Communications*, 277(3):711–717, 2000.
- [99] Sarah Foley, Colin Crowley, Monique Smaili, Claude Bonfils, Bernard F Erlanger, Patrick Seta, and Christian Larroque. Cellular localisation of a water-soluble fullerene derivative. *Biochemical and Biophysical Research Communications*, 294(1):116–119, 2002.
- [100] Hiroyuki Isobe, Waka Nakanishi, Naoki Tomita, Shigeki Jinno, Hiroto Okayama, and Eiichi Nakamura. Nonviral gene delivery by tetraamino fullerene. *Molecular Pharmaceutics*, 3(2):124–134, 2006.
- [101] Jillian G Rouse, Jianzhong Yang, Jessica P Ryman-Rasmussen, Andrew R Barron, and Nancy A Monteiro-Riviere. Effects of mechanical

- flexion on the penetration of fullerene amino acid-derivatized peptide nanoparticles through skin. *Nano. Lett.*, 7(1):155–160, 2007.
- [102] Jessica P Ryman-Rasmussen, Jim E Riviere, and Nancy A Monteiro-Riviere. Penetration of intact skin by quantum dots with diverse physicochemical properties. *Toxicol. Sci.*, 91(1):159–165, 2006.
- [103] Sumio Iijima. Helical microtubules of graphitic carbon. *Nature*, 354(6348):56–58, November 1991.
- [104] Daniel Ugarte. Curling and closure of graphitic networks under electron-beam irradiation. *Nature*, 359(6397):707–709, 1992.
- [105] K. S. Novoselov, A. K. Geim, S. V. Morozov, D. Jiang, Y. Zhang, S. V. Dubonos, I. V. Grigorieva, and A. A. Firsov. Electric field effect in atomically thin carbon films. *Science*, 306(5696):666–669, 2004.
- [106] Linus Pauling. *The Nature of the Chemical Bond and the Structure of Molecules and Crystals; An Introduction to Modern Structural Chemistry*. Cornell University Press, 3 edition, 1960.
- [107] McNaught, A. D. and A. Wilkinson. *IUPAC. Compendium of Chemical Terminology, 2nd ed. (the "Gold Book")*. Blackwell Scientific Publications, Oxford, 1997.
- [108] G. C. Abell. Empirical chemical pseudopotential theory of molecular and metallic bonding. *Phys. Rev. B*, 31(10):6184, 1985.
- [109] James H. Rose, John R. Smith, and John Ferrante. Universal features of bonding in metals. *Phys. Rev. B*, 28(4):1835–1845, Aug 1983.
- [110] Ilia A. Solov'yov, Maneesh Mathew, Andrey V. Solov'yov, and Walter Greiner. Liquid surface model for carbon nanotube energetics. *Phys. Rev. E*, 78(5):051601, 2008.
- [111] M.J. López, I. Cabria, N.H. March, and J.A. Alonso. Structural and thermal stability of narrow and short carbon nanotubes and nanostrips. *Carbon*, 43:1371–1377, 2005.

- [112] M. Buongiorno Nardelli, C. Brabec, A. Maiti, C. Roland, and J. Bernholc. Lip-lip interactions and the growth of multiwalled carbon nanotubes. *Phys. Rev. Lett.*, 80(2):313–316, 1998.
- [113] N. Sawada, S. and Hamada. Energetics of carbon nano-tubes. *Solid State Comm.*, 83:917–919, 1992.
- [114] D. H. Robertson, D. W. Brenner, and J. W. Mintmire. Energetics of nanoscale graphitic tubules. *Phys. Rev. B*, 45(21):12592–12595, 1992.
- [115] Thomas W. Ebbesen, editor. *Carbon nanotubes: preparation and properties*. CRC Press, 1997.
- [116] Donald W. Brenner. Empirical potential for hydrocarbons for use in simulating the chemical vapor deposition of diamond films. *Phys. Rev. B*, 42(15):9458, 1990.
- [117] Steven J. Stuart, Alan B. Tutein, and Judith A. Harrison. A reactive potential for hydrocarbons with intermolecular interactions. *J. Chem. Phys.*, 112(14):6472–6486, 2000.
- [118] Jeremy Q. Broughton and Michael J. Mehl. Transferable potential for carbon without angular terms. *Phys. Rev. B*, 59(14):9259–9270, Apr 1999.
- [119] P. W. Fowler and D. E. Manolopoulos. *An Atlas of Fullerenes*. Oxford Univ. Press, 1995.
- [120] Branko S. Jursic. Reliability of hybrid density theory-semiempirical approach for evaluation of bond dissociation energies. *J. Chem. Soc. Perkin Trans. 2*, (2):369–372, 1999.
- [121] A. P. Sutton and J. Chen. Long-range Finnis-Sinclair potentials. *Philosophical Magazine Lett.*, 61(3):139, 1990.
- [122] H. Rafii-Tabar and A. P. Sulton. Long-range Finnis-Sinclair potentials for f.c.c. metallic alloys. *Philosophical Magazine Lett.*, 63(4):217, 1991.

- [123] B.D. Todd and R.M. Lynden-Bell. Surface and bulk properties of metals modelled with Sutton-Chen potentials. *Surface Science*, 281(1-2):191–206, 1993.
- [124] R. M. Lynden-Bell. A simulation study of induced disorder, failure and fracture of perfect metal crystals under uniaxial tension. *J. Phys.: Condens. Matter*, 7:4603–4624, June 1995.
- [125] Saroj K. Nayak, S. N. Khanna, B. K. Rao, and P. Jena. Physics of nickel clusters: Energetics and equilibrium geometries. *J. Phys. Chem. A*, 101(6):1072–1080, February 1997.
- [126] Jonathan P. K. Doye and David J. Wales. Global minima for transition metal clusters described by Sutton-Chen potentials. *New. J. Chem*, 22(7):733–744, 1998.
- [127] Y. Yamaguchi and S. Maruyama. A molecular dynamics study on the formation of metallofullerene. *Eur. Phys. J. D*, 9(1):385–388, 1999.
- [128] Yasushi Shibuta and Shigeo Maruyama. Bond-order potential for transition metal carbide cluster for the growth simulation of a single-walled carbon nanotube. *Computational Materials Science*, 39(4):842–848, June 2007.
- [129] Alberto Martinez-Limia, Jin Zhao, and Perla Balbuena. Molecular dynamics study of the initial stages of catalyzed single-wall carbon nanotubes growth: force field development. *J. Mol. Mod.*, 13(5):595–600, May 2007.
- [130] N. G. van Kampen. *Stochastic Processes in Physics and Chemistry*. North-Holland, 1981.
- [131] Giovanni Bussi and Michele Parrinello. Accurate sampling using langevin dynamics. *Phys. Rev. E*, 75:056707, 2007.
- [132] James C. Phillips, Rosemary Braun, Wei Wang, James Gumbart, Emad Tajkhorshid, Elizabeth Villa, Christophe Chipot, Robert D. Skeel,

- Laxmikant Kalé, and Klaus Schulten. Scalable molecular dynamics with NAMD. *Journal of Computational Chemistry*, 26(16):1781–1802, 2005.
- [133] S. Nose. A unified formulation of the constant temperature molecular dynamics methods. *J. Chem. Phys.*, 81:511, 1984.
- [134] W. G. Hoover. Canonical dynamics: Equilibrium phase-space distributions. *Phys. Rev. A*, 31:1695, 1985.
- [135] Plimpton S. Fast parallel algorithms for Short-Range molecular dynamics. *Journal of Computational Physics*, 117:1–19, March 1995.
- [136] Julian D. Gale and Andrew L. Rohl. The general utility lattice program. *Molecular Simulation*, 29:291–341, May 2003.
- [137] William Thomson. LX. on the equilibrium of vapour at a curved surface of liquid. *Philosophical Magazine Series 4*, 42(282):448, 1871.
- [138] P Pawlow. Über die Abhängigkeit des Schmelzpunktes von der Oberflächenenergie eines festen Körpers (Zusatz.). *Z. Phys. Chem.*, 65:545–548, 1909.
- [139] Mieko Takagi. Electron-Diffraction study of Liquid-Solid transition of thin metal films. *J. Phys. Soc. Jpn.*, 9:359–363, 1954.
- [140] K Hanszen. Theoretische Untersuchungen über den Schmelzpunkt kleiner Kugelchen - Ein Beitrag zur Thermodynamik der Grenzflächen. *Z. Phys. Chem.*, 157:523–553, 1960.
- [141] Yue Qi, Tahir Cagin, William L. Johnson, and William A. Goddard III. Melting and crystallization in ni nanoclusters: The mesoscale regime. *J. Chem. Phys.*, 115(1):385–394, July 2001.
- [142] Ph. Buffat and J-P. Borel. Size effect on the melting temperature of gold particles. *Phys. Rev. A*, 13(6):2287–2298, Jun 1976.

- [143] T. Castro, R. Reifengerger, E. Choi, and R. P. Andres. Size-dependent melting temperature of individual nanometer-sized metallic clusters. *Phys. Rev. B*, 42(13):8548–8556, Nov 1990.
- [144] S. L. Lai, J. Y. Guo, V. Petrova, G. Ramanath, and L. H. Allen. Size-dependent melting properties of small tin particles: Nanocalorimetric measurements. *Phys. Rev. Lett.*, 77(1):99, Jul 1996.
- [145] C. E. Bottani, A. Li Bassi, B. K. Tanner, A. Stella, P. Tognini, P. Cheyssac, and R. Kofman. Melting in metallic sn nanoparticles studied by surface brillouin scattering and synchrotron-x-ray diffraction. *Phys. Rev. B*, 59(24):R15601–R15604, Jun 1999.
- [146] Martin Schmidt, Robert Kusche, Werner Kronmüller, Bernd von Issendorff, and Hellmut Haberland. Experimental determination of the melting point and heat capacity for a free cluster of 139 sodium atoms. *Phys. Rev. Lett.*, 79(1):99, Jul 1997.
- [147] Martin Schmidt, Robert Kusche, Bernd von Issendorff, and Hellmut Haberland. Irregular variations in the melting point of size-selected atomic clusters. *Nature*, 393(6682):238–240, May 1998.
- [148] R. Kusche, Th. Hippler, M. Schmidt, B. von Issendorff, and H. Haberland. Melting of free sodium clusters. *Eur. Phys. J. D*, 9(1):1–4, December 1999.
- [149] Christian Hock, Christof Bartels, Samuel Straburg, Martin Schmidt, Hellmut Haberland, Bernd von Issendorff, and Andrs Aguado. Premelting and postmelting in clusters. *Phys. Rev. Lett.*, 102(4):043401, 2009.
- [150] Thomas Bachelts, Hans-Joachim Gntherodt, and Rolf Schfer. Melting of isolated tin nanoparticles. *Phys. Rev. Lett.*, 85(6):1250, 2000.
- [151] Gary A. Breaux, Colleen M. Neal, Baopeng Cao, and Martin F. Jarrold. Melting, premelting, and structural transitions in Size-Selected alu-

- minum clusters with around 55 atoms. *Phys. Rev. Lett.*, 94(17):173401, 2005.
- [152] Colleen M. Neal, Anne K. Starace, and Martin F. Jarrold. Melting transitions in aluminum clusters: The role of partially melted intermediates. *Phys. Rev. B*, 76(5):054113, 2007.
- [153] Anne K. Starace, Baopeng Cao, Oscar H. Judd, Indrani Bhattacharyya, and Martin F. Jarrold. Melting of size-selected aluminum nanoclusters with 84–128 atoms. *J. Chem. Phys.*, 132(3):034302–9, 2010.
- [154] Gary A. Breaux, Damon A. Hillman, Colleen M. Neal, Robert C. Benirschke, and Martin F. Jarrold. Gallium cluster Magic melters. *J. Am. Chem. Soc.*, 126(28):8628–8629, 2004.
- [155] Pierre Papon, Jacques Leblond, and Paul Herman Ernst Meijer. *The physics of phase transitions*. Springer, July 2006.
- [156] S. Pochon, K. F. MacDonald, R. J. Knize, and N. I. Zheludev. Phase coexistence in gallium nanoparticles controlled by electron excitation. *Phys. Rev. Lett.*, 92(14):145702, 2004.
- [157] Y. Yamaguchi and S. Maruyama. A molecular dynamics simulation of the fullerene formation process. *Chem. Phys. Lett.*, 286:336–342, 1998.
- [158] H. Lange. Spectral diagnostics of helium-carbon arc plasma during carbon nanostructure formation. *Fullerenes, Nanotubes and Carbon Nanostruct.*, 5:1177–1201, 1997.
- [159] Przemyslaw Byszewski, Hubert Lange, Andrzej Huczko, and Jrgen F. Behnke. Fullerene and nanotube synthesis. plasma spectroscopy studies. *J. Phys. Chem. Solids*, 58(11):1679–1683, 1997.
- [160] H. Lange, K. Saidane, M. Razafinimanana, and A. Gleizes. Temperatures and  $c_2$  column densities in a carbon arc plasma. *J. Phys. D: Appl. Phys.*, 32(9):1024–1030, 1999.

- [161] A. Huczko, H. Lange, P. Byszewski, M. Poplawska, and A. Starski. Fullerene formation in carbon arc: Electrode gap dependence and plasma spectroscopy. *J. Phys. Chem.*, 101:1267, 1997.
- [162] S. Akita, H. Ashihara, and Y. Nakayama. Optical emission spectroscopy of arc flame plasma for generation of carbon nanotubes. *Jpn. J. Appl. Phys.*, 39:4939–4944, 2000.
- [163] Takumi Kimura, Toshiki Sugai, Hisanori Shinohara, Takashi Goto, Kazuyuki Tohji, and Isao Matsuoka. Preferential arc-discharge production of higher fullerenes. *Chem. Phys. Lett.*, 246(6):571–576, 1995.
- [164] J. B. Howard, J. T. McKinnon, Y. Makarovskiy, A. L. Lafleur, and M. E. Johnson. Fullerenes  $c_{60}$  and  $c_{70}$  in flames. *Nature*, 352:139–141, 1991.
- [165] Xiaolong Song, Yongning Liu, and Jiewu Zhu. The effect of furnace temperature on fullerene yield by a temperature controlled arc discharge. *Carbon*, 44(8):1584–1586, 2006.
- [166] T. Ishigaki, S. Suzuki, H. Kataura, W. Krtzschmer, and Y. Achiba. Characterization of fullerenes and carbon nanoparticles generated with a laser-furnace technique. *Applied Physics A: Materials Science & Processing*, 70(2):121–124, 2000.
- [167] Roger Taylor. On the formation and stability of fullerenes. *Fullerenes, Nanotubes, Carbon Nanostruct.*, 7(2):305, 1999.
- [168] B. L. Zhang, C. H. Xu, C. Z. Wang, C. T. Chan, and K. M. Ho. Systematic study of structures and stabilities of fullerenes. *Phys. Rev. B*, 46(11):7333, 1992.
- [169] Noriyuki Kurita, Kinya Kobayashi, Hiroki Kumahora, Kazutami Tago, and Kunio Ozawa. Dependence of binding energy on the number of atoms for carbon fullerenes. *J. Phys. Soc. Jpn.*, 62(7):2279–2284, 1993.



- [170] R. J. Cross and M. Saunders. Transmutation of fullerenes. *J. Am. Chem. Soc.*, 127(9):3044–3047, 2005.
- [171] Rainer D. Beck, Jorg Rockenberger, Patrick Weis, and Manfred M. Kappes. Fragmentation of  $C_{60}^+$  and higher fullerenes by surface impact. *J. Chem. Phys.*, 104(10):3638–3650, 1996.
- [172] Takumi Kimura, Toshiki Sugai, and Hisanori Shinohara. Surface-induced fragmentation of higher fullerenes and endohedral metallofullerenes. *J. Chem. Phys.*, 110(19):9681–9687, 1999.
- [173] Wenzhen Li, Changhai Liang, Jieshan Qiu, Weijiang Zhou, Hongmei Han, Zhaobin Wei, Gongquan Sun, and Qin Xin. Carbon nanotubes as support for cathode catalyst of a direct methanol fuel cell. *Carbon*, 40(5):791–794, 2002.
- [174] Kuanping Gong, Feng Du, Zhenhai Xia, Michael Durstock, and Liming Dai. Nitrogen-Doped carbon nanotube arrays with high electrocatalytic activity for oxygen reduction. *Science*, 323(5915):760–764, 2009.
- [175] Jason K. Holt, Hyung Gyu Park, Yinmin Wang, Michael Stadermann, Alexander B. Artyukhin, Costas P. Grigoropoulos, Aleksandr Noy, and Olgica Bakajin. Fast mass transport through Sub-2-Nanometer carbon nanotubes. *Science*, 312(5776):1034–1037, 2006.
- [176] A. Srivastava, O. N. Srivastava, S. Talapatra, R. Vajtai, and P. M. Ajayan. Carbon nanotube filters. *Nat Mater*, 3(9):610–614, 2004.
- [177] Albert G. Nasibulin, Sergey D. Shandakov, Larisa I. Nasibulina, Andrzej Cwirzen, Prasantha R. Mudimela, Karin Habermehl-Cwirzen, Dmitrii A. Grishin, Yuriy V. Gavrilov, Jari E. M. Malm, Unto Tapper, Ying Tian, Vesa Penttala, Maarit J. Karppinen, and Esko I. Kauppinen. A novel cement-based hybrid material. *New. J. Phys.*, 11(2):023013, 2009.
- [178] Zhi Wang, Zhiyong Liang, Ben Wang, Chuck Zhang, and Leslie Kramer. Processing and property investigation of single-walled carbon

- nanotube (SWNT) buckypaper/epoxy resin matrix nanocomposites. *Composites Part A: Applied Science and Manufacturing*, 35(10):1225–1232, 2004.
- [179] R. Z. Ma, J. Liang, B. Q. Wei, B. Zhang, C. L. Xu, and D. H. Wu. Study of electrochemical capacitors utilizing carbon nanotube electrodes. *J. Power Sources*, 84(1):126–129, 1999.
- [180] E. Frackowiak, K. Metenier, V. Bertagna, and F. Beguin. Supercapacitor electrodes from multiwalled carbon nanotubes. *Appl. Phys. Lett.*, 77(15):2421–2423, 2000.
- [181] Elzbieta Frackowiak and Francois Bguin. Carbon materials for the electrochemical storage of energy in capacitors. *Carbon*, 39(6):937–950, 2001.
- [182] Ding Wang, Pengcheng Song, Changhong Liu, Wei Wu, and Shoushan Fan. Highly oriented carbon nanotube papers made of aligned carbon nanotubes. *Nanotechnology*, 19(7):075609, 2008.
- [183] Zhongfu Zhao and Jan Gou. Improved fire retardancy of thermoset composites modified with carbon nanofibers. *Science and Technology of Advanced Materials*, 10(1):015005, 2009.
- [184] D. Ugarte. Onion-like graphitic particles. *Carbon*, 33(7):989–993, 1995.
- [185] M. S. Zwanger, F. Banhart, and A. Seeger. Formation and decay of spherical concentric-shell carbon clusters. *J. Cryst. Growth*, 163(4):445–454, 1996.
- [186] Satoshi Tomita, Takahiro Sakurai, Hitoshi Ohta, Minoru Fujii, and Shinji Hayashi. Structure and electronic properties of carbon onions. *J. Chem. Phys.*, 114(17):7477–7482, 2001.
- [187] Mauricio Terrones, Guillermo Terrones, and Humberto Terrones. Structure, chirality, and formation of giant icosahedral fullerenes and spherical graphitic onions. *Structural Chemistry*, 13(3):373–384, 2002.

- [188] F. Banhart and P. M. Ajayan. Carbon onions as nanoscopic pressure cells for diamond formation. *Nature*, 382(6590):433–435, 1996.
- [189] P. Wesolowski, Y. Lyutovich, F. Banhart, H. D. Carstanjen, and H. Kronmuller. Formation of diamond in carbon onions under MeV ion irradiation. *Appl. Phys. Lett.*, 71(14):1948–1950, 1997.
- [190] Y. Lyutovich and F. Banhart. Low-pressure transformation of graphite to diamond under irradiation. *Appl. Phys. Lett.*, 74(5):659–660, 1999.
- [191] Satoshi Tomita, Minoru Fujii, Shinji Hayashi, and Keiichi Yamamoto. Transformation of carbon onions to diamond by low-temperature heat treatment in air. *Diamond and Related Materials*, 9(3-6):856–860, 2000.
- [192] R. Astala, M. Kaukonen, R. M. Nieminen, G. Jungnickel, and Th. Frauenheim. Simulations of diamond nucleation in carbon fullerene cores. *Phys. Rev. B*, 63(8):081402, 2001.
- [193] A. S. Barnard, S. P. Russo, and I. K. Snook. Coexistence of bucky diamond with nanodiamond and fullerene carbon phases. *Phys. Rev. B*, 68(7):073406, 2003.
- [194] A. S. Barnard, S. P. Russo, and I. K. Snook. Size dependent phase stability of carbon nanoparticles: Nanodiamond versus fullerenes. *J. Chem. Phys.*, 118(11):5094–5097, 2003.
- [195] J.-M. Leyssale and G.L. Vignoles. Molecular dynamics evidences of the full graphitization of a nanodiamond annealed at 1500 k. *Chem. Phys. Lett.*, 454(4-6):299–304, 2008.
- [196] Oleksandr O. Mykhaylyk, Yurii M. Solonin, David N. Batchelder, and Rik Brydson. Transformation of nanodiamond into carbon onions: A comparative study by high-resolution transmission electron microscopy, electron energy-loss spectroscopy, x-ray diffraction, small-angle x-ray scattering, and ultraviolet raman spectroscopy. *J. Appl. Phys.*, 97(7):074302–16, 2005.

- [197] K. S. Novoselov, A. K. Geim, S. V. Morozov, D. Jiang, M. I. Katsnelson, I. V. Grigorieva, S. V. Dubonos, and A. A. Firsov. Two-dimensional gas of massless dirac fermions in graphene. *Nature*, 438(7065):197–200, 2005.
- [198] Claire Berger, Zhimin Song, Xuebin Li, Xiaosong Wu, Nate Brown, Cecile Naud, Didier Mayou, Tianbo Li, Joanna Hass, Alexei N. Marchenkov, Edward H. Conrad, Phillip N. First, and Walt A. de Heer. Electronic confinement and coherence in patterned epitaxial graphene. *Science*, 312(5777):1191–1196, 2006.
- [199] Alexander Tzalenchuk, Samuel Lara-Avila, Alexei Kalaboukhov, Sara Paolillo, Mikael Syvajarvi, Rositza Yakimova, Olga Kazakova, Janssen T. J. B. M., Vladimir Fal’ko, and Sergey Kubatkin. Towards a quantum resistance standard based on epitaxial graphene. *Nat Nano*, advance online publication, 2010.
- [200] Tim J. Booth, Peter Blake, Rahul R. Nair, Da Jiang, Ernie W. Hill, Ursel Bangert, Andrew Bleloch, Mhairi Gass, Kostya S. Novoselov, M. I. Katsnelson, and A. K. Geim. Macroscopic graphene membranes and their extraordinary stiffness. *Nano. Lett.*, 8(8):2442–2446, 2008.
- [201] Goki Eda, Giovanni Fanchini, and Manish Chhowalla. Large-area ultrathin films of reduced graphene oxide as a transparent and flexible electronic material. *Nat Nano*, 3(5):270–274, 2008.
- [202] Sungjin Park and Rodney S. Ruoff. Chemical methods for the production of graphenes. *Nat Nano*, 4(4):217–224, 2009.
- [203] Johann Coraux, Alpha T. N’Diaye, Carsten Busse, and Thomas Michely. Structural coherency of graphene on ir(111). *Nano. Lett.*, 8(2):565–570, 2008.
- [204] Alexander N. Obraztsov. Chemical vapour deposition: Making graphene on a large scale. *Nat Nano*, 4(4):212–213, 2009.

- [205] Alfonso Reina, Xiaoting Jia, John Ho, Daniel Nezich, Hyungbin Son, Vladimir Bulovic, Mildred S. Dresselhaus, and Jing Kong. Large area, Few-Layer graphene films on arbitrary substrates by chemical vapor deposition. *Nano. Lett.*, 9(1):30–35, 2009.
- [206] Prakash R. Somani, Savita P. Somani, and Masayoshi Umeno. Planer nano-graphenes from camphor by CVD. *Chem. Phys. Lett.*, 430(1-3):56–59, 2006.
- [207] Peter Blake, Paul D. Brimicombe, Rahul R. Nair, Tim J. Booth, Da Jiang, Fred Schedin, Leonid A. Ponomarenko, Sergey V. Morozov, Helen F. Gleeson, Ernie W. Hill, Andre K. Geim, and Kostya S. Novoselov. Graphene-Based liquid crystal device. *Nano. Lett.*, 8(6):1704–1708, 2008.
- [208] Xuan Wang, Linjie Zhi, and Klaus Mullen. Transparent, conductive graphene electrodes for Dye-Sensitized solar cells. *Nano. Lett.*, 8(1):323–327, 2008.
- [209] Julio A. Alonso. *Structure And Properties of Atomic Nanoclusters*. Imperial College Press, illustrated edition edition, February 2006.
- [210] Zhi Zhang, Wangyu Hu, and Shifang Xiao. Shell and subshell periodic structures of icosahedral nickel nanoclusters. *J. Chem. Phys.*, 122(21):214501, 2005.
- [211] M. Pellarin, B. Baguenard, J.L. Vialle, J. Lerm, M. Broyer, J. Miller, and A. Perez. Evidence for icosahedral atomic shell structure in nickel and cobalt clusters. comparison with iron clusters. *Chemical Physics Lett.*, 217(4):349–356, 1994.
- [212] J. M. Montejano-Carrizales, M. P. Iñiguez, J. A. Alonso, and M. J. López. Theoretical study of icosahedral ni clusters within the embedded-atom method. *Phys. Rev. B*, 54(8):5961, 1996.

- [213] Ilya A. Solov'yov, Andrey V. Solov'yov, Walter Greiner, Andrey Koshelev, and Andrey Shutovich. Cluster growing process and a sequence of magic numbers. *Phys. Rev. Lett.*, 90(5):053401, Feb 2003.
- [214] W. Greiner I. A. Solov'yov, A. V. Solov'yov. Fusion process of lennard-jones clusters: Global minima and magic numbers formation. *Int. J. Mod. Phys. E*, 13:697, 2004.
- [215] O.I. Obolensky, I.A. Solov'yov, A.V. Solov'yov, and W. Greiner. Fusion and fission of atomic clusters: recent advances. *Computing Lett.*, 1:313–318, December 2005.
- [216] R. Vanselow and R. Howe. *Chemistry and Physics Of Solid Surfaces VII*. Springer-Verlag, December 1988.
- [217] J. Jellinek, T. L. Beck, and R. S. Berry. Solid-liquid phase changes in simulated isoenergetic  $\text{Ar}_{13}$ . *J. Chem. Phys.*, 84:2783–2794, March 1986.
- [218] Heidi L. Davis, Julius Jellinek, and R. Stephen Berry. Melting and freezing in isothermal  $\text{Ar}_{13}$  clusters. *J. Chem. Phys.*, 86(11):6456, 1987.
- [219] L.D. Landau, E.M. Lifshitz, J.B. Sykes, and W.H. Reid. *Fluid Mechanics: Volume 6*. A Butterworth-Heinemann Title, 2 edition, August 1987.
- [220] Andres Aguado, Luis E. Gonzalez, and Jose M. López. Thermal properties of Impurity-Doped clusters: Orbital-Free molecular dynamics simulations of the meltinglike transition in  $\text{Li}_{13}\text{Na}_{54}$  and  $\text{Cs}_{13}\text{Na}_{54}$ . *J. Phys. Chem. B*, 108(31):11722–11731, 2004.
- [221] B. M. Ocko, A. Braslau, P. S. Pershan, J. Als-Nielsen, and M. Deutsch. Quantized layer growth at liquid-crystal surfaces. *Phys. Rev. Lett.*, 57(1):94–97, Jul 1986.
- [222] E. Chacón, M. Reinaldo-Falagán, E. Velasco, and P. Tarazona. Layering at free liquid surfaces. *Phys. Rev. Lett.*, 87(16):166101, Sep 2001.

- [223] Oleg A. Louchev, Thomas Laude, Yoichiro Sato, and Hisao Kanda. Diffusion-controlled kinetics of carbon nanotube forest growth by chemical vapor deposition. *J. Chem. Phys.*, 118(16):7622–7634, April 2003.





# LIST OF FIGURES

1	Rekonstituierung der C <sub>60</sub> Struktur bei der kritischen Temperatur im topologisch selektiven Modell. . . . .	ix
2	Der Übergang von C <sub>60</sub> @C <sub>180</sub> zu C <sub>240</sub> beginnt mit der Aufnahme von Kohlenstoff Atomen des C <sub>60</sub> in die C <sub>180</sub> Struktur (a), gefolgt von der Fragmentierung der C <sub>60</sub> Struktur wenn dessen Atome sukzessive in die C <sub>180</sub> Struktur Einwachsen (b) bevor der Endzustand, die C <sub>240</sub> Struktur (c) erreicht wird. . .	x
3.1	Finite-sized heat capacity curves of aluminium clusters consisting of 84-128 atoms [153]. . . . .	35
4.1	The caloric curves (top) and heat capacities (bottom) of C <sub>60</sub> , as calculated using the Tersoff potential for three different simulation times (50 ns, 500 ns and 1000 ns). The figures demonstrate how the phase transition temperature is affected by the total simulation time. Note that the simulation volume is $1.25 \times 10^8 \text{Å}^3$ . . . . .	41
4.2	Caloric curves (top) and heat capacities (bottom) of C <sub>60</sub> , as calculated using the Tersoff potential for volumes $8 \times 10^3 \text{Å}^3$ (dashed red) and $1.25 \times 10^8 \text{Å}^3$ (solid black). <i>Insets</i> : (a) and (b) are, respectively, magnifications of the caloric curve and heat capacity of C <sub>60</sub> in a simulation volume of $8 \times 10^3 \text{Å}^3$ ; (b) shows that the heat capacity has double extrema whose derivative, shown in (c), has a significant peak indicating a second-order-like phase transition. Note that the simulation time is 500 ns. . . . .	45

- 4.3 Total energy as a function of simulation time at the phase transition temperature of  $C_{60}$  as calculated with the Tersoff potential. The *inset* shows the behaviour of the total energy for the complete 1000 ns long simulation, while the main plot shows magnification of the inset between 0-500 ns, highlighting the steps in the total energy before fullerene fragmentation (see text for a discussion regarding the energy steps). Note that the simulation volume is  $1.25 \times 10^8 \text{ \AA}^3$ . . . . . 46
- 4.4 Snapshots of the  $C_{60}$  fragmentation process at the phase transition temperature (as calculated using the Tersoff potential). The snapshots (a)–(e) occur between 0-500 ns, prior to the total energy jump shown in Fig. 4.3. Note that the simulation volume is  $1.25 \times 10^8 \text{ \AA}^3$ . . . . . 48
- 4.5 The energy profiles (left) and evolved structures (right) of  $C_{60}$ , as calculated using the Tersoff potential, for temperatures of (a) 3000 K, (b) 3750 K and (c) 5000 K. Note that the simulation volume is  $8 \times 10^3 \text{ \AA}^3$ . . . . . 50
- 4.6 (colour online) Averaged number of fragments for selected excitation energies (100, 120, 130, 200 and 300 eV). In *red*: results obtained using TCF show a heavier weighting for  $C_2$  and  $C_{60}$  fragments . In *blue*: results of Ref. [61] using a tight-binding approach. . . . . 53
- 4.7 Caloric curves (top) and heat capacities (bottom) of  $C_{60}$ , as calculated using the Topologically-constrained forcefield for volumes  $8 \times 10^3 \text{ \AA}^3$  (dashed red) and  $1.25 \times 10^8 \text{ \AA}^3$  (solid black). Note that the simulation time is 500 ns. . . . . 55
- 4.8 Total energy as a function of simulation time at a temperature of 5125 K—the phase transition temperature in  $C_{60}$  as calculated with the Topologically-constrained forcefield. Note that the simulation volume is  $1.25 \times 10^8 \text{ \AA}^3$  and the total simulation time is 500 ns. . . . . 56

- 4.9 Snapshots of the  $C_{60}$  fragmentation process at the phase transition temperature (as calculated using the Topologically-constrained forcedfield). The snapshots (a)–(e) occur between 0-200 ns, prior to the total energy jump shown in Fig. 4.8. . . . . . 58
- 4.10 Consecutive oscillations in the time-dependent total energy of  $C_{60}$ , as calculated using the Topologically-constrained forcefield. The oscillations indicate that  $C_{60}$  shows a coexistence between the cage and gaseous phases—dynamically, this translates to consecutive fragmentation and reassembly of the carbon cage at the phase transition temperature of 5855 K. Note that the simulation volume is  $8 \times 10^3 \text{Å}^3$  and the total simulation time is 500 ns. . . . . . 59
- 4.11 Reassembly of the  $C_{60}$  cage at the phase transition temperature using the Topologically-constrained forcefield. The times indicated above each panel refers to the relative time between panels. The simulation was conducted in a volume of  $8 \times 10^3 \text{Å}^3$ . 60
- 4.12 Molefraction of the carbon vapour consisting of the C,  $C_2$  and  $C_3$  species. The distribution is based on the equilibrium concentration of the carbon vapour in an arc-discharge experiment, as given in Ref. [159]. *Inset*: the  $C_2$  molefraction fitted using equation 4.11 with parameters given in Table 4.3. . . . . 67

4.13	Dependence of the phase transition temperature on pressure. <i>Thick black line:</i> results of the model when the C <sub>2</sub> partial pressure is equivalent to the chamber pressure. The model is estimated to be valid in the pressure range marked by the thick black line. <i>Dashed red line:</i> results of the model when the C <sub>2</sub> partial pressure is given by the distribution in Ref. [159], see text for further details. <i>Inset:</i> all cited arc-discharge experimental works were conducted using a 6 mm electrode diameter. The current and chamber pressure are given in the brackets for each respective work. ★ [160] for (100 A, 13.3 kPa), ▲ [161] for (86 A and 131 A, 13.3 kPa), ▼ [158] for (88 A and 120 A, 17 kPa), ■ [28] for (100 A, 7 kPa) and (85 A, 13 kPa) and ● [159] for (75 A, 17 kPa). . . . .	70
5.1	Typical time-of-flight mass spectra indicating the high abundance of C <sub>60</sub> . This particular spectra was produced by resistive heating of graphite rods [27] . . . . .	74
5.2	Time-of-flight mass spectra of carbon extracted soot prepared by the arc-discharge of (a) a pure graphite rod and (b) 1% boron-doped graphite rod [163]. . . . .	75
5.3	Time-of-flight mass spectra of the raw soot produced in an arc furnace [165] at: (a) room temperature, (b) 200°C and (c) 500°C. . . . .	76
5.4	Fullerenes investigated in this subsection. . . . .	77
5.5	Caloric curves (top) and heat capacities (bottom) of fullerenes C <sub>32</sub> to C <sub>540</sub> . The phase transition temperatures indicated by the maximum of the heat capacity peaks are C <sub>32</sub> : 3320 K, C <sub>60</sub> : 3658 K, C <sub>70</sub> : 3715 K, C <sub>80</sub> : 3820 K, C <sub>90</sub> : 3945 K, C <sub>180</sub> : 4103 K, C <sub>240</sub> : 4388 K and C <sub>540</sub> : 4825 K. . . . .	79

- 5.6 *Solid lines* indicate the binding energy as calculated using the Tersoff potential (black squares), tight-binding method (red triangles) and Harris-SCF-GGA (blue circles). *Dashed lines* show the binding energy of each fullerene with respect to the binding energy of graphite ( $E_{\text{graphite}}-E_{\text{fullerene}}$ ), as calculated within each method. . . . . 80
- 5.7 Transformation to graphene prior to multifragmentation for (a)  $C_{32}$  and (b)  $C_{70}$ . . . . . 83
- 5.8 Fullerenes larger than  $C_{70}$  do not show transformation to graphene, but show rapid multifragmentation, as shown for (a)  $C_{90}$ , (b)  $C_{240}$  and (c)  $C_{540}$ . . . . . 84
- 5.9 Time-dependent total energy per atom of  $C_{32}$ ,  $C_{70}$  and  $C_{240}$ . Steps in the energy profiles of  $C_{32}$  and  $C_{70}$  can be seen, similar to those found for  $C_{60}$  in Chapter 4. . . . . 86
- 5.10 The  $C_{240}$  nanocarbon phases considered in this work: (a)  $C_{240}$  fullerene, (b)  $C_{60}@C_{180}$  carbon onion, (c) uncapped  $C_{240}^n$  nanotube with chirality of (10,10), (d)  $C_{240}^g$  graphene sheet and (e)  $C_{240}^b$  buckyowl. . . . . 89
- 5.11 Caloric curves (left) and respective heat capacities (right) for the  $C_{240}$  structures considered in this work. . . . . 90
- 5.12 Transformation of the  $C_{60}@C_{180}$  to a  $C_{240}$  fullerene before fragmentation . . . . . 91
- 5.13 The transformation of  $C_{60}@C_{180}$  to  $C_{240}$  begins with (a) incorporation of C atoms from  $C_{60}$  into the  $C_{180}$  shell, followed by (b) the fragmentation of the  $C_{60}$  cage as its atoms fuel the growth of  $C_{180}$  to form the final  $C_{240}$  structure in (c). . . . . 92
- 6.1 The four nickel structure that are investigated, (a) the optimised structure of a pure  $Ni_{147}$  cluster; (b) the *ground* state structure of the C-doped  $Ni_{147}$  cluster; (c) the *isomer* state structure of the C-doped  $Ni_{147}$  cluster; (d) the optimised structure of the  $C_2$ -doped  $Ni_{147}$  cluster. . . . . 96

- 6.2 Caloric curve (left) and heat capacity (right) of the pure Ni<sub>147</sub> cluster. Temperatures  $T < T_{freeze}$  and  $T > T_{melt}$  correspond respectively to the completely frozen and molten states. The melting temperature of the cluster,  $T_m = 750$  K, is given by the maximum of the heat capacity. . . . . 98
- 6.3 Time dependence of the instantaneous values of the total energy calculated for the Ni<sub>147</sub> cluster: (a)  $T = 600$  K, frozen state; (b)  $T = 750$  K, phase transition; (c)  $T = 800$  K, molten state. The dashed-dotted lines demonstrate the time-averaged total energy of the system. . . . . 100
- 6.4 Caloric curves (left) and heat capacities (right) of the pure Ni<sub>147</sub> cluster (solid line), the C-doped Ni<sub>147</sub> cluster (dashed-dotted line) and the C<sub>2</sub>-doped Ni<sub>147</sub> cluster (dotted line). The melting temperature are  $T_m = 750$  K, 720 K and 725 K for the Ni<sub>147</sub>, C-doped Ni<sub>147</sub> and C<sub>2</sub>-doped Ni<sub>147</sub> clusters respectively. 101
- 6.5 The two-dimensional projection of trajectories calculated for the Ni atom in the center of the C-doped Ni<sub>147</sub> cluster (filled dots), the Ni atom from the vertex of the cluster surface (stars) and the C impurity (open dots) for the cluster temperatures  $T = 400$  K, 680 K, and 800 K. The output time step is 1 ps and the total simulation time is 2 ns. . . . . 104
- 6.6 The time-averaged radial distribution function  $g(r)$  calculated for the Ni and C atoms in the C-doped Ni<sub>147</sub> cluster at different temperatures. . . . . 105
- 6.7 Temperature dependence of diffusion coefficients calculated for the Ni atom in the center of the C-doped Ni<sub>147</sub> cluster (filled dots), the Ni atom on the cluster surface (stars) and the C impurity (open dots). . . . . 107

- 6.8 Morse potential for the Ni – C interaction with different values of parameters  $\rho$  and  $r_0$ . *Curve 1*,  $\rho = 3.295$ ,  $r_0 = 1.763$  Å (optimal values); *Curve 2*,  $\rho = 1.648$ ,  $r_0 = 0.882$  Å (reduced bonding); *Curve 3*,  $\rho = 4.943$ ,  $r_0 = 2.645$  Å (enlarged bonding). The depth of the potential well is kept constant  $\varepsilon_M = 2.431$  eV. . . . . 109
- 6.9 The number of Ni atoms  $\Delta N$  at distances between  $r$  and  $r + \Delta r$  from the center of mass of the C-doped Ni<sub>147</sub> cluster calculated for different values of the parameters  $\rho$  and  $r_0$ : (a)  $\rho = 1.648$ ,  $r_0 = 0.882$  Å (reduced bonding); (b)  $\rho = 3.295$ ,  $r_0 = 1.763$  Å (optimal values); (c)  $\rho = 4.943$ ,  $r_0 = 2.645$  Å (enlarged bonding); (d) pure Ni<sub>147</sub> cluster for comparison. The radial interval  $\Delta r$  is 0.001 Å. . . . . 110
- 6.10 (Left) caloric curves for the C-doped Ni<sub>147</sub> cluster calculated for the different values of parameters  $\rho$  and  $r_0$ . *Curve 1*,  $\rho = 3.295$ ,  $r_0 = 1.763$  Å (optimal values); *Curve 2*,  $\rho = 1.648$ ,  $r_0 = 0.882$  Å (reduced bonding); *Curve 3*,  $\rho = 4.943$ ,  $r_0 = 2.645$  Å (enlarged bonding). The depth of the potential well is kept constant  $\varepsilon_M = 2.431$  eV. (Right) heat capacity for the C-doped Ni<sub>147</sub> cluster calculated for the different values of parameters  $\rho$  and  $r_0$ . *Curve 1*,  $\rho = 3.295$ ,  $r_0 = 1.763$  Å (optimal values); *Curve 2*,  $\rho = 1.648$ ,  $r_0 = 0.882$  Å (reduced bonding); *Curve 3*,  $\rho = 4.943$ ,  $r_0 = 2.645$  Å (enlarged bonding). The depth of the potential well is kept constant  $\varepsilon_M = 2.431$  eV. Arrow indicates the melting temperature of the pure Ni<sub>147</sub> cluster. . . 111





# LIST OF TABLES

2.1	Tersoff potential parameters for carbon . . . . .	22
2.2	The fullerene forcefield parameters . . . . .	26
4.1	Comparison of the energies of the structures calculated with the topologically-constrained forcefield (TCF) and the Tersoff potential. TCF has two C-C energy parameters which we refer to as the single (s) bond and the double (d) bond. In the table below, we present the energies of the structures of the most stable linear ( $C_2$ to $C_5$ ) and planar ( $C_6$ ) isomers of small carbon clusters. The energies calculated within TCF are constrained by the fact that each carbon atom can have only one double bond. . . . .	51
4.2	Fitting parameters for the $C_2$ molefraction . . . . .	66
5.1	Energetics of fullerene and graphene structures . . . . .	85



# CURRICULUM VITAE

## ADILAH HUSSIEN

Address           Wurmbachstr. 10, Frankfurt am Main, 60487 Germany.  
E-mail           hussein@fias.uni-frankfurt.de  
Nationality      Singaporean.  
Date of birth    April 16, 1984.

## EDUCATION

2006-2010   PHD in Physics, Frankfurt Institute for Advanced Studies, Germany.  
2002-2006   MSci in Physics, Imperial College London, United Kingdom.  
2001-2002   GCE A-LEVELS, Cambridge Tutors College, United Kingdom.

## PUBLICATIONS & TALKS

### JOURNAL ARTICLES

- 2010   A. Hussien, A. V. Yakubovich, A. V. Solov'yov and W. Greiner,  
“Phase Transition, formation and fragmentation of fullerenes”,  
*Eur. Phys. J. D* (2010).
- 2009   A. Hussien, A. V. Yakubovich and A. V. Solov'yov,  
“Studying Phase Transition in Nanocarbon Structures”,  
*AIP Conf. Proc. (ISACC 2009)* **1197**, 152 (2009).
- 2009   A. G. Lyalin, A. Hussien, A. V. Solov'yov and W. Greiner,  
“Impurity effects on the melting of nickel clusters as seen via molecular  
dynamics simulations”, *Phys. Rev. B* **79**, 165403 (2009).

## POSTERS

- 2009 A. Hussien, A. V. Yakubovich, A. V. Solov'yov and W. Greiner, "Fullerene phase transitions", *ISACC 2009*, Michigan, USA.
- 2008 A. Hussien, A. V. Yakubovich, A. V. Solov'yov and W. Greiner, "Phase Transitions in Fullerenes: fragmentation & reassembly of the carbon cage", *ISACC 2008*, St. Petersburg, Russia.
- 2007 A. Hussien, A. V. Yakubovich, A. V. Solov'yov and W. Greiner, "Phase Transitions in Fullerenes", *International Workshop on Atomic Physics*, Max Planck Institute for Complex Systems, Dresden, Germany.
- 2007 A. Hussien, A. V. Yakubovich, A. V. Solov'yov and W. Greiner, "Phase Transitions in Fullerenes", *ISACC 2007*, Darmstadt, Germany.
- 2007 A. Hussien, A. V. Yakubovich, A. V. Solov'yov and W. Greiner, "Phase Transitions in Fullerenes", *Symposium on Size Selected Clusters (S<sup>3</sup>C 2007)*, Brand, Austria.

## TALKS

- 2009 A. Hussien, A. Lyalin, A. V. Solov'yov and W. Greiner, "Melting on carbon-doped nickel clusters", *ISACC 2009*, Michigan, USA.
- 2008 A. Hussien, A. V. Yakubovich, A. V. Solov'yov and W. Greiner, "Phase Transitions in Fullerenes: fragmentation & reassembly of the carbon cage", *ISACC 2008*, St. Petersburg, Russia.

## AWARDS

- 2008 European Physical Society, Poster Prize.

## WORK EXPERIENCE

- 2005 Undergraduate research internship, High Energy Physics, Imperial College London, United Kingdom.
- 2005 Teaching assistant, The Hackney Powermaths Project, London, United Kingdom.
- 2004 Private tutoring in physics, London, United Kingdom.
- 2004 Undergraduate research internship, deltaDOT Ltd., London, United Kingdom.
- 2004 Student mentor with Aimhigher, St. Aloysius' College, London, United Kingdom.

## SKILLS

### IT & PROGRAMMING

C++, Perl, PHP, markup languages (XHTML, XML, CSS),  $\LaTeX$ , UNIX shell scripting.

Experienced with: Wordpress, MovableType, Adobe Photoshop, GIMP.

Operating systems: Linux (Ubuntu, Debian) and Windows Vista/XP.

### LANGUAGES

English (fluent), Malay (native), Japanese (intermediate), Arabic (written), German (basic) and French (basic).

